Beam Steerable Antennas Reconfigured Using Liquid Metal

By

Zhishu Qu

A thesis submitted in partial fulfilment of the requirements for the degree of

Doctor of Philosophy

School of Electronic Engineering and Computer Science
Queen Mary University of London

United Kingdom

September 2022

Declaration

I, Zhishu Qu, confirm that the research included within this thesis is my own or that where it has been carried out in collaboration with, or supported by others, that this duly acknowledged below and my contribution indicated. Previously published material is also acknowledged.

I attest that I have exercised reasonable care to ensure that the work is original, and does not to the best of my knowledge break any UK law, infringe any third party copyright or other intellectual property right, or contain any confidential material. I accept that the college has the right to use plagiarism software to check the electronic version of the thesis. I confirm that the thesis has not previously submitted for the award of a degree by this or any other university. The copy right of this thesis rests with the author and no quotation from it or information derived from it may be published without prior written consent of the author.

Signature: Zhishu Qu

Date: 23/09/2022

Dedication

I dedicate this work to all my family members.

I could not have done it without your support.

Abstract

Beam steerable antennas are required for use in a range of emerging applications, including satellite internet, and 5G mobile access at millimeter wave (mmWave) frequencies. Liquid metal, as a new material, attracts an increasing attention due to its advantages of low insertion loss, low harmonic distortion, and large tuning ranges. Unlike conventional beam steerable antennas, there is relatively little work has been done on the topic of antennas reconfigured using liquid metal with beam steering capability. In this thesis, the research focuses on the development of patch antennas as well as arrays, achieving beam steering capability based on liquid metal. The proposed antennas reported in this thesis have low cost, wide scan angle, and low scan loss.

Firstly, a theoretical calculation of the transmission behavior limit for the multi-layer reconfigurable transmit-array unit cell is proposed, which could guide the future similar designs. The theoretical calculations have been validated through computer simulation. This is the first study to be applicable to transmit-array unit cells in which the conducting resonators, on the different layers, are shaped differently. Based on the above theoretical study, we further design a reconfigurable transmit-array unit cell using liquid metal. It has low profile with only three conducting layers. The proposed prototype was fabricated and measured within an open-ended waveguide. It is the first time that a reconfigurable transmit-array unit cell, employing liquid metal, provides a large phase shifting range together with low insertion loss.

Then beam steerable microstrip patch antennas are also presented. The proposed antennas utilize two beam switching techniques in concert, including parasitic steering technique and switchable ground plane. The proposed antennas have low scan loss across the large scan angle range. The proposed antennas were fabricated and measured.

The measured results agree well with the simulated results and validate the effectiveness of the proposed antennas. More importantly, the switchable ground plane as a novel beam switching approach is firstly proposed in this work.

Finally, an improved microstrip patch antenna was reported. The improvement enables continuous beam steering. To this end we designed a liquid metal channel and fabricated it using a 3D printer. With this improved channel, the updated patch antenna can achieve a continuous beam steering. This is the first microstrip patch antenna having the capability of continuous beam steering in the elevation plane.

This thesis proposes novel antenna solutions based on liquid metal with beam steering capability. The designed antennas with essential characteristics, including low cost, wide scan angle, low scan loss, and high efficiency, could be used in future wireless communications.

Acknowledgments

I would like to express my deepest gratitude to my PhD supervisor, Dr James Kelly, for his support, guidance, and patience throughout my doctoral studies. Many of his qualities, such as hard work and passion for research, are worth learning from and have had a profound impact on me. It has been a great pleasure and honour for me to work with him. Dr James is a very responsible supervisor who is always there to help his students. I am thankful to him.

I would also like to thank my co-supervisor, Dr Akram Alomainy, for his support and active interest in the research topics of my thesis. I would like to thank my Stages 1 and 2 examiners, Dr Robert Donnan and Dr Mona Jaber. Thanks for their great technical discussions and comments on my work which made me improve further.

Many thanks to the staff of the Antenna lab., Electronic lab. and Antennas workshop at Queen Mary University of London (QMUL). These include but are not limited to Dr Max Munoz, Dr Abdre Andy, Mr Kok Ho Huen, Mrs Geetha Bommiredy, Mrs Patricia Goddard, and Mr Geoffrey.

I am thankful to all my family members, especially my husband Mr Siyuan Wu. I could not have done it without your support. I am also thankful to all my friends in QMUL who helped me during this time and made my stay here memorable.

Table of Contents

List of Figures

List of Tables

List of Abbreviations

FSS	Frequency Select Surface
PDMS	Polydimethylsiloxane
mmW	Millimeter Wave
SLL	Side Lobe Level
MEMS	Microelectromechanical systems
LC	Liquid Crystal
PCB	Printed Circuit Board
Hg	Mercury
NaK	Eutectic Sodium Potassium
Ga	Gallium
EGaIn	Eutectic Gallium Indium
SLA	Stereolithography
DLP	Digital Light Processing
FDM	Fused Deposition Modeling
SLS	Selective Laser Sintering

LOM	Laminated Object Manufacturing
ABS	Acrylonitrile Butadiene Styrene
PLA	Polylactic Acid
SRR	Split Ring Resonator
3D	Three Dimension
ECC	Electrochemically Controlled Capillarity
NaOH	Sodium Hydroxide
CEW	Continuous Electrowetting
LIS	Large Intelligent Surfaces

Chapter 1 Introduction

In wireless communication system, signals are transmitted using electromagnetic waves, and antennas are used to transmit and receive these signals. With the development of communication system, various areas such as satellite communication, space exploration, WIFI systems, and indoor communication require antennas having different properties. Beam steering functionality is an essential antenna property enabling power to be transmitted or received in a specific direction [1] - [8]. For example, for on-the-move communications, the position of a mobile station is not fixed, so the base station needs to align the beam towards the end users.

Array antennas and single antennas are valid candidates for the beam steering functionality. Array antennas include phased array antennas, reflect-array antennas, and transmit-array antennas. Phased array antennas are amongst the most popular form of beam steerable antennas. However, they require phase shifters to control the phase, which are expensive and suffer from severe energy losses. Compared with a phased array antenna, a reflect-array or a transmit-array antenna, which is spatially illuminated by a single-element feed, has lower losses caused by the feed. Additionally, a transmit-array antenna has advantage that the feed and its supporting structure do not block the antenna aperture compared with a reflect-array antenna. A single antenna can also provide the steerable beams. Please note that the term single antenna refers to an antenna in which only one radiator is active at any specific moment in time. In this case, a lens antenna is typically an example of a single antenna even if it might be fed by several elements because only one of those radiators will be active at any one time. To this end, antenna designs, including array antennas and single antennas, are investigated with the aim to achieve beam steering functionality.

1.1 Motivation

To achieve the beam steering performance of antennas, multiple approaches have been proposed [9] - [22]. The approaches for the beam steerable antennas can be generally categorized into three basic classes: mechanical scan [9] - [12], frequency scan [13], and electrical scan [14] - [22]. However, each technique shows characteristics accompanied with advantages as well as drawbacks.

Mechanical scan techniques are reported in much research [9] - [12], but they actually have many limitations. For example, the steerable beams could be achieved by rotating the lens or feeds, which makes the system difficult to adjust. Additionally, mechanical moving parts are undesirable, for many applications, because they require periodic maintenance, repair, and replacement.

For frequency scan techniques, steerable beams are realized by altering the frequency. However, there are still some limitations, such as high side lobes and narrow scan angle, for the applications of frequency steering in modern wireless communication and radar system.

Electrical scan techniques are widely applied in modern wireless communication as it can increase the speed of imaging and detecting. Several electrical scan methods for beam steerable antennas have been proposed [14] - [22]. On the one hand, electrical scan can be achieved by using phase shifters in the feed network of an antenna array. For example, phase shifters are commonly employed in phased array antennas. With the phase shifters, the phase distribution can be adjusted. For digital phase shifters, despite high-number bit of phase shifters can provide small step of phase shift thus almost continuously steering beams, they are either lossy and expensive or unavailable at all [14] - [16]. Low-number bits of phase shifters are difficult to achieve continuously

steerable beams. On the other hand, beam steering can also be realized by applying discrete devices such as varactor diodes [17] - [19], PIN diodes [20], and micro-electro-mechanical systems switches [21], or exotic materials such as ferroelectric material [22]. However, PIN diodes suffer from relatively high level of insertion loss, and they create intermodulation distortion.

In summary, in the previous literature, most of the beam steerable antennas using conventional devices, such as varactors, PIN diodes, or structural modification, have various disadvantages. The disadvantages mainly include power loss from the devices, complex structure, and high cost. This motivates us to investigate the novel beam steerable antennas to provide advantages among high efficiency, simplification, and low cost.

1.2 Research Questions

We are interested in developing beam steerable antennas that can steer beams to a discrete or continuous range of different directions. Our work, therefore, involves analysis of phase shift properties, reconfigurable array unit cell, and beam steerable patch antennas.

The main objectives of our work are summarized below, in the form of a series of research questions.

1. Can we calculate the limits on the transmission behavior of a general multi-layer transmit-array unit cell (i.e. one in which the resonators on different layers have different geometries, sizes, orientations, or all three)?

2. For transmit-array unit cell, how to achieve reconfigurable phase shifting other than using electronic devices like varactors or PIN diodes?

3. Can we devise a beam steering technique, for an antenna having moderate gain, that has a wide scan angle range together with low scan loss?

4. Can we devise a new approach to obtain continuous beam steering over a scan angle range?

1.3 Contributions to Knowledge

This thesis has resulted in several contributions to knowledge.

1. Theoretical calculation and analysis of the transmission performance limits for a transmit-array unit cell. In contrast of reported works which focus on transmit-array unit cells, the contributions of this work are as follows:

a) Most of the previous work focused on the design of the transmit-array unit cells and did not analyze the transmission performance limits of the unit cell. For example, none of them analyze the relationship between transmission phase and dielectric properties. Here, we analyze the transmission performance limits for a transmit-array unit cell.

b) Previous calculation is valid only for a specific structure. However, we present a theory for a general case. It is effective for a transmit-array unit cell in which the conducting resonators, on the different layers, could have different geometries, size, orientation, or all three.

c) It has been previously confirmed that if every conducting layers of transmit-array unit cell are identical, such as Frequency Select Surface (FSS) structure, it needs at least four conducting layers to provide a 360° phase shifting range within -1 dB of transmission loss. However, we verify for the first time that different geometries

or orientations on each layer are efficient to expand the transmission behavior limitation. We found that three conducting layers are enough to achieve the abovementioned performance (i.e., 360° phase shifting range within -1 dB of transmission loss).

d) We proposed a new methodology to analyze the maximum S_{21} amplitude for a given phase shifting range of S_{21}. The result shows the theoretical limitation of the structure, which can guide the future design.

e) Different from conventional FSS unit cells having at least four conducting layers, we proposed a novel transmit-array unit cell configuration. The design has only three conducting layers, which has a simple structure yet large phase shifting range and low transmission loss.

2. Design, development and fabrication of a reconfigurable transmit-array unit cell employing liquid metal. Compared with previous transmit-array unit cells, our design has the following contributions:

a) We proposed a simple configuration of the reconfigurable unit cell employing liquid metal. Previous reconfigurable transmit-array unit cells employing liquid metal have so many layers, which makes the configuration complicated. Here the proposed design reduces the complexity of structure yet providing a good performance on large phase shifting range.

b) Conventional reconfigurable transmit-array unit cells employ electrical devices like varactors and thus suffering from a large insertion loss. Compared with these conventional designs, the proposed design employing liquid metal is capable of providing a large phase shifting range with a very low insertion loss.

c) We proposed a simple method to fabricate the liquid metal channels. The proposed method is to carve slots as channels in the dielectric substrates. The advantage of this method is that dielectric substrates provide good and stable RF performance, which will not worsen the performance of antenna a lot.

3. Design, development and fabrication of two patch antennas with switchable beams using liquid metal. The contributions involve:

a) We propose the switchable ground plane technique for the first time. This is the first time that the antenna is capable of reconfiguring its radiation pattern by reshaping the ground plane using liquid metal. No other paper in the literature, whether involving liquid metal or not, reports switching of a beam by adding and removing sections of the ground plane.

b) Most of the previous beam switchable patch antennas have disadvantages of narrow scan angle or large scan loss. The proposed patch antennas have an improved performance on wide scan angle and low scan loss. Specifically, the first proposed antenna can switch beams up to $\pm 40^{o}$ with only 0.5 dB of scan loss. The second proposed antenna can switch beam up to $\pm 68^{o}$ within 2 dB of scan loss.

4. Design, development, and fabrication of a microstrip patch antenna using liquid metal. The contributions of this work are as follows:

a) How to control liquid metal has always been a challenge. Here, we design a configuration for liquid metal channel, which makes it possible to continuously control liquid metal.

b) Different from the fabrication of liquid metal channel using Polydimethylsiloxane (PDMS), we proposed 3D printing technique to fabricate the liquid metal channel.

It is an easy way to fabricate the channels even if the 3D configuration of channels is complex.

c) Most of the microstrip patch antennas can only steer beams towards a discrete range of different directions rather than provide continuous beam steering. However, the proposed microstrip patch antenna with a single feed has the capability of providing continuously steerable beams in the elevation plane.

1.4 Publications

The research carried out during this PhD phase has resulted in the following publications.

Papers that have been published:

1. Zhishu Qu, James R. Kelly and Yue Gao, "Analysis of the Transmission Performance Limits for a Multilayer Transmitarray Unit Cell" *IEEE Trans. Antennas Propag.*, vol. 70, no. 3, pp. 2334-2339, March 2022.

2. Zhishu Qu, James R. Kelly, Zhengpeng Wang, Shaker Alkaraki and Yue Gao, "A Reconfigurable Microstrip Patch Antenna with Switchable Liquid-Metal Ground Plane," *IEEE Antennas and Wireless Propagation Letters*, 2022.

3. Zhishu Qu, Yihua Zhou, Shaker Alkaraki, James R. Kelly and Yue Gao, "Continuous Beam Steering Realized by Tunable Ground in a Patch Antenna," *IEEE Access*, vol. 11, pp. 4095-4104, 2023.

4. Zhishu Qu and James R. Kelly, "Theoretical Calculation of the Phase Limit for Transmitarray Unit Cell [C]" *Proc. 16th Eur. Conf. Antennas Propag. (EUCAP).*

IEEE, 2022: 1-4.

1.5 Overview of the Thesis

The thesis is organized as follows:

Chapter 2 presents the background of beam steerable antennas, including array antennas and single antennas which have only one active radiator at any specific moment in time. For each category of the antennas, common beam steering techniques are discussed, and associated limitations of each technique are highlighted. Then we provide the background information related to liquid metal, 3D printing technique, and the fabrication methods of channels. After that, some beam steerable antennas employing fluidic materials are reviewed. The chapter ends with a summary of the research gaps.

Chapter 3 presents a theoretical calculation establishes the performance limits for a multi-layer transmit-array unit cell. This is the first study to be applicable to unit cells in which the conducting resonators, on the different layers, are shaped differently. A theoretical calculation is derived at the beginning. Additionally, for a given phase shifting range of S_{21}, a new methodology for analyzing the maximum S_{21} amplitude, based on different substrates, is proposed. Finally, the theoretical calculations have been validated through computer simulation.

Chapter 4 presents a reconfigurable transmit-array unit cell using liquid metal. It is an extended design based on the proposed theory of Chapter 3. The designed geometry is provided firstly. Then fabrication of the unit cell and assembly are presented. The unit cell was measured within an open-ended waveguide. Simulation and measurement results are presented. It is the first time that a transmit-array unit cell, reconfigured using liquid metal, provides the combination of low insertion loss and large phase shifting

range. Different methods of actuation of liquid metal are discussed at the end of this chapter.

Chapter 5 presents two pattern reconfigurable patch antennas employing liquid metal. This is the first time that the antenna is capable of reconfiguring its radiation pattern by reshaping the ground plane using liquid metal. At the beginning, the chapter presents a discussion of the journey that leads to the final design. It further presents two designs that differ in their reflector layout. Fabrication and assembly of the antenna are highlighted. The details of actuation of liquid metal are discussed. The chapter ends with presenting simulation and measurement results.

Chapter 6 presents a microstrip patch antenna with continuously steerable beams using liquid metal. This is the first microstrip patch antenna having the capability of continuous beam steering in the elevation plane. It is an improved version of the design reported in Chapter 5. The improvement enables antenna to achieve continuous beam steering. To this end we designed a liquid metal channel and fabricated it using a 3D printer. This chapter introduces in detail the effect of the choice of material and printing method on the antenna performance. This chapter ends with fabrication and measured results.

Chapter 7 concludes the thesis and presents the ideas for future work. Specifically, this chapter presents the drawbacks of the previous designs and possible solutions for future work.

Chapter 2 Background and Literature Review

Modern communication scenarios, like satellite internet and 5G mobile access, at millimeter wave (mmWave) frequencies, require high-capacity channels to support a large number of users. Beam steerable antennas are one of the solutions due to their advantages, including: ability to enhance communication security, improve channel capacity, and adapt to changing channel conditions. A variety of beam steering techniques have been employed in the literature. In this chapter, we firstly introduce the beam steering techniques employed within array antennas. Then, we introduce the beam steering techniques employed within single antennas. Please note that the term single antenna refers to an antenna in which only one radiator is active at any specific moment in time. In this case, a lens antenna is typically an example of a single antenna even if it might be fed by several elements because only one of those radiators will be active at any one time. Next, we introduce background information related to liquid metal, 3D printing technique, and channel fabrication methods. After that, we review the current literature on beam steerable antennas employing fluidic materials. This chapter ends with a summary of the research gaps.

2.1 Beam Steering Techniques Employed in Array Antennas

In this section, we introduce the various beam steering techniques used within array antennas. Array antennas include phased array antennas, reflect-array antennas, and transmit-array antennas. In a phased array antenna, phase shifters are employed to steer the main beam. Reflect-array antennas and transmit-array antennas can convert the spherical phase front, available from the feed, into a planar plane pointing towards a specific direction. This is achieved by compensating a progressive phase shift between the unit cells forming the array antenna. Compared with a reflect-array antenna, a

transmit-array antenna has the advantage that the feed and its supporting structure do not block the antenna aperture.

2.1.1 Phased Array Antennas

In this section, we firstly introduce the geometry and working principle of phased array antennas. Then we explain the classification of beam steering techniques employed in phased array antennas. Finally, we give some examples of phased array antennas presented in the literature.

1) Geometry and Working Principle.

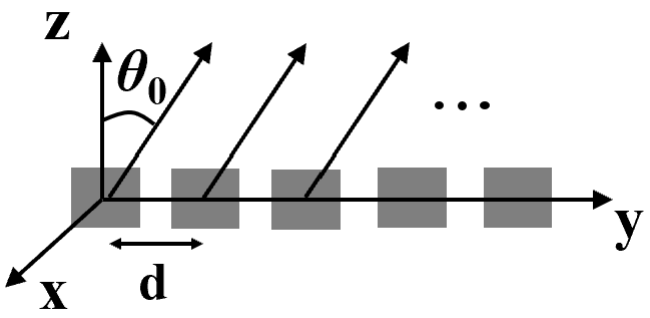

Fig. 2. 1. Geometry of a linear phased array antenna. Please note that the gray rectangular blocks represent the elements of the array, d is the spacing between two adjacent elements, and θ_0 is the angle between the beam direction and Z-axis.

Phased array antennas are one of the most commonly used types of antennas in applications which require beam steering capabilities. This is due to the fact that a phased array antenna: provides beam steering over a wide angle range, supports continuous beam steering, and has good control over the Side Lobe Level (SLL). A phased array antenna consists of a number of elements which radiate in unison. Fig. 2. 1 shows the basic geometry of a linear phased array antenna. In Fig. 2. 1 the gray rectangular blocks represent the elements of the array. A phase array antenna enables beam steering by adjusting the phase difference between the elements in the array. This allows the radiation pattern to be controlled and directed to a target without requiring

any physical movement of the antenna. For simplicity, let us consider 1D beam steering capability as an example here.

A phased array antenna applies a progressive phase shift (φ) between two adjacent elements to steer the beam towards a desired beam direction (θ_0), as shown in Fig. 2. 1. The relationship between a progressive phase shift and the desired beam direction can be expressed by the following equation:

$$\varphi = k\,\mathrm{d}\,sin(\theta_0) \tag{2-1}$$

$$k = \frac{2\pi}{\lambda_0} \tag{2-2}$$

Where θ_0 is the angle between the beam direction and z-axis, d is the spacing between elements, k is the free-space wavenumber, λ_0 is the free-space wavelength, and φ represents a progressive phase shift between two adjacent array elements.

2) Classification of Beam Steering Techniques.

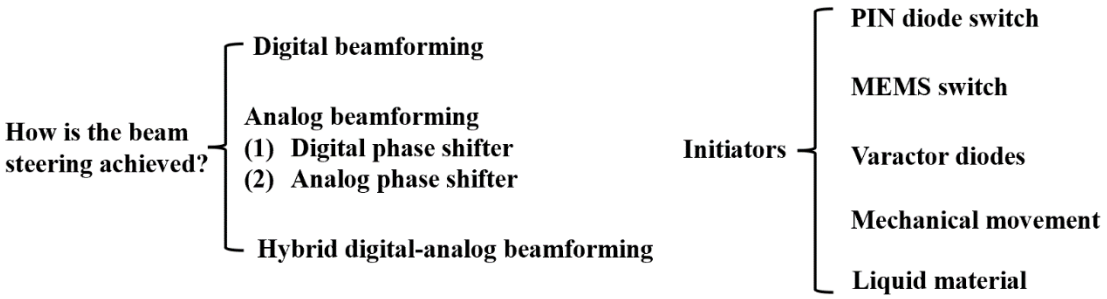

Fig. 2. 2. Classification of beam steering technology for phased array antennas.

How to achieve beam steering, i.e. adjust the phase of each element, is an essential issue in phased array antennas. Fig. 2. 2 explains the classification of techniques and initiators. There are several techniques, including digital beamforming, analog beamforming, and hybrid digital-analog beamforming. The initiators include: RF switches, varactors, and so on. Please note that any of the listed initiators could be employed within a phase

shifter.

Table 2. 1 summarizes the advantages and limitations associated with each of the different techniques for achieving the beam steering of phased array antennas.

Table 2. 1. Advantages and limitations of the different techniques for achieving the beam steering of phased array antennas.

How is the Beamforming achieved?	Advantage	Limitation
Digital Beamforming	● Highest phase shift precision. ● Adjustable phase and amplitude.	● High power consumption. ● High cost.
Analog Beamforming	● A single RF chain with several phase shifters. ● Relative lower cost than digital beamforming.	● Relatively lower precision than digital beamforming. ● Large insertion loss from the phase shifters, especially at high frequencies.
Hybrid Digital-Analog Beamforming.	● Reduced the number of RF chain. ● Relative lower cost than digital beamforming.	● Still need a large number of phase shifters. ● Large insertion loss from the phase shifters.

This paragraph discusses the advantages and limitations of different techniques for achieving beam steering with phased array antennas [23] - [30]. The first technique is digital beamforming. Digital beamforming has a dedicated RF chain for each radiating element in the array. The phase shift of digital signals can be precisely operated, thus making it possible for digital beamforming system to provide a fine phase resolution. However, digital beam formers are costly and suffer high power losses. The second technique is analog beamforming. An analog beamformer incorporates one phase shifter for each radiating element and just a single RF chain. Consequently, it has a lower cost than digital beamforming. By controlling the phase shifters, it is possible to

alter the phase of each element. In this case, different beams could be achieved. Phase shifters used in an analog phased array could be digital phase shifters or analog phase shifters. The insertion loss of a digital phase shifter is proportional to the number of bits of resolution. For example, high number of bits of resolution could have large insertion loss as well. Generally, analog phase shifters have lower insertion losses than digital phase shifters, but analog phase shifters do not have programmable features. The third technique is hybrid digital-analog beamforming. It combines the digital beamforming and analog beamforming. There is a trade-off between the number of RF chains and phase resolution. However, it still needs many phase shifters which makes the beamformers expensive and complex.

3) Literature review.

The technology behind analog phased array antennas is mature and they are widely used in many applications to achieve beam steering. However, they need expensive components and complicated feeding network, especially for cases involving a large number of elements. Recently, a configuration consisting of a phased array antenna was proposed to solve the problem of high cost [31] - [36]. It consists of a phased array with a small aperture area. The phased array is combined with another radiator such as a lens antenna or transmit-array antenna, as shown in Fig. 2. 4. This has the effect of reducing the number of radiating elements required to achieve a particular level of gain. In turn this reduces the cost. In this section, we will introduce such new configuration of phased array antennas.

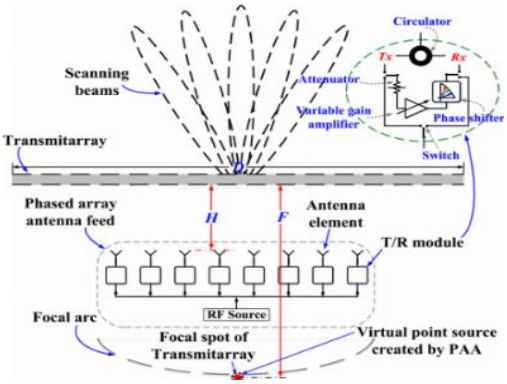

Fig. 2. 4. Geometry of a transmit-array antenna fed by a phased array antenna [34].

There are several advantages associated with employing a phased array antenna as feeding antenna. For example, 1) in comparison with a single feed antenna, it reduces the distance between the feed antenna and the radiator antenna. It is because the phased array antenna is located between the radiator antenna and its focal point (as seen in Fig. 2. 4) [34]; 2) in comparison with a single feed antenna, phased array antenna can reorganize the amplitude distribution of phased array elements to provide a better primary illumination for radiator antennas; and 3) it reduces the number of array elements required whilst still provides a similar performance as a phased array with a large aperture, such as wide scan angle range [31] or high efficiency [32], [33]. These characteristics make the radiator antenna fed by a phased array antenna highly desirable in practice. The following paragraphs discuss work on this topic.

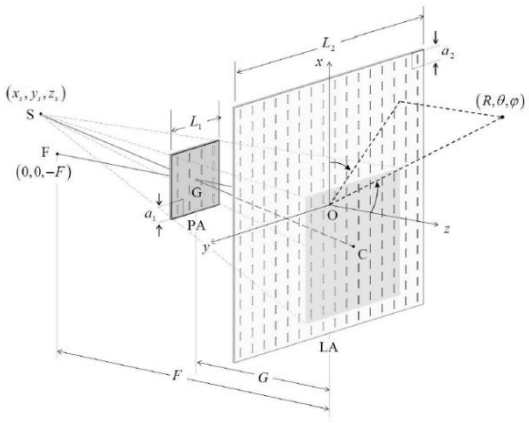

Fig. 2. 3. Geometry of a lens-enhanced phased array [32].

For example, Professor Abbaspour-Tamijani and his team at Arizona State University

and Helen K. Pan at al. at Intel proposed a novel antenna consisting of a transmit-array antenna fed by a phased array antenna [32], [35]. The phased array antenna and the transmit-array antenna are parallel to each other, as shown in Fig. 2. 3. The phases of signals applied to the elements of the phased array are chosen so as to synthesize the same wavefront as the one generated by a point source located at focal point. The wavefront, produced by the phased array antenna, can be transformed into a planar one after passing through the transmit-array antenna. The design proposed in [32] has the effect of improving the directivity, but it did not show the capability of beam steering.

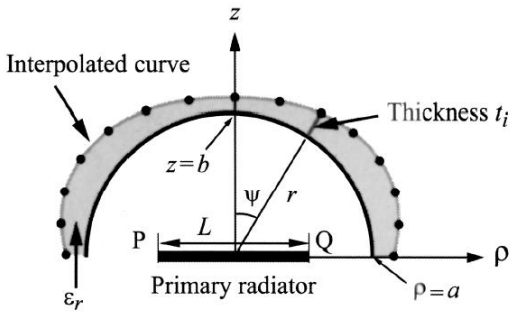

Fig. 2. 5. Geometry of a lens antenna fed by a planar phased array [36].

Additionally, in 2010, Hiroyuki Kawahara at al. designed and fabricated a dielectric dome incorporating an array-feed antenna [36]. The design operates at a frequency of 20 GHz and is capable of producing multiple beams covering a wide scan angle range. The dielectric dome antenna is fed by linear array antennas with nine elements. Fig. 2. 5 shows the block diagram. The primary feed antenna itself can steer up to $\pm 55°$ with a 5-dB scan loss. With the addition of the dielectric dome, the whole design can steer up to $\pm 70°$ with a 2-dB scan loss. However, the wide scan angle was obtained by sacrificing the peak gain of the primary phased array antenna.

2.1.2 Reflect-Array Antennas

In this section, we firstly introduce the geometry and working principle of reflect-array

antennas. Then we explain the classification of controlling reflection phase techniques employed in reflect-array antennas. Finally, we discuss one design as an example for each category to illustrate the different techniques.

1) Geometry and working principle.

Fig. 2. 6 shows the typical construction of a reflect-array antenna. The reflect-array antenna consists of a large number of unit cells. The unit cell of a reflect-array antenna consists of a ground plane and a reflective element. We can tune the amplitude of the reflected wave by altering the size of the reflecting element. The reflect-array antenna can transfer a spherical wave from the feed antenna into a plane wave towards different directions by compensating the reflection phase. Thus, how to control the reflection phase of a unit cell is an essential problem for reflect-array antennas.

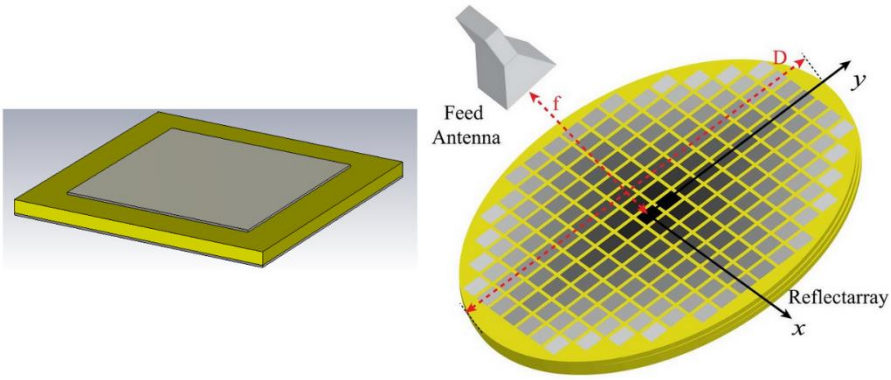

Fig. 2. 6. Geometry of a reflect-array antenna.

2) Classification of controlling reflection phase techniques.

There are different techniques for controlling the reflection phase of a unit cell. In other words, there are different techniques for reflect-array antennas to achieve steerable beams. Next, we discuss an approach for classifying these techniques. Fig. 2. 7 explains the classifications. We classify the designs from the literature in two ways. One classification is by means of the way in which the reflection phase is controlled, and

the other one is by means of the approach used to initiate reconfiguration. Please note that each of the techniques to control the reflection phase could involve any of the listed initiators.

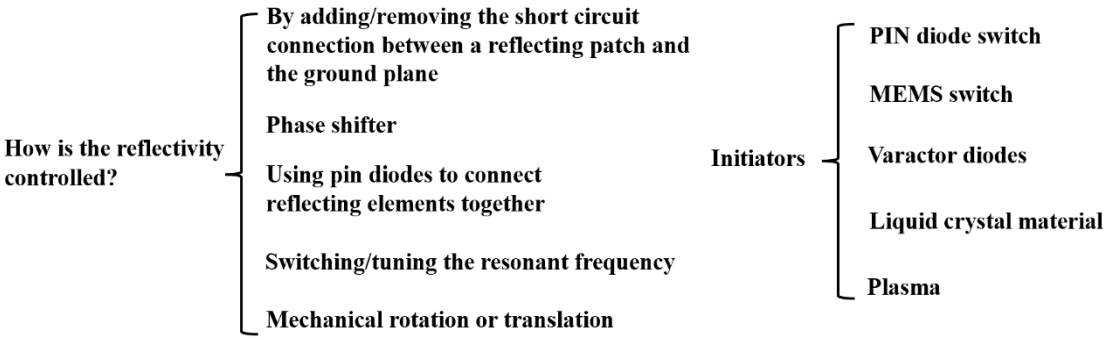

Fig. 2. 7. Classification of Reflect-array Technology.

We have identified five different main initiators for controlling the reflection phase. Among which PIN diodes and varactors are the most widely used initiators. PIN diodes and varactors are cheap and widely available. However, they suffer from relatively high level of insertion loss, and they create intermodulation distortion. Microelectromechanical systems (MEMS) switches also draw much attention due to their advantages including: small volume, low power consumption, and high integration. However, it is complex to control them. Liquid Crystal (LC) materials are mostly used at mmWave and THz frequencies. At these frequencies, modern LC materials have low insertion losses together with wide phase tuning range. However, LC materials have limited usage at lower frequencies (i.e. below 30 GHz). This is because a thicker LC material is required at lower frequencies which leads to a higher insertion loss and limited phase tuning range. Plasma could provide fast response time and high resolution, but it has high cost and power consumption.

Table 2. 2 summarizes the advantages and limitations associated with each of the different techniques for controlling the reflection phase.

Table 2. 2. Advantages and limitations of the different techniques for controlling the reflection phase.

How is the Reflection Phase Controlled?	Advantage	Limitation
By adding/removing the short circuit connection between a reflecting patch and the ground plane [37] - [44]	● Simple to design and fabricate	● Increased IL due to high concentration of current in switch [42]. ● Sensitive to switch fabrication tolerances [43]. ● Harmonic distortion*. ● Biasing network must be designed so as to avoid affecting the scattering performance*.
Phase shifter [45], [46]	● Control of phase is performed by dedicated component thus simplifying design and enhancing performance	● Harmonic distortion*. ● Biasing network must be designed so as to avoid affecting the scattering performance*.
Using PIN diodes to connect reflecting elements together [47], [48]	● Fairly simple to design and fabricate	● Harmonic distortion*. ● Biasing network must be designed so as to avoid affecting the scattering performance*.
Switching/tuning the resonant frequency [49] - [52]	● Simple to design and fabricate	● Design is sensitive to fabrication errors due to the rapid variation in phase around resonance [43]. ● Bandwidth reduced because unit cell operated around resonance where phase changes rapidly with frequency. ● Harmonic distortion*. ● Biasing network must be designed so as to avoid affecting the scattering performance*.
Mechanical rotation or translation [53] - [56]	● Enables continuous control of the beam direction ● High power handling capability	● Mechanical moving parts are undesirable because they require periodic maintenance, repair, and replacement. ● The element rotation technique can only be

		applied to circular polarization designs.

* Applies wherever a semiconductor switch is employed.

This paragraph discusses the advantages and limitations of different techniques for controlling the reflection phase. The two most popular techniques involve using PIN diodes to connect a reflecting patch to the ground plane or using PIN diodes to connect reflecting elements together. Reflect-array antennas based on these techniques are simple to fabricate. However, the high concentration of current in the PIN diode switch leads to relatively high dissipation losses which can adversely affect antenna efficiency and hence gain. Additionally, there are various other disadvantages associated with the use of semiconductors, as discussed above. The use of a phase shifter enables the phase to be controlled independently of other radiation parameters. This simplifies the process of antenna design. However, phase shift components are often relatively large thus increasing the overall size of the antenna. Mechanical rotation or translation can also be used to achieve continuous control over the reflection phase and thus the main beam of the antenna. Antennas employing this approach have high power handling capabilities. However, mechanical moving parts are undesirable, for many applications, because they require periodic maintenance, repair, and replacement.

3) Literature review.

In the following text, we discuss one design as an example for each category to illustrate the different technique for controlling the reflection phase. Different techniques are employed in unit cells to tune the reflection phase. Thus, we focus on the unit cells

instead of the whole array in the following text.

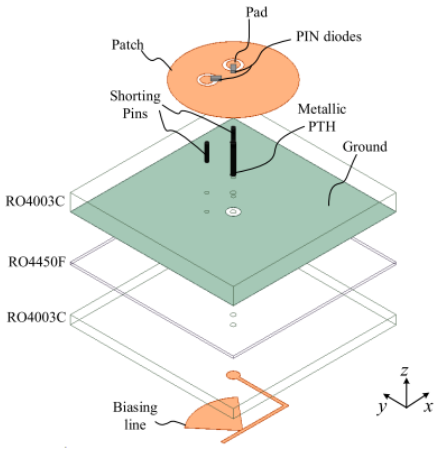

Fig. 2. 8. A design for a reflect-array unit cell in which the reflection phase is controlled using PIN diodes that connect/disconnect the reflecting patch from the ground plane [44].

By adding/removing the short circuit connection between a reflecting patch and the ground plane: Fig. 2. 8 shows an example of a design which employs this technique [44]. The unit cell incorporates a circular reflecting patch mounted on a substrate above a ground plane. Two bits of phase control are obtained by using a pair of PIN diodes, mounted on the reflecting patch, to connect or disconnect the patch from the ground plane. A hardware prototype of the reflect-array was developed incorporating 16 × 16 unit cells. The design operates at 9.5GHz and has a frequency operating bandwidth of 730 MHz. It provides a realized gain of 21.8 dBi. The scan angle range is ±45° and the scan loss is 3 dB.

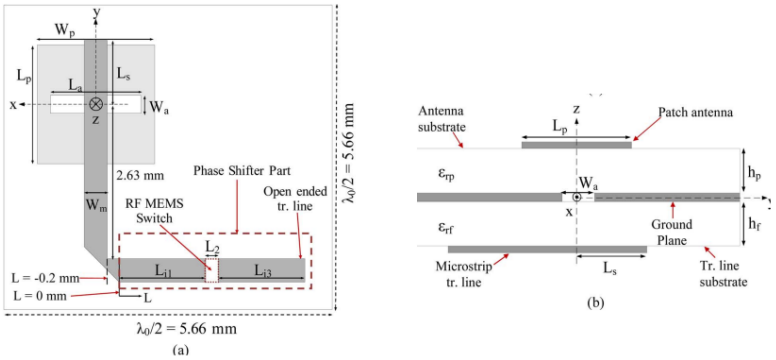

Fig. 2. 9. A design for a reflect-array unit cell in which the reflection phase is controlled by using a phase shifter [46].

Phase shifter: Fig. 2. 9 shows an example of a design which employs this technique [46]. The unit cell incorporates a square patch which is coupled, via an aperture, to an open ended microstrip transmission line. This microstrip line acts as a phase shifter. A MEMS switch is used to alter the length of the microstrip line. A hardware prototype of the reflect-array was developed incorporating 10 × 10 unit cells. The design operates at 26.5 GHz. The frequency operating bandwidth was not specified. It provides a realized gain of 11.42 dBi. The scan angle range is ± 40° and the scan loss is 0.37 dB.

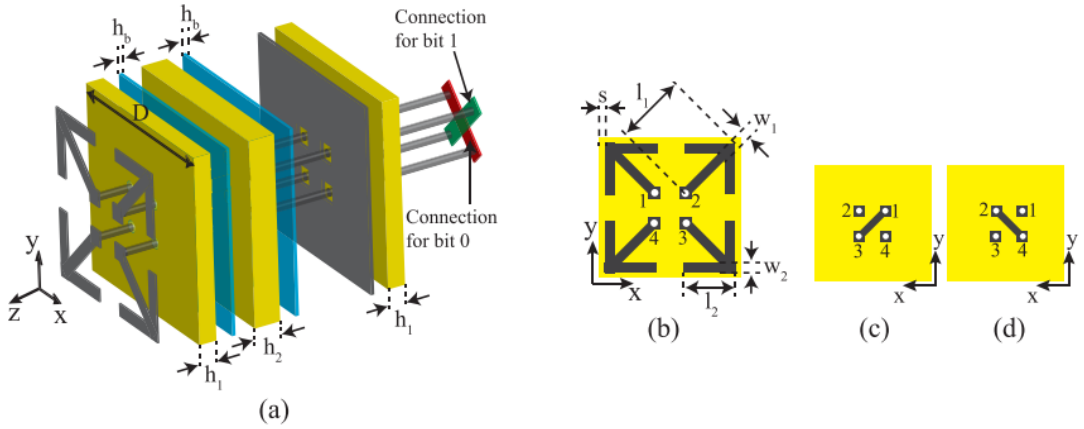

Fig. 2. 10. A design for a reflect-array unit cell in which the reflection phase is controlled using PIN diodes that connect/disconnect reflecting elements [48].

Using PIN diodes to connect reflecting elements together: Fig. 2. 10 shows an example of a design which employs this technique [48]. The unit cell incorporates 4 arrow shaped reflecting elements which form the reflecting element. These elements are mounted on a grounded dielectric substrate. The arrows can be connected together, at their base, using 2 PIN diodes. The PIN diodes are mounted on a second substrate located beneath the ground plane. This reduces the risk of unwanted scattering from the PIN diodes. A hardware prototype of the reflect-array was developed incorporating 408 unit cells. The design operates at 10 GHz and has a frequency operating bandwidth is 4 GHz (40%). It provides a realized gain of 25 dBi. The scan angle range is ±45° and the scan loss is 3 dB.

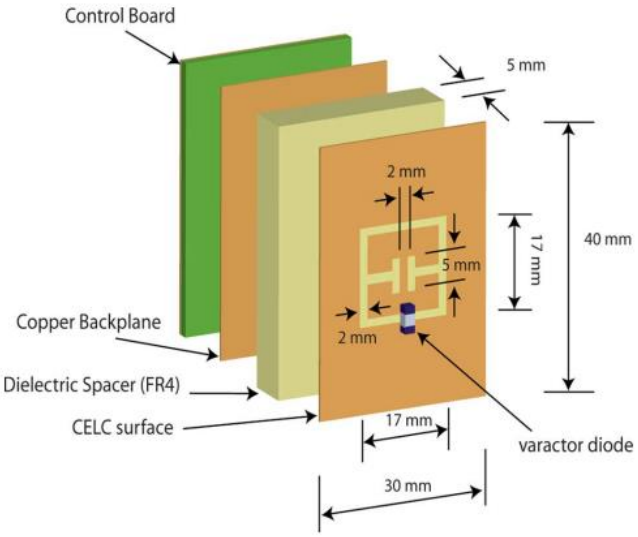

Fig. 2. 11. A design for a reflect-array unit cell in which the reflection phase is controlled by switching and tuning the resonant frequency [52].

Switching/tuning the resonant frequency: Fig. 2. 11 shows an example of a design for a unit cell in which the reflection phase is controlled by tuning the resonant frequency [52]. This is achieved with the aid of a varactor diode. The reflector is a metallic surface incorporating a series of cutouts, namely: a square loop, and a capacitive element. A varactor diode is mounted across the square loop. Altering the capacitance of the varactors has the effect of shifting the operating frequency of the reflecting element. In turn this alters the phase of the reflection phase. A hardware prototype of the reflect-array was developed incorporating 5 × 5 unit cells. The design operates at 2.25 GHz. However, no other performance parameters were reported.

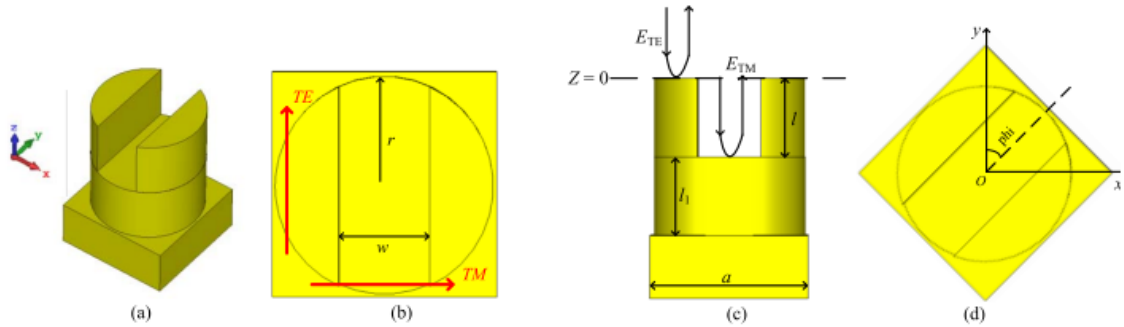

Fig. 2. 12. A design for a reflect-array unit cell in which the reflection phase is controlled by mechanical rotation or translation [56].

Mechanical rotation or translation: Fig. 2. 12 shows an example of a design for a unit cell which uses mechanical rotation to alter the reflection phase [56]. The reflecting element consists of a cylinder incorporating a rectangular grove. The cylinder can be rotated, mechanically, causing the grove to face along a different direction. A hardware prototype of the reflect-array was developed incorporating 14 × 14 unit cells. The design operates at 26 GHz and has a frequency operating bandwidth is 5.3 GHz (20.38% for a 1.5 dB gain drop). It provides a realized gain of 18.9 dBi. The scan angle range is ±60° and the scan loss is 2 dB.

2.1.3 Transmit-Array Antennas

In this section, we firstly introduce the geometry and working principle of transmit-array antennas. Then we explain the classification of controlling transmission phase techniques employed in transmit-array antennas. Finally, we discuss one design as an example for each category to illustrate the different techniques.

1) Geometry and working principle

Fig. 2. 13 shows the typical construction of a transmit-array antenna. A conventional transmit-array antenna consists of an illuminating feed antenna and a transmitting

surface. The feed antenna is usually located on the focal point of the transmitting surface. On the transmitting surface, there is an array of unit cells. The transmission coefficients of these unit cells are individually designed to convert the spherical phase front from the feed antenna to a plane wave towards different directions. By controlling the compensation transmission phase of transmitting surface, steering beams can be achieved.

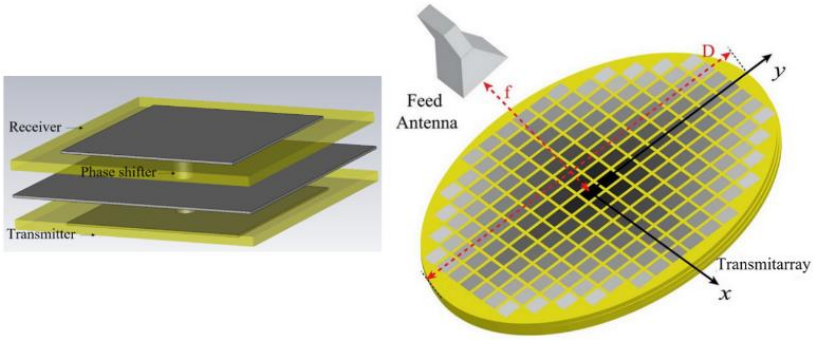

Fig. 2. 13. Geometry of transmit-array antenna.

2) Classification of controlling transmission phase techniques

This section discusses an approach for classifying transmit-array technologies of controlling the transmission phase. Fig. 2. 14 explains the classification. We classify designs from the literature in two ways. One classification is by means of the way in which the transmission phase is controlled, and the other one is by means of the approach used to initiate reconfiguration. Please note that each of the techniques to control the transmission phase can involve any of the listed initiators.

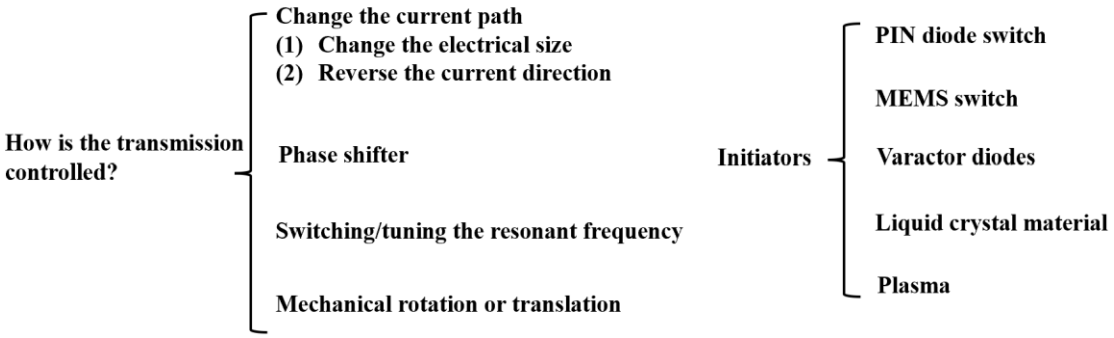

Fig. 2. 14. Classification of Transmit-array Technology.

Table 2. 3 summarizes the advantages and limitations associated with each of the different techniques for controlling the phase of the signal transmitted through the transmit-array.

Table 2. 3. Advantages and limitations of the different techniques for controlling the transmission phase.

How is the Transmission Phase Controlled?	Advantage	Limitation
Change the current path (include change the electrical size [57], [58] and reverse the current direction [59] - [62]).	● Simple to design and fabricate (hardwire structure). ● Using PIN diodes to change the current path has relative low insertion loss compared with varactors.	● Most of the PIN diodes work below or around 10 GHz frequency. ● 1-bit/2-bits structure will have the phase quantization loss. It is usually 3 to 4 dB for 1-bit structure. ● Harmonic distortion*. ● Biasing network must be designed so as to avoid affecting the scattering performance*.
Phase shifter [63] - [66]	● Control of phase is performed by dedicated component thus simplifying design and enhancing	● Harmonic distortion*. ● Biasing network must be designed so as to avoid affecting the scattering performance*.

	performance.	
Switching/tuning the resonant frequency [67] - [69]	• Simple to design and fabricate. • Using varactors could achieve continuous phase shift tuning.	• Design is sensitive to fabrication errors due to the rapid variation in phase around resonance. • Bandwidth reduced because unit cells operate around resonance where phase changes rapidly with frequency. • Large insertion loss caused by varactors, especially in high frequency. • Harmonic distortion*. • Biasing network must be designed so as to avoid affecting the scattering performance*.
Mechanical rotation or translation [70], [71]	• Enables continuous control of the beam direction. • High power handling capability.	• Mechanical moving parts are undesirable because they require periodic maintenance, repair, and replacement. • The element rotation technique can only be applied to circular polarization designs. • If the feed source is rotated and the array is hardwired, then the array cannot provide an ideal phase compensation for different locations of feed source.

* Applies wherever a semiconductor switch is employed.

This paragraph discusses the advantages and limitations of different techniques for controlling the transmission phase. The first method to control the transmission phase is to change the current path. Specifically, it involves changing the electrical size of elements on the unit cells or reversing the direction of the current. Designs that use PIN diodes to change the current path exhibit lower insertion loss than designs that use varactors. However, most of the PIN diodes work below or around 10 GHz frequency. Transmit-array antennas based on these techniques are simple to fabricate. 1-bit or 2-bits designs will have appreciable phase quantization loss, which is usually around 3 dB to 4 dB. The second method is to employ a phase shifter. The control of phase, for this technique, is performed by dedicated component thus simplifying design and enhancing performance. The insertion losses of the designs reversing the direction of the current or the designs employing phase shifters range from 1 dB to 3 dB, and the scan angle could be up to ±60°. The third technique involves switching/tuning the resonant frequency. Transmit-array antennas based on this technique are simple to

fabricate. When varactors are used, the designs can achieve continuous control of the phase. However, such designs are sensitive to fabrication errors due to the rapid variation in phase with frequency around resonance. Also, for the same reason, the operating frequency bandwidth is likely to be reduced. When varactors are used the insertion loss tends to be large, especially in high frequency. The average insertion loss for designs employing this technique is 5 dB. The scan angles of most designs are below ±30°. The final technique for altering the transmission phase is mechanical rotation or translation. This technique enables continuous control of the beam directions and has high power handling capability. Designs employing this technique have relative low insertion loss (less than 3 dB). However, mechanical moving parts are undesirable, for many applications, because they require periodic maintenance, repair, and replacement.

3) Literature review.

In the following text, we discuss one design as an example for each category to illustrate the different techniques for controlling the transmission phase. Different techniques are employed in unit cells to tune the transmission phase. Thus, we focus on the unit cells instead of the whole array in the following text.

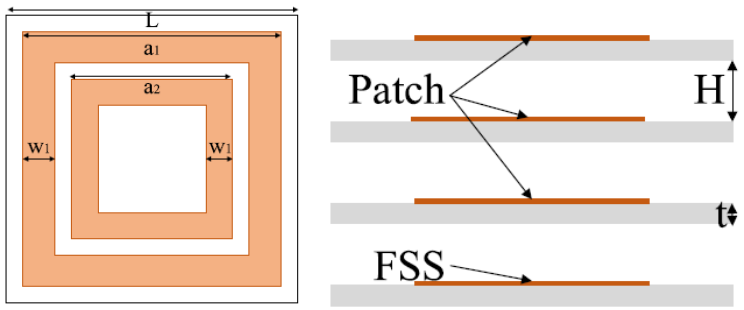

Fig. 2. 15. A design for a transmit-array unit cell in which the transmission phase is controlled by changing the electrical size of elements [58].

Change the current path: changing the electrical size of elements in the unit cell: Fig. 2.

15 shows an example of a design for a unit cell which uses this technique [58]. The design incorporates 4 substrates layers and 4 metal layers, namely: patch layers, and FSS layer. Three square patches are mounted on each of the three substrates. One FSS layer mounts on bottom substrate. By changing the electrical size of the elements on patch layers, the transmission phase could be changed. A hardware prototype of the transmit-array was developed incorporating 9 × 9 unit cells. The design operates at 11 GHz. The peak gain of the design in transmit-array mode is 20.9 dBi. However, the paper did not discuss the beam steering capability of the design.

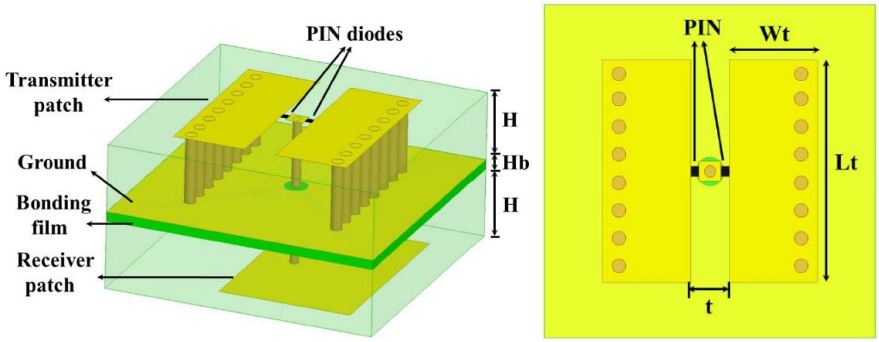

Fig. 2. 16. A design for a transmit-array unit cell in which the transmission phase is controlled by reversing the current direction [60].

Change the current path: reversing the current direction: Fig. 2. 16 shows a design that employs this technique [60]. The transmitter section consists of two rectangular patches and two PIN diodes. When one of the PIN diodes is switched ON, the short-circuit patch will operate as an equivalent magnetic dipole. Operating the other one of the PIN diodes has the effect of reversing the current direction. A hardware prototype of the transmit-array was developed incorporating 16 × 16 unit cells. The design operates at 29 GHz and has a frequency operating bandwidth of 4.2 GHz. It provides a realized gain of 20.8 dBi. The scan angle range is ±50° and the scan loss is 5.8 dB.

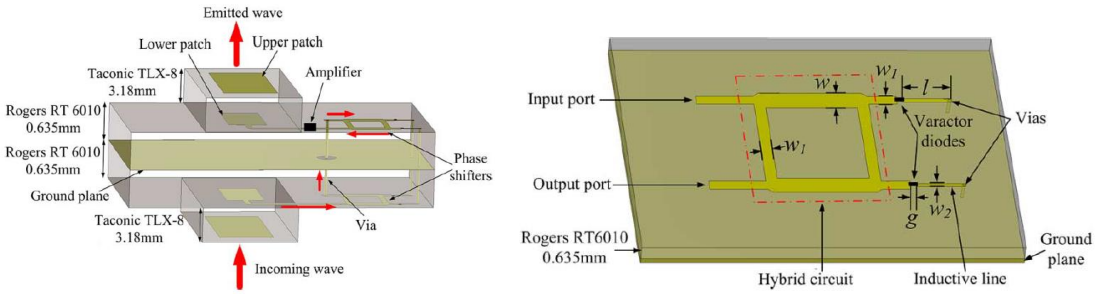

Fig. 2. 17. A design for a transmit-array unit cell in which the transmission phase is controlled by using a phase shifter [66].

Phase shifter: Fig. 2. 17 shows an example of a design that employs this technique [66]. The design consists of 4 substrate layers and 5 metal layers, incorporating: receiving, transmitting, two phase shifting layers, and ground plane. It incorporates a microstrip patch antenna on the receiving layer and a microstrip patch antenna on the transmitting layer. A parasitically coupled patch is employed on each layer to increase the operating frequency bandwidth. Energy from the receiving layer passes through a pair of phase shifters before being made available on the transmitting layer. The phase shifters are a pair of hybrid reflection-type phase shifters which are connected in cascade by a through hole via. Each phase shifter incorporates a pair of varactors which are connected across two ports of the phase shifter, as shown in Fig. 2. 17. This makes it possible to continuously tune the transmission phase. The paper only reports the performance of the unit cell which operates at 5 GHz. The total tuning range of the transmission phase is 400° with an insertion loss of 2.5 dB.

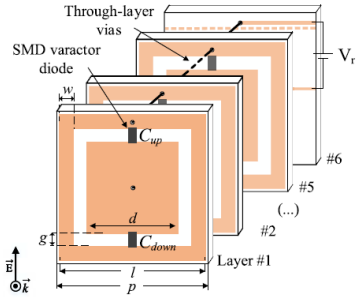

Fig. 2. 18. A design for a transmit-array unit cell in which the transmission phase is controlled by tuning the resonant frequency [67].

Switching/tuning the resonant frequency: Fig. 2. 18 shows an example of a design that employs this technique [67]. The design consists of 5 stacked layers of square-slot FSS and a biasing layer. Each square-slot FSS layer incorporates a pair of varactor diodes. Altering the capacitance of the varactor diodes has the effect of shifting the operating frequency of the associated FSS layer, thus altering the transmission phase. The FSS layers are connected to the biasing layer by means of a pair of through hole vias. A hardware prototype of the transmit-array was developed incorporating 5 × 5 unit cells. The transmit-array antenna operates at 5.2 GHz and has a frequency operating bandwidth of 70 MHz. It provides a realized gain of 20.2 dBi. The scan angle range is ±26° and the scan loss is 4.1 dB.

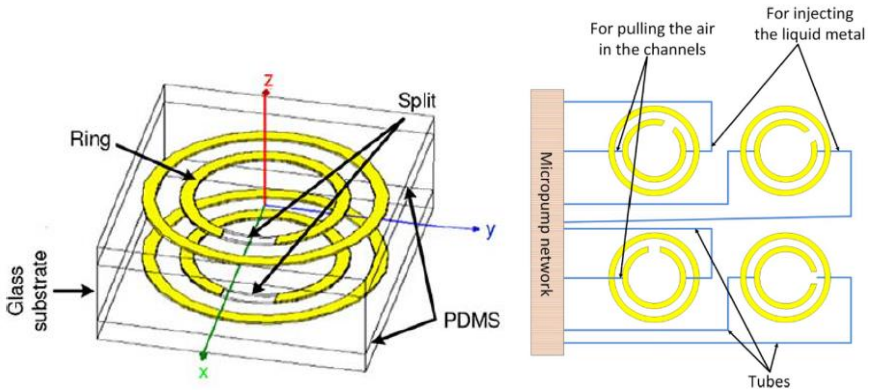

Fig. 2. 19. A design for a transmit-array unit cell in which the transmission phase is controlled by mechanical rotation or translation [71].

Mechanical rotation or translation: Fig. 2. 19 shows an example of a design that employs this technique [71]. The design consists of two layers of resonators stacked one above the other. Each layer consists of two concentric rings. The innermost ring has a split ring construction whilst the outermost ring is complete and unbroken. The conductive regions are formed by injecting liquid metal into a channel structure, whereas the split region is created by an air gap in the ring. By rotating the split towards different directions, the transmission phase can be tuned. This paper only discusses the performance of the unit cell, which operates at 8.8 GHz. The total tuning range of the transmission phase is 360° with 3 dB of insertion loss.

2.2 Beam Steering Techniques Employed in Single Antennas

In this section, we introduce the various beam steering techniques employed in single antennas. It is worth noting that the term single antenna refers to an antenna in which only one radiator is active at any specific moment in time. In this case, a lens antenna is typically an example of a single antenna even if it might be fed by several elements because only one of those radiators will be active at any one time. We firstly introduce the classification of beam steering techniques employed in single antennas. Then we discuss one design as an example for each category to illustrate the different techniques.

1) Classification of beam steering techniques

This section will discuss an approach for classifying beam steering technologies for single antennas. Fig. 2. 20 explains the classification. We classify the designs from the literature in two ways. One classification is by means of the way in which the steering beams are controlled, and the other one is by means of the approach used to initiate beam steering. Please note that each of the techniques to achieve the beam steering can

involve any of the listed initiators.

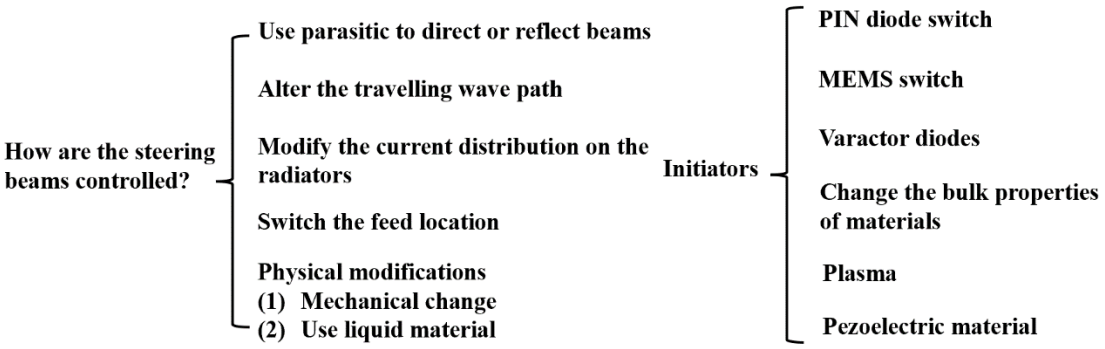

Fig. 2. 20. Classification of beam steering technologies for single antennas.

Table 2. 4 summarizes the advantages and limitations associated with each of the different techniques for achieving the beam steering of single antennas.

Table 2. 4. Advantages and limitations of the different techniques for achieving the beam steering.

How are the steering beams achieved?	Advantage	Limitation
Use parasitic to direct or reflect the beams [72] - [76]	● Parasitics provide the high gain and directivity	● Bandwidth could be influenced if a number of director element is used.
Alter the travelling wave path [77] - [79]	● Simple to design and fabrication ● High directivity	● Most of the loading elements such as varactors work around a low frequency. ● Large insertion loss caused by varactors, especially in high frequency. ● Sensitive to operating frequency thus it is difficult to achieve a wide bandwidth
Modify the current distribution on the radiators [80] - [83]	● Using PIN diodes or switches provides fast speed	● Most of the PIN diodes work below or around 10 GHz frequency. ● Large insertion loss caused by varactors, especially in high frequency. ● Complex feeding network. ● Intermodulation distortion for PIN.
Switch the feed location	● Simple to design and fabrication	● Complex feed section, including array configuration or feed network.

[21], [36], [84], [85]	• Electric switches provide fast respond speed	• Lens antenna with 3D configuration has limitation in many practical applications
Physical modifications [86] - [89]	• Simple to design and fabrication	• Mechanical moving parts are undesirable because they require periodic maintenance, repair, and replacement. • A lower speed than the electrically controlled antennas

This paragraph discusses the advantages and limitations of different beam steering techniques for single antennas. The first method is to use parasitics to direct or reflect the beam. Parasitics could provide the high gain and high directivity. However, the operating bandwidth of such structure could be influenced if a number of director elements are used. The second method is to alter the travelling wave path. Designs using this technique provide high directivity and include leaky wave antennas. However, the operating bandwidth is limited because such designs are sensitive to operating frequency. The third method is to modify the current distribution on the radiators. It is usually achieved by using PIN diodes, varactors, or switches. Using PIN diodes or switches would provide fast respond speed. However, most of the PIN diodes work below or around 10 GHz frequency. Varactors could be another choice. However, large insertion loss is caused by varactors, especially at high frequencies. The fourth method is to switch the feed location. This method still provides fast speed using electrical initiators. Some dielectric lens antennas use this method [21], [36]. However, such an antenna has a 3D configuration which is disadvantageous in many practical applications. The final technique, for steering the beam of a single antenna, is physical modification. It includes adding or removing liquid dielectrics, such as water [90], from certain areas of the antenna or mechanically changing the shape of the radiating element. Antennas using this method are simple to design and fabricate. However, mechanical moving parts are undesirable because they require periodic maintenance, repair, and

replacement. Additionally, mechanically controlled antennas provide a lower reconfiguration speed than electrically controlled antennas.

2) Literature review

In this section, we discuss one design from each category as an example to illustrate the different techniques for achieving the beam steering within a single antenna.

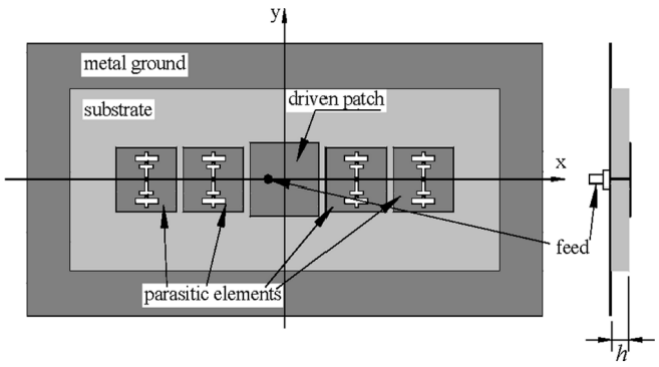

Fig. 2. 21. A single antenna in which the steering beams are controlled by using parasitic to direct or reflect beams [76].

Use parasitic to direct or reflect beams: Fig. 2. 21 shows an example of a single antenna which uses this technique [76]. Designs using this technique consist of one driven element and one or more parasitics. Those parasitics are employed as directors or reflectors. For example, Yagi antennas are typical antennas using this technique. In [76], the antenna can steer beams in the E-plane by changing the states of the switches installed in the slots, which were etched on the parasitic patches. The antenna operates at a frequency range from 9.15 GHz to 9.45 GHz. The beam can be switched between -7°, +33.5° and -40° in the E-plane.

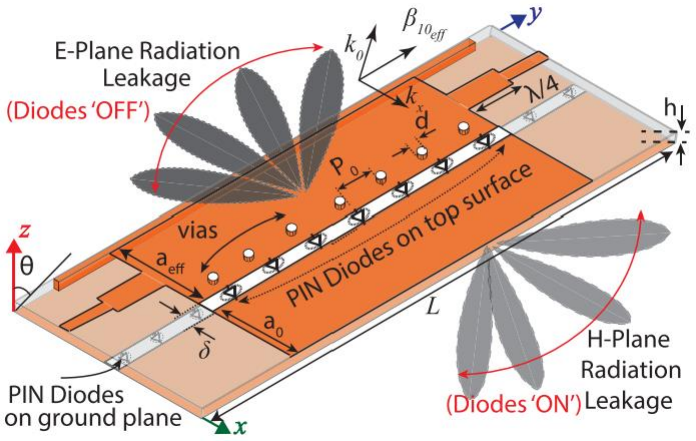

Fig. 2. 22. A single antenna in which the steering beams are controlled by altering the travelling wave path [77].

Alter the travelling wave path: Fig. 2. 22 shows an example of a single antenna which uses this technique [77]. A travelling wave antenna is a non-resonant antenna which uses a travelling wave on a guiding structure as the main radiating mechanism. For example, leaky wave antennas are type antenna which uses this technique. In [77], the antenna can steer beams by altering the travelling wave path. In this design, beam steering is achieved by extending the top and bottom metallic planes using metallic vias along the leakage side. The antenna can steer a beam by an angle of up to 54° in the E-plane from 10 GHz to 11.7 GHz, and up to 58° in the H-plane from 9 GHz to 10.6 GHz.

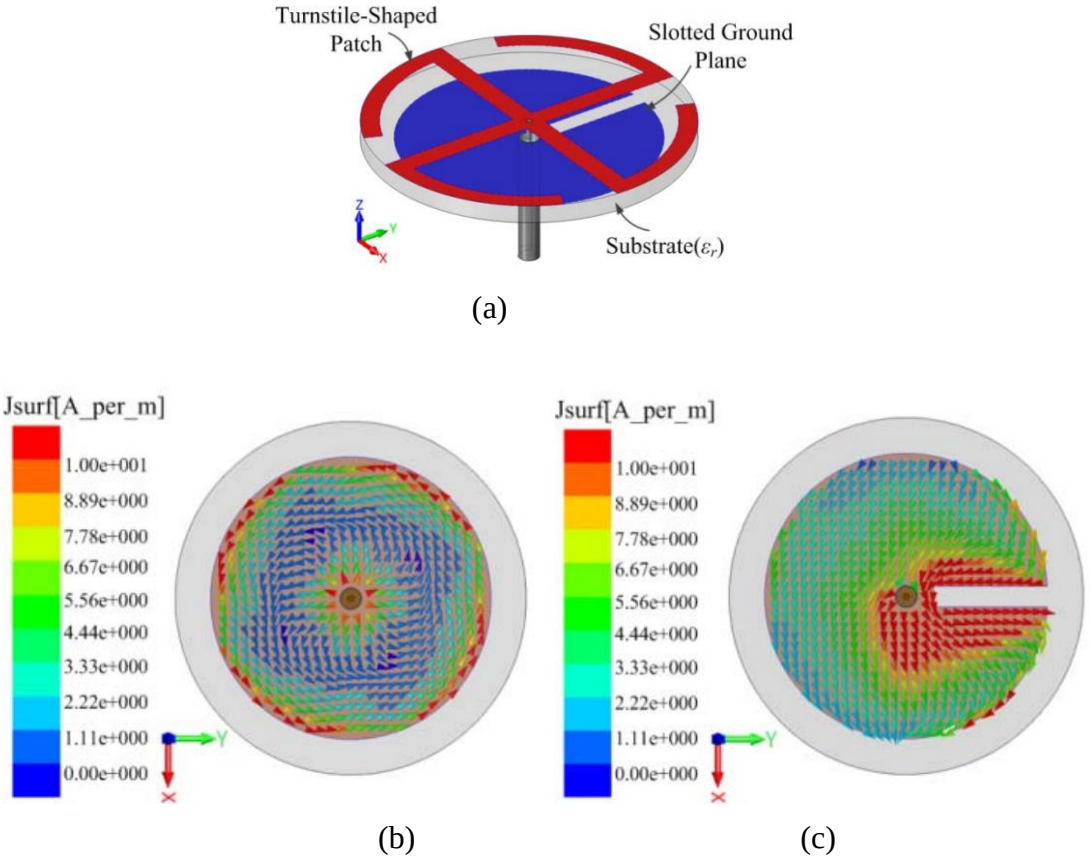

Fig. 2. 23. (a) A single antenna in which the steering beams are controlled by modifying the current distribution on the radiators [81]; (b) current distribution of ON-state of PIN diode; (c) current distribution of OFF-state of PIN diode.

Modify the current distribution on the radiators: Fig. 2. 23 shows an example of a single antenna which uses this technique [81]. Different from the previous categories, this category refers to a standing wave antenna. For example, slotted antennas are a type of antenna which uses this technique. In [81], a PIN diode is placed in the slot which is on the ground plane. By switching the PIN diode ON and OFF, the current distribution on this plane can be changed thus changing the main beam direction. Fig. 2. 23 (b) and (c) show different current distributions for different states of the PIN diode. This proposed antenna incorporates four slots in the ground plane, and it is capable of steering its beams to four different angles directing towards 0º, 90º, 180º and 270º in the azimuth plane.

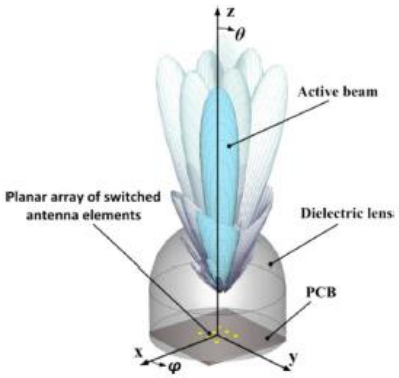

Fig. 2. 25. A single antenna in which the steering beams are controlled by switching the feed location [21].

Switch the feed location: Fig. 2. 25 shows an example of a single antenna which uses this technique. In [21], a 3D lens antenna with several feed antennas is proposed. The antenna is composed of an extended hemispherical lens made from quartz and a printed circuit board (PCB) containing the feeding circuit. The feed antenna is an array antenna. The feeding elements within the array are arranged in a 2D pattern together with a switching circuit. By switching the feed elements thus changing the feed location, it is possible to obtain discrete beam steering up to $\pm 20^{o}$.

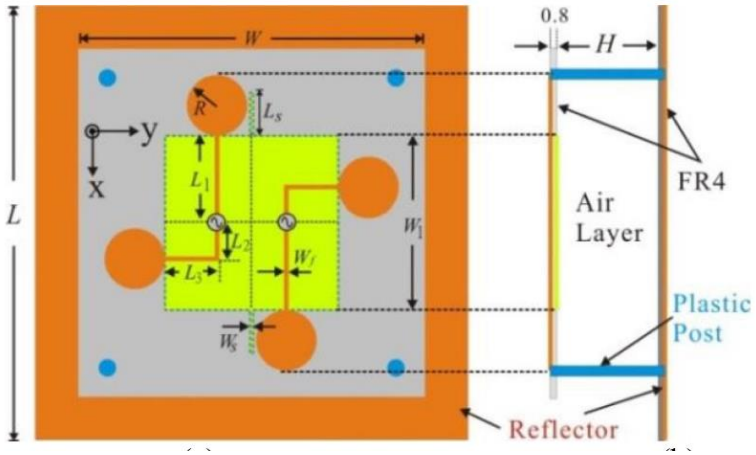

Fig. 2. 24. A single antenna in which the steering beams are controlled by mechanical change [89].

Physical modification - Mechanical change: Mechanically controlled antennas use the mechanical moving parts to alter the direction of the main beam. For example, Fig. 2.

24 shows an example of a single antenna which uses this technique. The antenna proposed in [89] consists of a dipole antenna with a bent dumbbell shape and a metal reflector. A parasitic square patch etched on the bottom side of the dumbbell arms provided a feeding delay line for producing dipole. The distance between the driven elements and a reflector (H parameter in Fig. 2. 25) could be adjusted in order to reconfigure the beam. The main beam direction can be switched between $\pm 48^{o}$ at around 3.6 GHz.

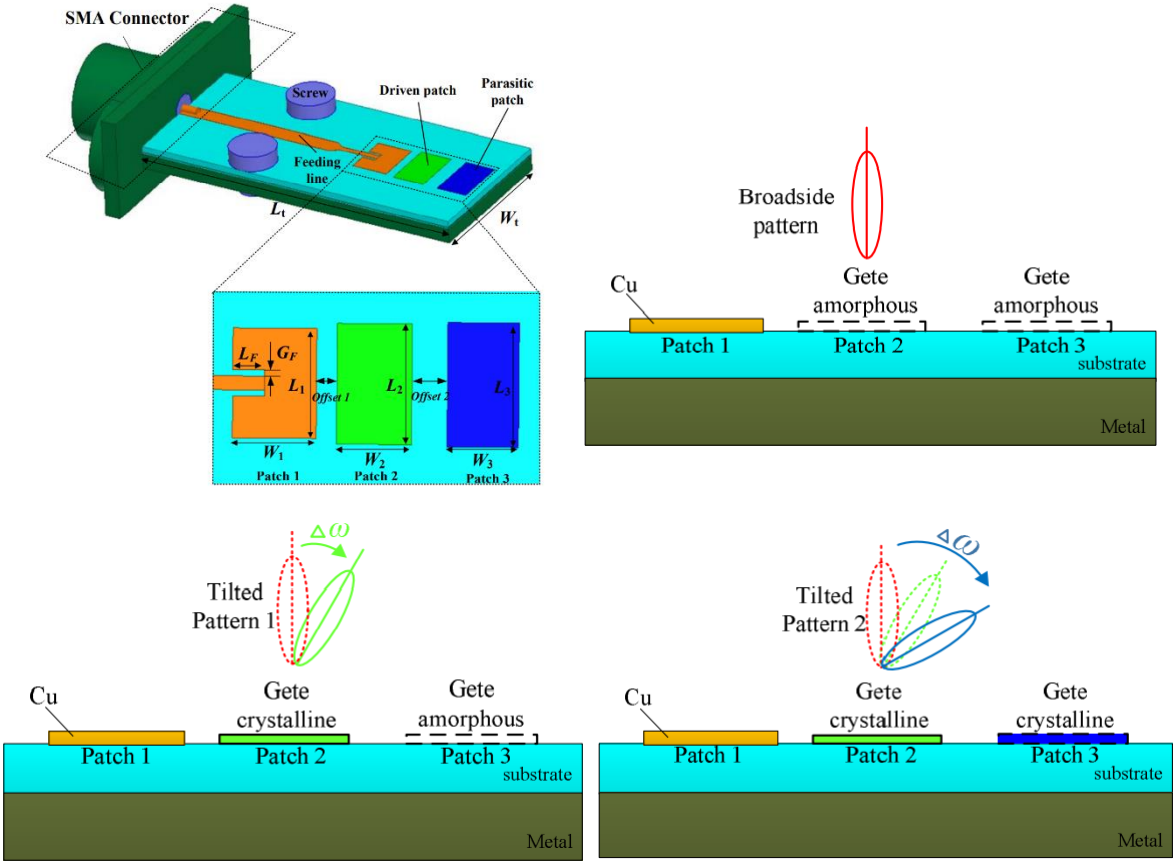

Fig. 2. 26. A single antenna in which the steering beams are controlled by using liquid material [86].

Physical modification – Use liquid material: Using liquid material refers to adding/removing liquid dielectrics, such as water, from certain areas of the antenna or changing the properties of material through changing the electric voltage. For example, Fig. 2. 26 shows an example of a single antenna which uses this technique [86]. In [86], the proposed antenna consists of one driven patch and two parasitics. The two parasitics

are formed from phase-change material. By changing an optical source, the parasitics considered as switchable elements transfer between amorphous and crystalline states. The conductivities of crystalline and amorphous states are 4.1×10^5 S/m and 10 S/m, respectively. The main beam direction can be switched between 0^o, 20^o, and 60^o at 30 GHz.

2.3 Background on Liquid Metal Alloy

In this section, we will introduce the background information related to liquid metal.

Liquid metals belong to an emerging class of materials with characteristics originating from their simultaneous metallic and liquid natures. They are characterized by having low melting points and good conductivity. Liquid metals could consist of either a single natural material or an alloy of several materials. Among different liquid metals, common liquid metal alloys that have been reported in the literature include Mercury (Hg), Eutectic Sodium Potassium (NaK), and Eutectic Gallium (Ga) alloys. Hg is the most known liquid metal at room temperature, but it is rarely used in practical due to its toxicity. NaK reacts explosively with water and reacts with air to form potassium superoxide, which can react explosively with organic materials [91]. For these reasons, NaK is rarely used in practice. Alloys of gallium are an attractive choice due to their electrical properties and their non-toxicity.

Gallium itself has a melting temperature of 29.8 ^{o}C, while alloying gallium with other metals, one can lower the melting point below room temperature [91]. Gallium alloys also have other advantages. For example, in their liquid state, gallium alloys have low viscosity and negligible solubility. As metal, gallium alloys have high thermal conductivity and comparable electrical conductivity with copper. Another important feature of gallium alloys is the formation of a thin oxide layer on their surface when exposed to air. This oxide layer helps to ensure that liquid gallium alloy remains fixed

in location until the applied external pressure exceeds the surface tension.

Generally, there are two types of gallium alloys that are widely reported and commercially available. They are Eutectic Gallium Indium (EGaIn) and Gallium Indium Tin (Galinstan). The melting points for EGaIn and Galinstan are 15.7 ºC and -19 ºC, respectively. Galinstan has a lower melting point than EGaIn alloy, but its electrical conductivity is greatly affected when the temperature range is between 22 ºC and 87 ºC. While the effect of temperature on the electrical conductivity of EGaIn alloy is negligible.

Refer to the designs reported in the thesis, we use a commercially available EGaIn alloy, which consists of 75% Gallium and 25% Indium. The conductivity of EGaIn alloy is 3.4×10^6 S/m.

2.4 Background on Fabrications

In this section, we will introduce the background information related to fabrications, including 3D printing technique and the fabrication of channels.

2.4.1 Background on 3D Printing Technique

3D printing is also called additive manufacturing. It is a method to produce a physical object layer by layer. Different from the reductive manufacturing which removes sections through cutting from a block of material, 3D printing builds an object, layer by layer. Specifically, the layers, which range in high from 0.06 mm to 0.4 mm, are laid down, one by one, until the required height is achieved. This method has several advantages over traditional fabrication methods, including a smaller form-factor, lighter weight, and lower cost. Due to these advantages, recently, 3D printing technology has been increasingly used for the fabrication of antennas [92] - [94].

Table 2. 5 shows the categories of 3D printing techniques. Depending on the materials used by the printer, 3D printing technologies can be classified into the following four categories. They are: 1) Liquid Polymer System; 2) Molten Material System; 3) Discrete Particle System; and 4) Solid Sheet System. Liquid Polymer System applies an ultraviolet laser to cure the photosensitive resin layer by layer in the print chamber or applies the nozzle to drop the photosensitive resin to a specific location, and then cures it by ultraviolet light. The typical techniques of this system include Stereolithography (SLA), Digital Light Processing (DLP), and Inkjet. Molten Material System extrudes the melted material from the nozzle and covers it in layers under the control of the program. The material will be cured after cooling. Generally, this system applies two nozzles. One is used for printing the object, the other one is used for printing the supporting structure of the object. Fused Deposition Modeling (FDM) is one of the most common techniques for it. Discrete Particle System applies a high-power laser to melt the discrete particle or an adhesive to bond them to form the pattern for each layer. The typical techniques are Selective Laser Sintering (SLS) and Selective Laser Melting (SLM). Solid Sheet System cuts each thin layer of material into a specific shape and vertically builds multiple layers into a 3D object. One typical technique is Laminated Object Manufacturing (LOM).

Plastics, such as Acrylonitrile Butadiene Styrene (ABS), Polylactic Acid (PLA) and Nylon, are the most commonly used in 3D printing. The permittivity of them is generally at the range from 2 to 4, which are suitable for the designs presented in this thesis. As a result, for the following designs presented in this thesis, we use PLA as printing material and apply the FDM printing technique. A particular maker of 3D printer named Ultimaker S3 is used. The best fabrication accuracy of the 3D printer in height is 0.06 mm. The 3D printer has a best possible resolution of 6.9 μm × 6.9 μm × 2.5 μm in x-, y-, and z-axes, respectively.

Table 2. 5. The category of 3D printing techniques.

Category of printing system	Typical Technique	Material
Liquid Polymer System	Stereolithography (SLA)	Photosensitive resin
	Digital Light Processing (DPL), Inkject	
Molten Material System	Fused Deposition Modelling (FDM)	PLA, ABS, Nylon, etc.
Discrete Particle System	Direct Metal Laser Sintering (DMLS)	Almost all metal alloys
	Electron-Beam Melting (EBM)	Almost all metal alloys including Titanium
	Selective Laser Melting (SLM)	Titanium, stainless steel, aluminium, etc.
	Selective Laser Sintering (SLS)	Thermoplastic materials, metal powder, ceramic powder, Nylon, etc.
Solid Sheet System	Laminated Object Manufacturing (LOM)	Paper, plastic film, etc.

2.4.2 Background on Channel Fabrication

In the following text, we will discuss two fabrication processes. The first one is about the methods of fabrication of liquid metal channels. The second one is about how to assemble channels with an antenna.

There are several different kinds of methods to fabricate the liquid metal channel. One of the most common methods is manufacturing a mold and then using Polydimethylsiloxane (PDMS) to cast the channel. This method is widely used in the literature, but PDMS usually suffers from high loss tangent, which reduces the efficiency of antennas. In this section, we introduce another two methods of channel fabrication, namely: 1) cutting slots in the PCBs; and 2) 3D-printing channels. Both methods can provide good RF performance for antennas.

The first method, i.e., cutting slots in the PCBs, is convenient for the case that liquid metal channels have simple shapes such as rectangular slots or via holes. In this case, those channels can be simply obtained by cutting PCBs using a mechanical milling machine or laser cutting. Fig. 2. 27 shows the schematic. The advantage of this method is that PCBs as the material have good RF performance and low impact on the antenna.

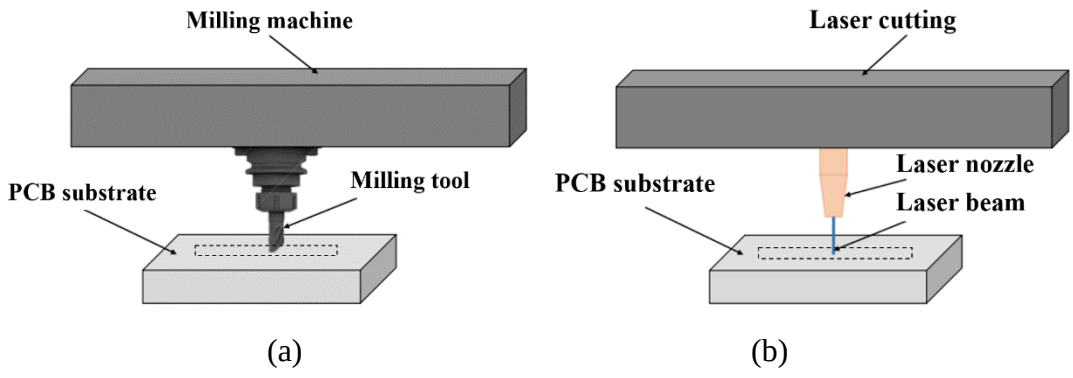

Fig. 2. 27. Schematic of (a) milling machine; and (b) laser cutting.

The second method, i.e., 3D-printing channels, is suitable for the channels with complex 3D shapes. For example, if the 3D channel design has a meander shape, 3D printers can easily print it with high quality. Fig. 2. 28 shows the schematic. The advantage of this method is that 3D printing technique can provide high accuracy, low cost, and fast processing for complex 3D channels.

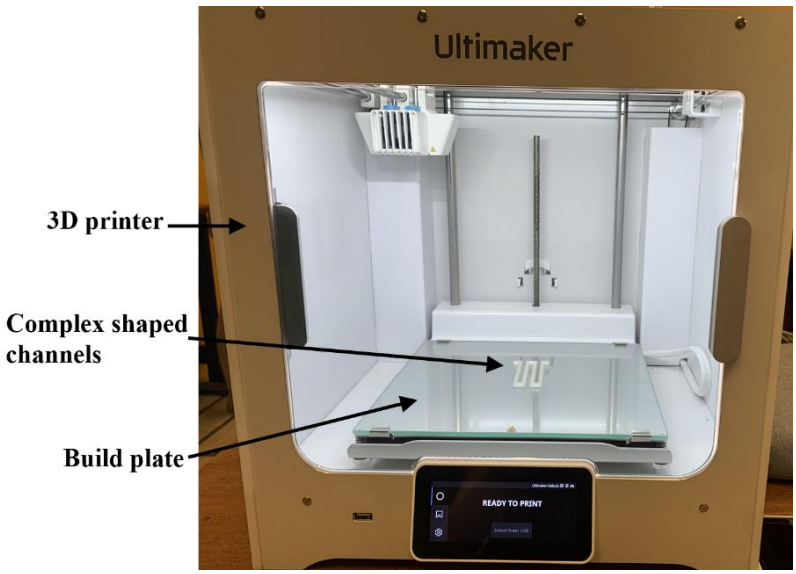

Fig. 2. 28. Schematic of 3D printing channel.

Let us now discuss how to assemble channels with an antenna. For the abovementioned two different fabrication methods of channels, we discuss the corresponding installation methods separately. Firstly, for the method of cutting slots in the PCBs, the channels could be bonded to an antenna by using the multilayer substrates bonding technique. Different bonding films are used according to different PCB substrates. For example, if the channel design uses the Rogers RO4003c as substrates, then the bonding film could be Rogers 4450F. This ensures the minimum interference with the electrical function of bonded strip line and other multilayer constructions. Secondly, for the method of 3D printing, channels could be simply assembled with an antenna by screws.

Throughout this thesis, different channel fabrication methods and installation methods are used depending on better suitability for each design. Further discussions will be

included in relevant sections throughout the thesis.

2.5 Beam Steerable Antennas Employing Liquid Metal

In the previous Sections 2.1 and 2.2, we discussed different beam steering techniques. Different initiators are applied in those techniques. Commonly, semiconductor devices, such as varactors, are widely employed in beam steerable antennas. For example, varactors loaded in parasitics realize beam steering by changing the antennas input impedance [95]. Many beam steerable antennas also incorporate switching devices, such as PIN diodes or MEMS, to alter the current paths [59] - [62]. Such switching initiators are employed in various structures, including switchable loads [96], switching the feed network [84], and switching parasitic elements [75]. Both varactors and PIN diodes are controlled by electrical techniques. They have advantages of fast response time and programmable features, which could be automatically controlled by computer programs. However, the significant power loss from these initiators will cause a low radiation efficiency. Liquid metal as the new material could be electrically controlled, and it still has the advantages of low insertion loss, low harmonic distortion, and large tuning ranges [97] - [99]. Thus, beam steerable antennas employing liquid metal play an emerging role in the next generation of wireless communications.

In this section, we will introduce the literature on beam steerable antennas employing liquid metal. We will introduce both the array antennas employing the liquid metal and the single antennas employing liquid metal.

2.5.1 Array Antennas Employing Liquid Metal to Achieve Beam Steering

In 2012, M. Li, et al, proposed a fluidically tunable periodic structure. It acts as a spatial phase shifter which can provide phase shifting range from 0° to 360° [100]. Fig. 2. 29

shows the proposed structure in [100]. It is a non-resonant transmit-array unit cell. The tuning mechanism is based on integrating small and movable liquid metal droplets within the unit cell. By moving these liquid metal droplets by small distances within the unit cell, the frequency response of antenna can be tuned continuously. However, in order to provide a 360º phase shifting range, the unit cell has several layers filled with liquid metal. Moreover, the droplets of liquid metal in each layer need to be precisely posited in right places, which is difficult to achieve it. Thus, it is desirable to propose a simple and practical unit cell which can provide large phase shifting range for array antennas.

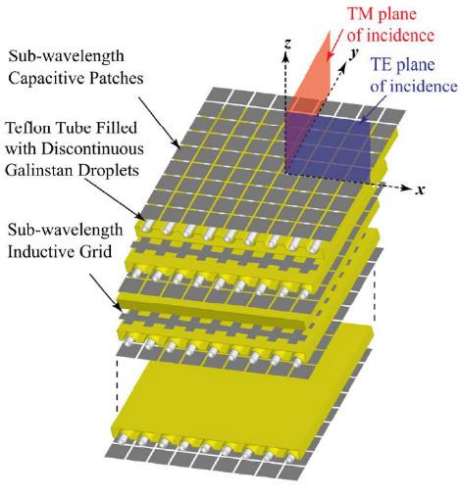

Fig. 2. 29. The topology of a fluidically tunable transmit-array unit cell proposed in [100].

Split Ring Resonator (SRR) is another structure commonly used within microwave circuits and antennas. Recently, it was demonstrated that an SRR tunable filter with liquid metal can be tuned by adjusting the size and position of the air gap within the structure [99]. Fig. 2. 30 shows the structure. In [101], the structure is easy to fabricate, and the size and position of the air gap can be tuned by applying pressure with a finger. However, the results presented in this paper only verify that the structure can provide the phase shift by changing the size and position of the air gap. It did not propose an alternative design which can provide a large phase shifting range for a transmit-array

antenna.

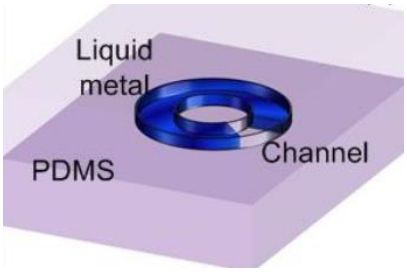

Fig. 2. 30. The structure of SRR unit cell proposed in [101].

[71] presented a continuously tunable microfluidic transmit-array unit cell. Fig. 2. 31 shows the proposed unit cell. It comprises double-layer split rings. The split rings are worked as microfluidic channels embedded in PDMS. Conductive regions of the rings are formed by injecting liquid metal, and there are air gaps within the rings. Phase shift is achieved by employing the unit cell rotation method, as shown in Fig. 2. 32. Specifically, under the incidence of a wave with circular polarization, the rotation of the transmit-array unit cell around the surface normally results in a phase shift of the transmitted wave which is equal to twice the angle of unit cell rotation. In this case, a 360° linear phase shifting range in the transmitted field is provided. However, such structure has two strict requirements for the incidence wave: 1) there should be 90° of phase difference between the orthogonal components of the transmitted wave; 2) the magnitudes of the orthogonal components at that frequency should be maximized.

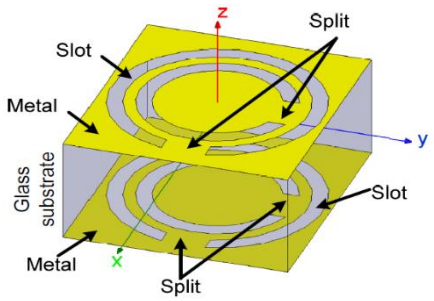

Fig. 2. 31. Dual-layer nested split ring slot structure proposed in [71].

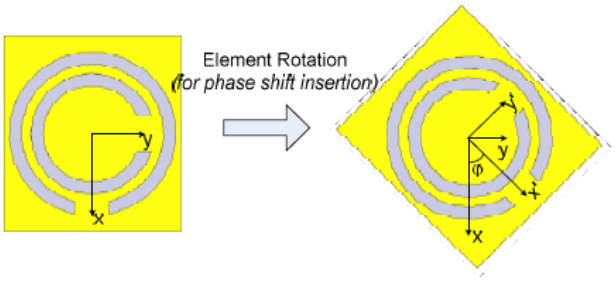

Fig. 2. 32. Unit cell rotation method for phase shift insertion in transmit-array unit cells proposed in [71].

2.5.2 Single Antennas Employing Liquid Metal to Achieve Beam Steering

[102] presented a beam steerable antenna based on the displacement of liquid metal. The antenna is based on a Yagi-Uda type antenna consisting of a central driven element and movable liquid metal parasitic. The liquid metal is located within a microfluidic channel which surrounds the central driven element. Fig. 2. 33 shows the structure. The driven element which is made out of solid copper has a static behavior. Beam steering is achieved by varying the position of the liquid metal parasitic. The antenna operates at 1800 MHz, and it can steer beams over a 360° range. However, in practice, it would be challenging to accurately control the position of the liquid metal and air gap within channels for this design.

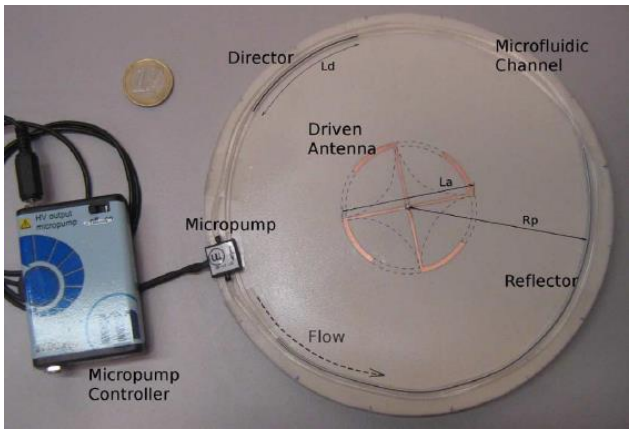

Fig. 2. 33. Structure of microfluidic reconfigurable antenna proposed in [102].

[103] presented a beam switchable cone antenna employing liquid metal reflectors. It

consists of a metal cone which acts as the main radiator and eight poles, surrounding the radiator. Fig. 2. 34 shows the structure. The poles are used as reflectors. The coaxial probe for feeding is directly connected to the bottom of the cone, which has an influence on the impedance matching of the antenna. Form Fig. 2. 34, it can be seen that eight poles are placed symmetrically in an azimuth plane with a 45° interval. The proposed antenna can switch its beams by controlling the director and the reflectors in the microfluidic channels. The tubes at different positions can be filled or emptied of liquid metal. When these tubes are injected with liquid metal as reflectors, the overall radiation of the cone antenna is deflected to the opposite direction of them to achieve beam steering. It operates from 1.7 GHz to 2.7 GHz and has four different operating modes. Syringes were used to inject liquid metal into the tubes. Injecting the liquid metal into the straight holes would be easier than the previous antenna in [71]. However, the proposed antenna has a relative high profile, which limits its application.

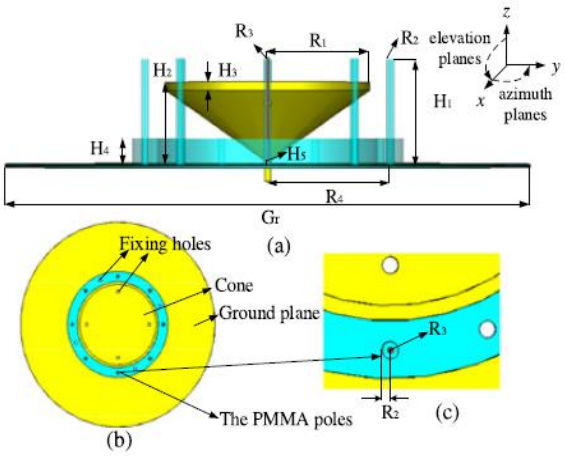

Fig. 2. 34. Structure of the proposed cone antenna proposed in [103].

[97] presented a planar beam switchable antenna using liquid metal. The antenna can switch the beam along both E- and H-plane. Instead of relying on phase shifters, the antenna employs parasitics. The parasitics are formed from liquid metal. Fig. 2. 35 shows the structure. The liquid metal located in the middle of the antenna is employed as the driven element. The location of parasitics can be altered, as they are also formed

from liquid metal. The parasitics can work as reflectors or directors, thus switching the beams in the E- and H-plane. This antenna achieves beam switching up to a minimum angle of ±48° in the H-plane, and ±54° in the E-plane. Fig. 2. 36 shows that a 2D beam switching could be achieved by combing different states of parasitics. The proposed beam switching mechanism is easy to realize and shows a potential capability for future beam steerable antennas. However, the beams are still discrete instead of continuous.

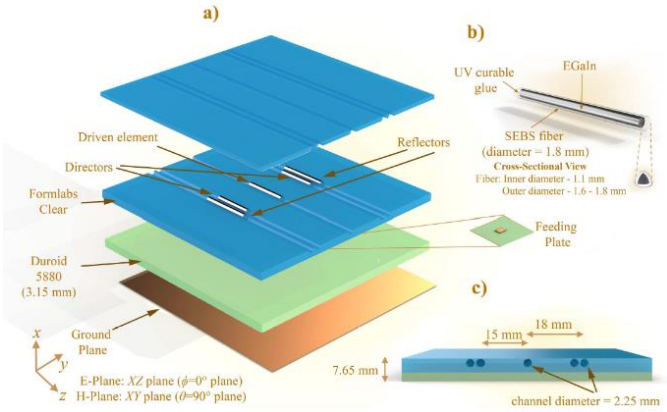

Fig. 2. 35. The structure of antenna proposed in [97].

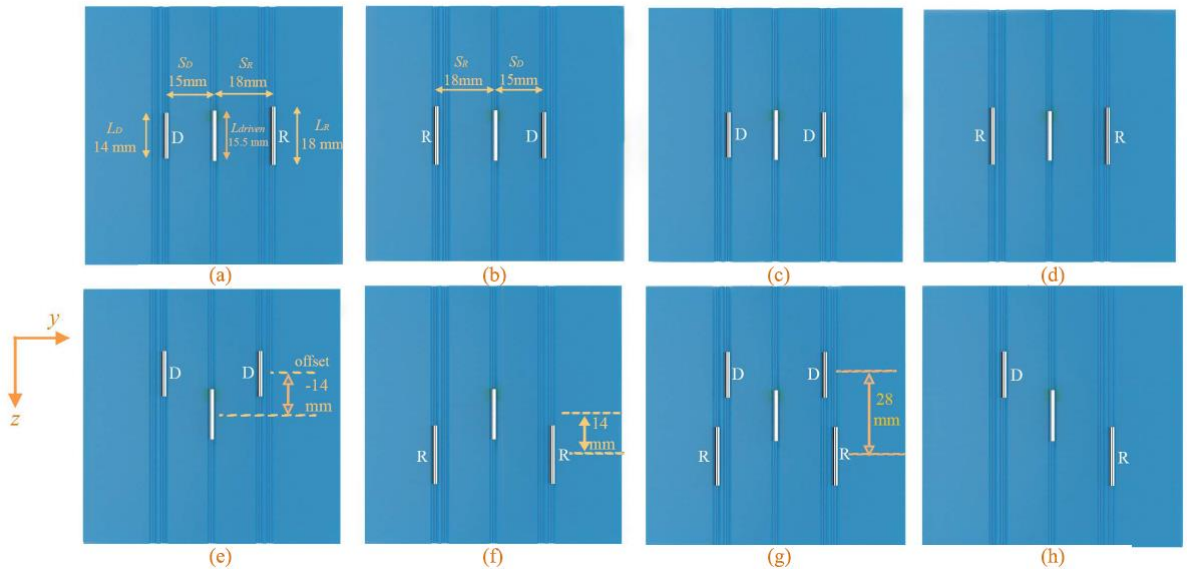

Fig. 2. 36. Examples for different states of parasitics proposed in [97].

This section reviewed a wide range of different techniques for beam steerable or switchable antennas, including array antennas and single-element antennas. Some relevant works were introduced, including their advantages and disadvantages. What

these different pieces of work have in common is that they all relate to beam steering or beam switching employing liquid metal.

2.6 Research Gap

The following lines of enquiry have been identified from the analysis above.

Firstly, it is important to figure out the performance limits of a structure before we start the design work. Transmit-array antennas play an important role in beam steerable antennas. Most of the existing works, on unit cells of transmit-array antennas, focus on the designs having a specific geometry. However, the transmission behavior of the structure is usually neglected in the literature. Consequently, to further design a beam steerable transmit-array antenna, it is important to explore the transmission behavior and the performance limits of the unit cells first.

Secondly, the radiation efficiency of reconfigurable transmit-array unit cell needs to be improved. Existing literature uses initiators having large insertion losses such as varactors. Only a few papers proposed some designs using new materials with low loss [100], but they have complex and costly multilayer structures. It appears that a reconfigurable transmit-array unit cell, having large phase shift, low insertion loss, and simple structure simultaneously, is not currently available.

Thirdly, a beam switchable patch antenna with good performance is needed. It is common that a single patch antenna could provide the beam reconfiguration. However, they have many disadvantages in their performance. For example, the switchable beam provided by those antennas are usually in unevenly steps, or those antennas have a narrow steering range or a large scan loss. To the date, there have been a few attempts for simple patch antennas providing switchable beams in even steps and covering a

wide steering range with low scan loss.

Fourth, the capability of continuous beam steering of single-element antennas needs to be improved. It is common for array antennas to provide the continuously steering beams. However, their configurations are complex and costly. Few literature achieves beam steering by single-element antennas. It appears that continuously steering beams provided by a simple-element antenna are desirable.

2.7 Chapter Summary

Beam steerable antennas are experiencing significant growth in modern cellular, satellite, and radar antenna systems. At the beginning of this chapter, different beam steering techniques employed in different types of antennas, including phased array antennas, reflect-array antennas, transmit-array antennas, lenses, and single-element antennas, were explored. Advantages and disadvantages of each technique have been discussed. Additionally, we gave a specific design as an example to further illustrate each beam steering technique. In the following section, we introduced the background information related to liquid metal alloy, 3D printing technique and channel fabrication processes. Based on these discussions, we know that liquid metal working as a promising initiator attracts an increasing attention of researchers due to the advantages of low insertion loss, low harmonic distortion, and large tuning ranges. In this case, using liquid metal within the antennas to achieve beam steering attracts more interests. Some literature that uses liquid metal to achieve beam steering was introduced as well.

Several research gaps have been identified which are not fully addressed by previous works. These research gaps include: the transmission behavior analysis of beam steerable transmit-array unit cells; improving radiation efficiency of reconfigurable transmit-array unit cell; a simple patch antenna having large steering range with low

scan loss; and a simple patch antenna with the capability of continuous beam steering. The following chapters present theoretical calculations and antenna designs which are intended to address these gaps.

Chapter 3 Theoretical Analysis of Transmission Properties of a Transmit-Array

As described in Chapter 2, transmit-array antennas are one of the most popular forms of beam steerable antenna. Different designs of transmit-array unit cells play an important role in deciding the radiation performance of an array. Previous literature focuses on specific designs of transmit-array unit cells to suit different requirements. The fundamental limits on the performance of a transmit-array unit cell are usually neglected in the literature. However, it is essential to understand the fundamental limits on the performance of transmit-array antennas before starting to design a specific structure.

This chapter presents a theoretical study that establishes the performance limits for a multi-layer transmit-array unit cell. This is the first study to be applicable to unit cells in which the conducting resonators, on the different layers, are shaped differently. The study enables one to account for the effects of dynamically reconfiguring the resonators on certain layers (e.g. through shape change). Firstly, the study quantifies the range of phase shift values, available from the unit cell, for a given amplitude of S_{21}. Secondly, for a given phase shifting range of S_{21}, a new methodology for analyzing the maximum S_{21} amplitude is also proposed. This methodology has been used to calculate the maximum S_{21} amplitudes for unit cells based on different substrates. Finally, the theoretical calculations have been validated through computer simulations. This study aims to give a theoretical introduction into the novel transmit-array unit cell design that will be presented in this chapter.

3.1 Introduction

Beam steering could be achieved by different kinds of array antennas, including phased array antennas, reflect-array antennas, and transmit-array antennas. Compared with the phased array antennas, reflect-array and transmit-array antennas are spatially illuminated by a single feed, which is simpler and more efficiency. Additionally, compared with a reflect-array antenna, a transmit-array antenna has advantage that the feed and its supporting structure do not block the antenna aperture. Thus, transmit-array antennas are widely applied in wireless communication systems to achieve beam steering.

Consider a transmit-array antenna, it consists of many passive unit cells. In order to create a collimated beam in a particular direction, the transmit-array antenna is necessary to compensate for phase changes caused by the spatial separation between the unit cells. To achieve this, the unit cell, of the transmit-array antenna, must be capable of supporting a 360° phase shifting range. In order to steer the beam produced by a transmit-array antenna, it is necessary to create a progressive phase shift across the unit cells comprising the antenna. If we wish to steer beams to wide angles and also to maintain high gain, then this imposes three important requirements on the unit cell of the transmit-array antenna: 1) it must be possible to vary the phase of transmission coefficient (i.e. $\angle S_{21}$) over a wide range; 2) the amplitude of transmission coefficient (S_{21}) must remain constant throughout the tuning range, otherwise the efficiency and hence gain of the antenna will be adversely effected; 3) there should be only a small fluctuation in the amplitude of S_{21} over the entire phase shifting range of the unit cell. From this discussion, it is clear that the phase shifting range that can be achieved within a unit cell of the transmit-array antenna along with the corresponding amplitude of S_{21} both play vitally important roles in determining the beam steering performance of a

transmit-array antenna. This motivates the study reported in this chapter. Henceforth, we refer simply to unit cells but it should be understood that we are referring to the unit cells of transmit-array antennas.

The unit cells within a transmit-array antenna are expected to provide a 360° phase shifting range, as mentioned earlier. However, it is difficult to achieve this goal using a unit cell comprising only one or two conducting layers [103]. For this reason, larger numbers of conducting layers, separated by dielectrics or air gaps, are commonly employed [105] - [107]. For example, [105] and [106] employ seven and five conducting layers, respectively, to cover a 360° phase shifting range. To provide the required phase shifting range and yet maintain an S_{21} amplitude $\leq$ -1 dB, the unit cells in [105] - [107] require at least four identical conducting layers. Although increasing the number of layers within the unit cell will normally expand the phase shifting range, one potential drawback of such an approach is the relatively high profile of the unit cell. Furthermore, increasing the number of layers will inevitably decrease the amplitude of S_{21}. In an effort to reduce the profile, [108] and [109] propose unit cell designs having only three conducting layers while still providing the required phase shifting range. However, [108] and [109] focus on the geometries of the unit cell designs, and do not discuss the limitations on the phase shifting range

Most of the published literature, on unit cells for transmit-array antennas, presents designs having a specific geometry that was optimized to provide either: 1) a large phase shifting range, 2) the maximum amplitude of S_{21}, or 3) a low profile. However, these parameters are actually interrelated. For this reason, optimizing one parameter will often have an adverse effect on the other parameters. For example, [105] presents a unit cell having a 360° phase shifting range. The unit cell comprises seven conducting layers and achieves a large phase shifting range at the expense of a higher profile. More

importantly, the performance limits of the transmit-array antenna unit cells are usually neglected in the literature. [103] presents an investigation into the phase shifting range of a multi-layer transmit-array antenna unit cell. However, the conclusion drawn in [103] is only valid for unit cells in which the resonators on each of the conducting layers have identical geometries. This chapter presents a more general study which, for the first time, applies to the unit cells in which the resonators on the various conducting layers have different geometries.

3.2 Theoretical Analysis of a Single-Layer Structure

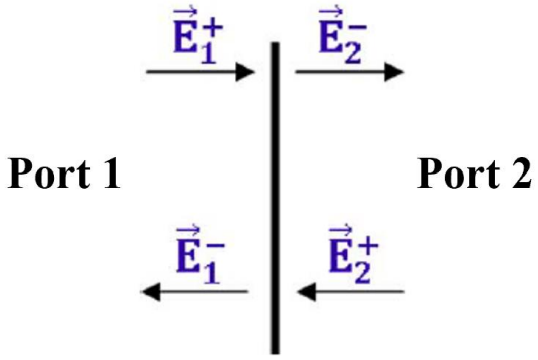

Fig. 3. 1. Single-layer structure.

For the purpose of theoretical calculation, a single conducting layer can be regarded as a two-port network [110], [110]. Fig. 3. 1 shows the schema. It is assumed to be illuminated on both sides. The incident and reflected plane waves are $\overrightarrow{E_1^+}$ and $\overrightarrow{E_1^-}$, respectively, for port 1. Similarly, $\overrightarrow{E_2^+}$ and $\overrightarrow{E_2^-}$ are the incident and reflected plane waves, respectively, for port 2. Thus, according to the linear two-port networks theory [111], these waves have the following relationship:

$$\begin{bmatrix} E_1^- \\ E_2^- \end{bmatrix} = \begin{bmatrix} S_{11} & S_{12} \\ S_{21} & S_{22} \end{bmatrix} \begin{bmatrix} E_1^+ \\ E_2^+ \end{bmatrix}$$

Where [S] is the scattering matrix of the two-port system. Three assumptions and approximations are applied to simplify the equations. They are as follows.

1) The layer is symmetrical and reciprocal, thus [S] matrix is symmetrical:

$$S_{11} = S_{22} \text{ and } S_{12} = S_{21} \tag{3.1}$$

2) The layer is lossless. Thus, we have,

$$|S_{11}|^2 + |S_{21}|^2 = 1, |S_{12}|^2 + |S_{22}|^2 = 1 \tag{3.2}$$

$$S_{11}{S_{12}}^* + S_{21}{S_{22}}^* = 0 \tag{3.3}$$

By submitting (3.1) in (3.3), we get

$$\angle S_{11} - \angle S_{21} = \pm\frac{\pi}{2} \tag{3.4}$$

3) Based on the Fresnel reflection and transmission coefficients, we get

$$S_{21} = 1 + S_{11} \tag{3.5}$$

By substituting (3.4) into (3.5), we can obtain an expression for the S_{21} amplitude as a function of the phase:

$$|\mathrm{S}_{21}|\mathrm{e}^{j(\angle \mathrm{S}_{21})} = 1 + |\mathrm{S}_{11}|\mathrm{e}^{j(\angle \mathrm{S}_{21} \pm \frac{\pi}{2})}$$
$$|\mathrm{S}_{21}| - |\mathrm{S}_{11}|\mathrm{e}^{\pm j\frac{\pi}{2}} = \mathrm{e}^{-j(\angle \mathrm{S}_{21})}$$
$$|\mathrm{S}_{21}| \mathrm{mj} |\mathrm{S}_{11}| = \cos(\angle \mathrm{S}_{21}) - \mathrm{jsin}(\angle \mathrm{S}_{21})$$

Thus,

$$|S_{21}| = cos(\angle S_{21}) \tag{3.6}$$

$$|S_{11}| = \pm sin(\angle S_{21}) \tag{3.7}$$

These equations show the relationships between the amplitude and phase of the transmission and reflection coefficients. From (3.6), it can be seen that the S_{21} amplitude, for a single conducting layer, is solely determined by the phase of S_{21} ($\angle S_{21}$), regardless of the size, geometry or orientation of the resonator on the conducting layer. In other words, the relationships hold irrespective of the unit cell shape. In Fig. 3. 2, equation (3.6) has been plotted on a polar diagram, such that the amplitude represents $|S_{21}|$ and the angle represents $\angle S_{21}$.

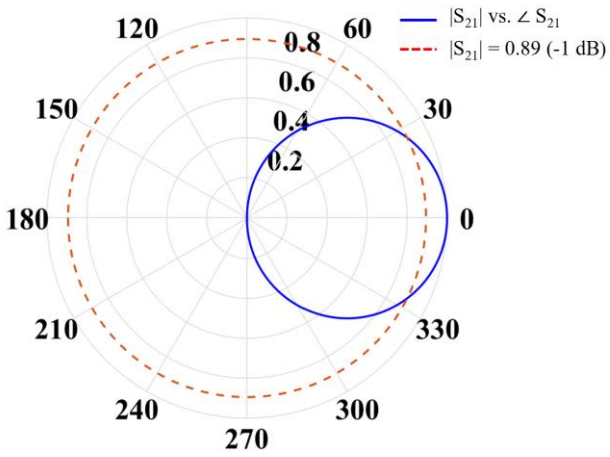

Fig. 3. 2. Transmission coefficient of a single-layer configuration.

From the above Fig. 3. 2, we know that the maximum transmission coefficient ($|S_{21}| = 1 = 0$ dB) is achieved only at multiples of 2π. In a practical scenario we may accept a certain reduction in the transmission coefficient. For example, in Fig. 3. 2, the curve pertaining to a -1 dB reduction of the transmission coefficient is marked by the red circle. The maximum phase range that could be achieved by a single layer transmit-array is 54º (±27º) for -1 dB transmission coefficient (i.e. an insertion loss of 1 dB).

Based on the above analysis, from (3.1), (3.4), (3.6), and (3.7), the S-parameters of a single layer configuration can be represented as a function of its transmission phase:

$$S_{11} = S_{22} = \sin(\angle S_{21}) e^{j(\angle S_{21} \pm \frac{\pi}{2})} \tag{3.8}$$

$$S_{12} = S_{21} = \cos(\angle S_{21}) e^{j(\angle S_{21})} \tag{3.9}$$

From (3.8) and (3.9), we can see that the [S] matrix is a function of only one variable, namely $\angle S_{21}$.

3.3 Theoretical Analysis of a Multi-Layer Structure

In this section, we will introduce the theoretical analysis of a multi-layer structure, including the double-conducting-layers structure and triple-conducting-layers structure. The following analysis is based on the above analysis of single-layer structure.

3.3.1 Double-Conducting-Layers Structure

Consider a unit cell incorporating two conducting layers. If these two conducting layers are identical in every way, the limit of the phase shifting range for a -1-dB amplitude of S_{21} is 170° [104]. In this section of Chapter 3, we generalize the analysis to conducting layers incorporating resonators that have different: sizes, geometries, orientations or perhaps all three. We discover that having the ability to vary those things does not increase the phase shifting range of a unit cell having two conducting layers.

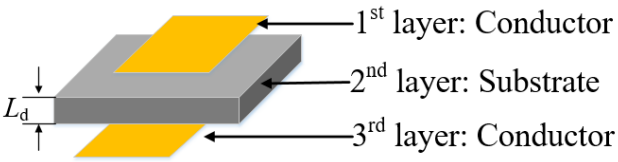

Fig. 3. 3. Schematic illustration of a unit cell incorporating two conducting layers.

Fig. 3 shows a unit cell for a transmit-array antenna incorporating two conducting layers. The two conducting layers are printed on the opposite sides of a single dielectric

substrate. By extension of the discussion in Section 3.2, each of the conducting layers can be modelled by a separate [S] matrix. If the resonators on the two conducting layers are identical in size, geometry, and orientation, then their [S] matrices will also be identical. If they differ in any of these three respects, then so will their [S] matrices. This study investigates a general case in which the [S] matrices on each layer differ.

Note that each conducting layer is represented by a separate [S] matrix. Each of the dielectric substrates is also represented by a separate [S] matrix. The matrices for each conducting layer are given by equations (3.8) and (3.9). Whereas the matrix for the dielectric substrate is given by equations (3.10) and (3.11).

$$S_{11} = S_{22} = \frac{\Gamma(1-e^{-j2\beta L_d})}{1-\Gamma^2 e^{-j2\beta L_d}} \tag{3.10}$$

$$S_{12} = S_{21} = \frac{(1-\Gamma^2)e^{-j\beta L_d}}{1-\Gamma^2 e^{-j2\beta L_d}} \tag{3.11}$$

$$\Gamma = \frac{1-\sqrt{\varepsilon_r}}{1+\sqrt{\varepsilon_r}},\ \beta = \frac{2\pi\sqrt{\varepsilon_r}}{\lambda_0} \tag{3.12}$$

Where: ε_r is the permittivity of the substrate, L_d is the physical thickness of the substrate, and λ_0 is the free-space wavelength. From equations (3.10), (3.11) and (3.12), it can be seen that the [S] matrix of a particular substrate is determined by the permittivity and thickness of the substrate material, as one would expect. However, these two factors have a similar influence on the [S] matrix. For brevity, we will only explore the effect of varying the substrate permittivity whilst keeping the substrate thickness constant. The overall [S] matrix, for a multi-layer unit cell, can be obtained by cascading the [S] matrices for the individual layers. Equations (3.13) to (3.15) result when two separate [S] matrices are cascaded together [110], [111].

$$S_{11}^{c} = \frac{S_{11}^{2} S_{12}^{1} S_{21}^{1}}{1 - S_{11}^{2} S_{22}^{1}} + S_{11}^{1} \tag{3.13}$$

$$S_{12}^{c} = S_{21}^{c} = \frac{S_{21}^{1} S_{21}^{2}}{1 - S_{11}^{2} S_{22}^{1}} \tag{3.14}$$

$$S_{22}^{c} = \frac{S_{22}^{1} S_{21}^{2} S_{12}^{2}}{1 - S_{11}^{2} S_{22}^{1}} + S_{22}^{2} \tag{3.15}$$

Where: S^1, S^2, S^c represent the first matrix, the second matrix and the overall cascaded matrix, respectively.

For a transmit-array antenna unit cell comprising two conducting layers, the overall [S] matrix can be determined by repeating the cascading process twice. Based on (3.14), the overall S_{21} is given as follows:

$$S_{21}^{3c} = \frac{S_{21}^{2c} \cdot S_{21}^{3}}{1 - S_{11}^{3} \cdot S_{22}^{2c}} \tag{3.16}$$

Where S^{2c}, S^{3c} represent the [S] matrices obtained by cascading two and three separate [S] matrices, respectively. S^3 represents the [S] matrix of the third layer of the unit cell. Note that, S_{21}^{2c}, S_{22}^{2c} are given by (3.14) and (3.15), respectively.

(3. 17) is obtained by substituting (3.2), (3.14), and (3.15) into (3.16).

$$\begin{aligned} S_{21}^{3c} &= \frac{S_{21}^{1} \cdot S_{21}^{2} \cdot S_{21}^{3}}{(1 - S_{11}^{2} \cdot S_{22}^{1}) \left[1 - S_{11}^{3} \cdot \left(\frac{S_{22}^{1} \cdot S_{21}^{2} \cdot S_{12}^{2}}{1 - S_{11}^{2} \cdot S_{22}^{1}} + S_{22}^{2}\right)\right]} \\ &= \frac{S_{21}^{1} \cdot S_{21}^{2} \cdot S_{21}^{3}}{1 - S_{11}^{1} \cdot S_{11}^{2} - S_{11}^{2} \cdot S_{11}^{3} - S_{11}^{1} \cdot S_{11}^{3} \cdot \left[(S_{21}^{2})^2 - (S_{11}^{2})^2\right]} \end{aligned} \tag{3.17}$$

In practice, once a substrate has been selected, its properties (and hence [S] matrix) are fixed. Consequently, for a given choice of substrate, the main factors in (3.17) that we can control are the [S] matrices of the two conducting layers. The [S] matrix of each

conducting layer is a function of only one variable (i.e. $\angle S_{21}$). However, the overall relationship, described by (17), is actually a function of two variables (i.e. $\angle S_{21}^{1}$, $\angle S_{21}^{3}$). Equation (3.17) can, therefore, simply be expressed as follows:

$$Am \cdot e^{jPhase} = S_{21}^{3c} = f(\angle S_{21}^{1}, \angle S_{21}^{3}) \tag{3.18}$$

For each set of $\angle S_{21}^{1}$ and $\angle S_{21}^{3}$ values, there is a corresponding complex value of S_{21}^{3c}. Fig. 3. 4 plots the S_{21}^{3c} amplitude and phase distributions as a function of these two variables ($\angle S_{21}^{1}, \angle S_{21}^{3}$). The different parts of Fig. 3. 4 pertain to different substrate permittivity values. The electrical thickness (βL_d) remains fixed. Fig. 3. 4 (a) and (b) show the overall S_{21} amplitude and phase distributions, respectively, when the permittivity is set to 3.38. Similarly, Fig. 3. 4 (c) and (d) show the separate S_{21} amplitude and phase distributions when the permittivity is set to 1. The phase of the overall S_{21} (i.e. $\angle S_{21}^{3c}$) remains constant at all points on the white dashed line, shown in Fig. 3. 4 (b). The corresponding amplitude of the overall S_{21} (i.e. $|S_{21}^{3c}|$) is indicated by the points on the white dashed line, shown in Fig. 3. 4 (a). It can be seen that amplitude assumes several different values. From the S_{21} amplitude distributions, shown in Fig. 3. 4 (a) and (c), it can be seen that the maximum amplitude for a given $\angle S_{21}$ value is obtained when the values of the two variables (namely $\angle S_{21}^{1}, \angle S_{21}^{3}$) are identical (as indicated by the diagonal dashed line in Fig. 3. 4 (a)). In other words, for a given $\angle S_{21}$, the maximum amplitude of the overall S_{21} is obtained when the separate [S] matrices associated with the different layers are identical to one another.

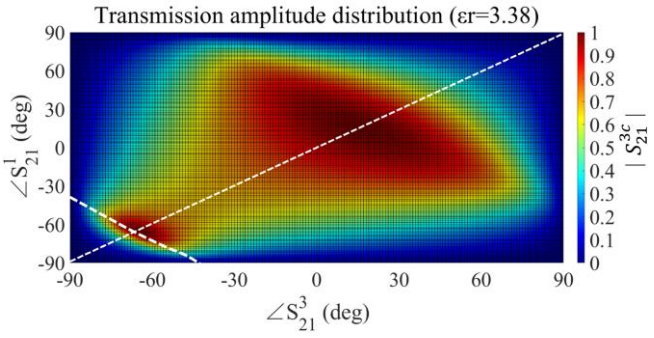

(a)

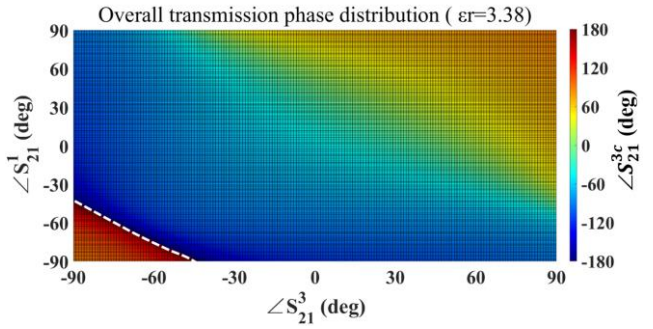

(b)

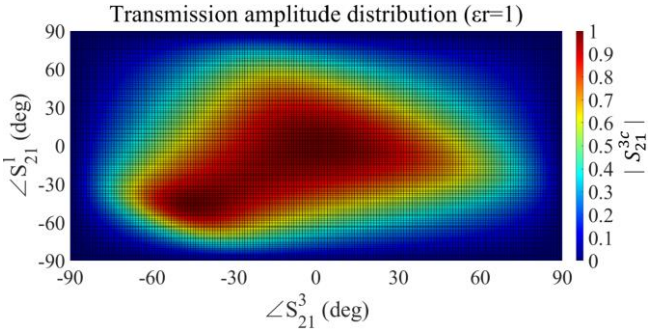

(c)

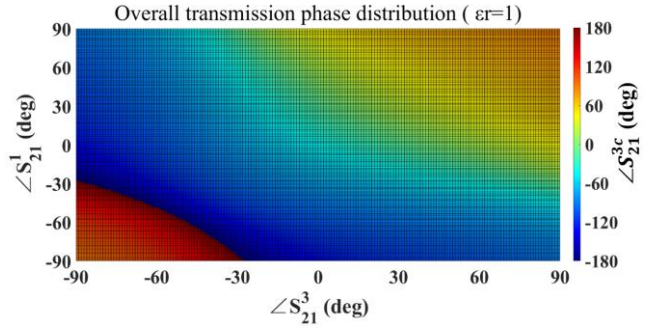

(d)

Fig. 3. 4. Amplitude and phase distributions as a function of two variables ($\angle S_{21}^1, \angle S_{21}^3$). (a) and (c) represent the amplitude distributions corresponding to substrate permittivities of 3.38 and 1, respectively. (b) and (d) represent the phase distributions corresponding to substrate permittivities of 3.38 and 1, respectively. The electrical thickness (βL_d) remains fixed at 45°.

Fig. 3. 5 plots the relationship between the S_{21} amplitude and phase in polar coordinates. The relationship shown in Fig. 3. 5 is for the general case in which the resonators on each conducting layer have different: sizes, geometries, orientations or perhaps all three. In Fig. 3. 5, the curves having a bold red outline represent the case that the resonators on the two conducting layers are identical in every way. From Fig. 3. 5, we can draw an interesting and valuable conclusion, namely that the S_{21} amplitude for the overall structure attains its optimal value when the geometry of the resonators on the two conducting layers are identical in every way. This conclusion agrees well with the conclusion obtained from Fig. 3. 4. This conclusion does not contradict our earlier statement about the limit of phase range. For a chosen permittivity of substrate, it illustrates the prerequisites for obtaining the maximum phase range. It is also reasonable that the phase shift ranges for 1-dB insertion loss shown in Fig. 3.5 are less than the earlier calculated limit.

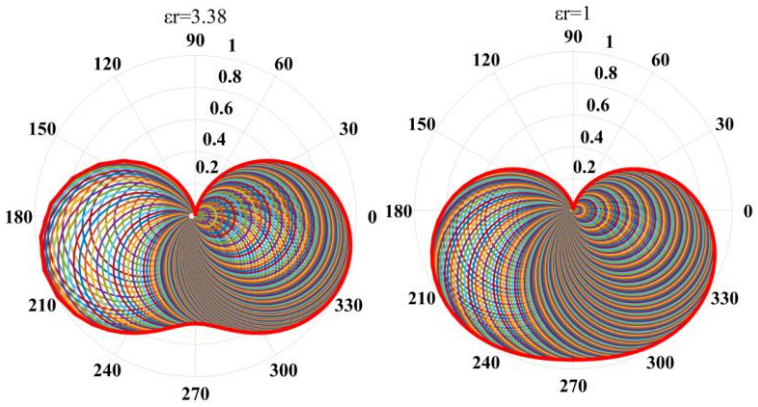

(a) (b)

Fig. 3. 5. Relationship of the S_{21} amplitude and phase ($\beta L_d = 45°$). (a) shows the relationship with the permittivity of 3.38. (b) shows the relationship with the permittivity of 1.

3.3.2 Triple-Conducting-Layers Structure

In the previous literature, pertaining to the unit cells for transmit-array antennas, it was assumed that the: size, geometry, and orientation of the resonators on different conducting layers were identical. Under this condition, at least four conducting layers

were required to provide a 360° phase shifting range with an S_{21} amplitude of -1 dB.

Based on the analysis presented in the above Section 3.3.1, it is clear that a unit cell having two conducting layers cannot achieve a phase shifting range of 360°. For that reason, we are forced to consider a unit cell having three conducting layers. In such a unit cell, the three conducting layers are separated by two substrates, as shown in Fig. 3. 6. To investigate this structure, we will first derive expressions for its overall S_{21}. To simplify the calculations, we assume that the permittivity and electrical thickness of the two dielectric substrates are identical and fixed. This implies that the [S] matrices of the two dielectric substrates are identical and remain constant. Thus, we use three variables, i.e. $\angle S_{21}^{1}$, $\angle S_{21}^{3}$, $\angle S_{21}^{5}$, to represent the [S] matrices of three conducting layers, respectively.

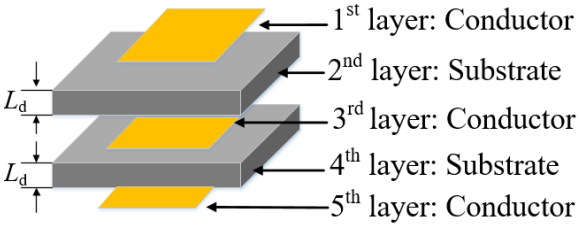

Fig. 3. 6. Schematic structure of a unit cell having three conducting layers.

The overall [S] matrix, for the unit cell having three conducting layers, is formed by cascading the [S] matrix of a unit cell having two conducting layers with that of the additional conducting layer and substrate. The overall S_{21} of the unit cell having three conducting layers can be expressed as a function of three variables using equation (3.19). Note that the form of (3.19) is similar to that of equation (3.18).

$$Am \cdot e^{jPhase} = S_{21}^{overall} = f(\angle S_{21}^{1}, \angle S_{21}^{3}, \angle S_{21}^{5}) \tag{3.19}$$

Fig. 3. 7 shows 3D plots illustrating the amplitude and phase distribution of S_{21} as

functions of three variables. Each plot shows three cuts through the 3D distribution. The different plots, shown in Fig. 3. 7, pertain to different dielectric substrate permittivity values but constant electrical thicknesses. Fig. 3. 7 (a) and (c) show the overall S_{21} amplitude distributions pertaining to dielectric substrate permittivity values of 3.38 and 1, respectively. Fig. 3. 7 (b) and (d) show the corresponding phase distributions of the overall structure. The phase (of S_{21}) shifting range is 360° with an S_{21} amplitude of -1 dB. This can be seen from the 2D cut-plane images in Fig. 3. 8. The white dotted line marks the extremity of the region in which the amplitude of S_{21} is better than -1 dB. Fig. 3. 8 shows the amplitude and phase distributions for the case where the first and third conducting layers have identical [S] matrices (i.e.$\angle S_{21}^{1} = \angle S_{21}^{3}$). The permittivity is 3.38 and the electrical thickness (βL_d) is 45°.

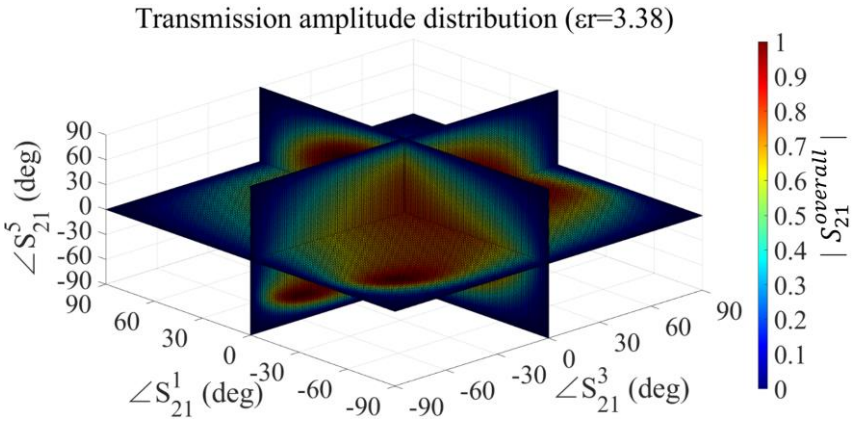

(a)

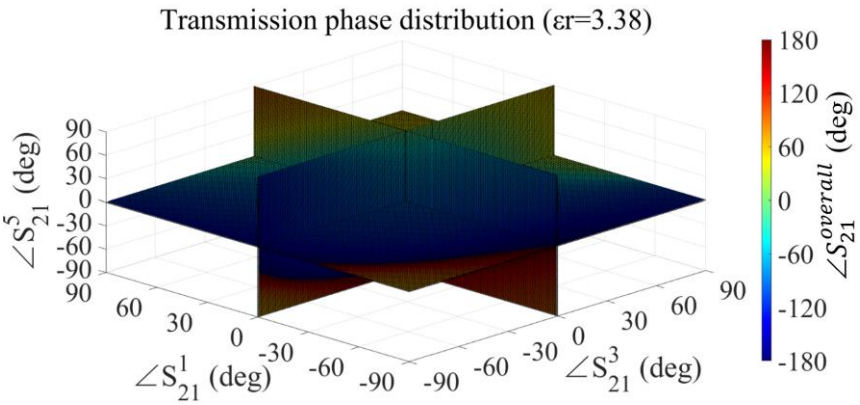

(b)

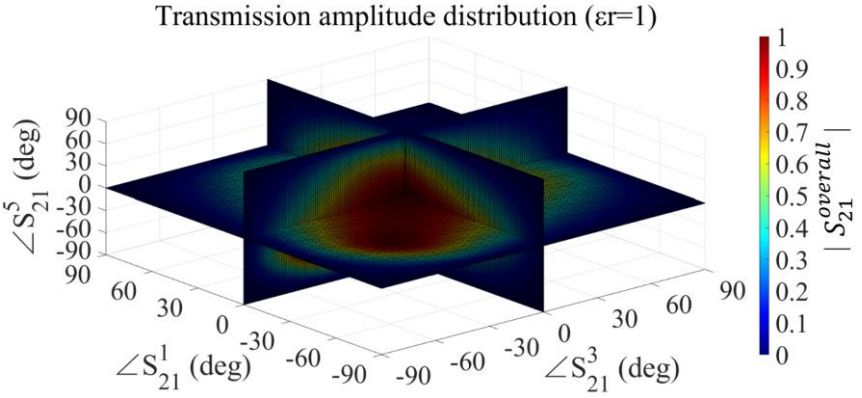

(c)

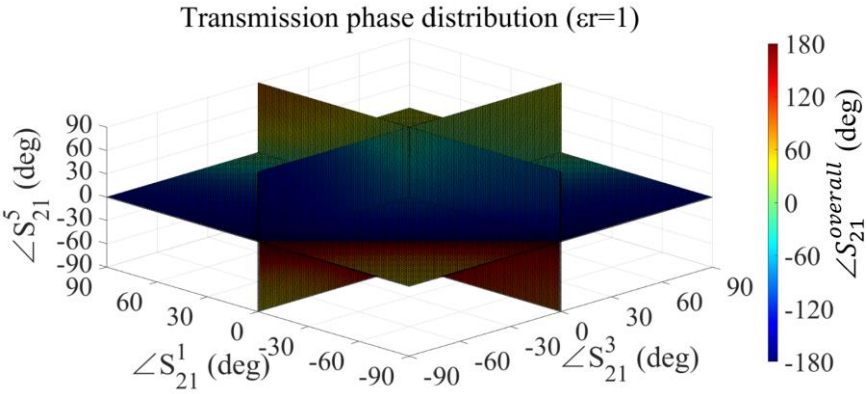

(d)

Fig. 3. 7. 3D views of the overall amplitude and phase distributions of S_{21} as a function of three variables. The different parts of the figure relate to different permittivity values but constant electrical thicknesses (βL_d) = 45°. (a) and (c) show the amplitude distributions, and (b) and (d) show the phase distributions.

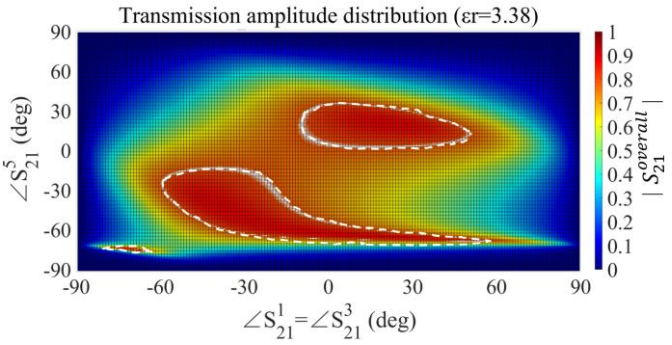

(a)

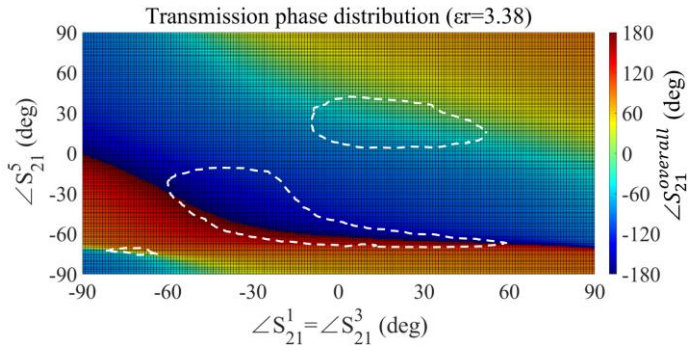

(b)

Fig. 3. 8. Amplitude and phase distributions on 2D cut plane ($\beta L_d = 45°$).

In this section, we show that the phase shifting range can be improved by employing resonators, on the different layers, which differ in their: size, geometry, orientation, or all three. Specifically, we discovered that a unit cell having three conducting layers can provide a 360° phase shifting range with an S_{21} amplitude of -1 dB. To achieve this, the resonators on the different layers must differ in their: geometry, size, and orientation or all three. We have also conducted further investigations for different substrate permittivity values and found that the phase shifting range, for most of the permittivity values considered (studied range: 1 to 10), can cover 360°.

3.4 Theoretical Calculation of the Transmission Amplitude Limitations

In this section, we fix the phase shifting range of the unit cells and evaluate the amplitude of S_{21} for a multi-layer unit cell as a function of the substrate parameters. We focus on a unit cell, for a transmit-array antenna, incorporating three conducting layers. In Section 3.3.2, we showed that such a configuration can yield a phase shifting range of 360°. We propose a new methodology for calculating the maximum S_{21} amplitude. Based on this newly proposed method, we calculate the S_{21} amplitude for different substrates.

Based on the analysis presented in Section 3.3.2, it is known that for a unit cell having three conducting layers and providing a 360° phase shifting range, the maximum S_{21} amplitude is determined by the permittivity and electrical thickness of the dielectric substrate. Consequently, for a unit cell based around a given dielectric substrate, the process of calculating the maximum S_{21} amplitude comprises three steps. The first step is to calculate the S_{21} of the overall cascaded structure and obtain a function of three variables similar to equation (3.12), as shown in Section 3.3.2. Secondly, we must find the maximum S_{21} amplitude pertaining to each phase shift value. Note that a given phase of S_{21} ($\angle S_{21}$) usually corresponds to several different amplitude values as can be seen in Fig. 3. 4, shown in Section 3.3.1. For this reason, the second step was achieved by applying a tree traversal algorithm, i.e. by searching and comparing all of the S_{21} amplitude values pertaining to a fixed value of $\angle S_{21}$. By repeating this process for a set of phase shift values, we obtained a corresponding set of amplitude values. Finally, the third step is to find the minimum value from the set of values obtained in step 2. The result is actually the maximum S_{21} amplitude over the considered phase shifting range. If the dielectric substrates were changed, then the calculation process, discussed above, would need to be repeated. Fig. 3. 9 gives a flowchart summarizing the whole calculation process.

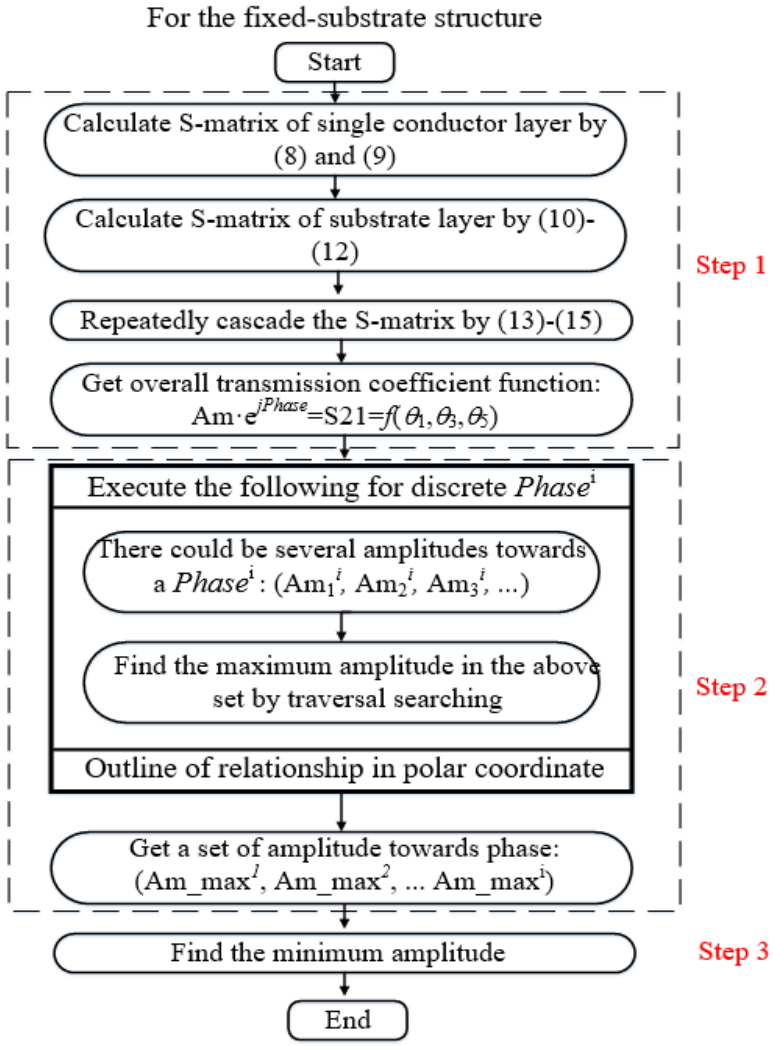

Fig. 3. 9. Flowchart of the calculation process.

Fig. 3. 10 presents the maximum S_{21} amplitude associated with a 360° phase shifting range for different dielectric substrates. From an analysis of Fig. 3.10, we can draw the following conclusions: 1) For a given value of substrate permittivity, a thick substrate will improve the S_{21} amplitude. This holds when the electrically thickness is less than 90°; 2) For a given value of substrate permittivity, the unit cell will exhibit minimum loss when the electrical thickness of the unit cell is quarter of a wavelength; 3) Two unit cells, having the same substrate permittivity and for which the sum of their electrical thicknesses is 180° (i.e. ε1= ε2 and ε1+ ε2=180°), will have the same S_{21}

amplitude limit; 4) For a given value of substrate electrical thickness, the limit on the S_{21} amplitude of the unit cell drops sharply as the permittivity increases.

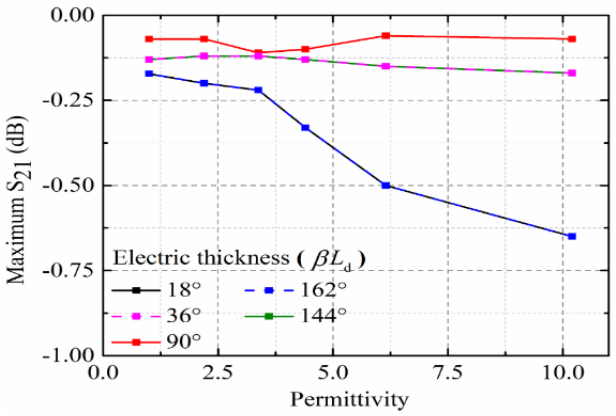

Fig. 3. 10. The maximum S_{21} amplitude values as a function of the permittivity of the dielectric substrate.

3.5 Simulation Results

This section presents the results of a study performed within the computer simulation environment. The purpose of the study was to validate the phase shifting range of the multi-layer unit cells, presented in Sections 3.2 and 3.3. These unit cells were simulated at 2.5 GHz. All the computer simulation results, reported in this chapter, were obtained using CST Microwave Studio 2019.

3.5.1 Simulation of A Unit Cell Having Single Conducting Layer

Fig. 3. 11 shows the structure of a unit cell that was designed for the purpose of validating the results presented in Section 3.2. For convenience, we will refer to this as Design #1. Design #1 consists of a single conducting layer incorporating double square loops. These double square loops can provide a pair of resonances. By varying the dimensions of the square loops within the unit cell, the resonances can be moved. Design #1 operates at a central frequency of 2.5 GHz, and the periodicity of the unit

cell is $0.5\lambda_{0,}$ where: λ_0 is the free-space wavelength (P = 60 mm). We set the length of the outside of the loop L_1 as a variable for parametric study. It varies from L_1=23.5 mm to L_1=58.8 mm. The length of the inner of the loop L_2 changes with the change of L_1, such that the separation between the two loops is constant (S=8.4 mm). The widths w_1 and w_2 are equal to 1.7 mm.

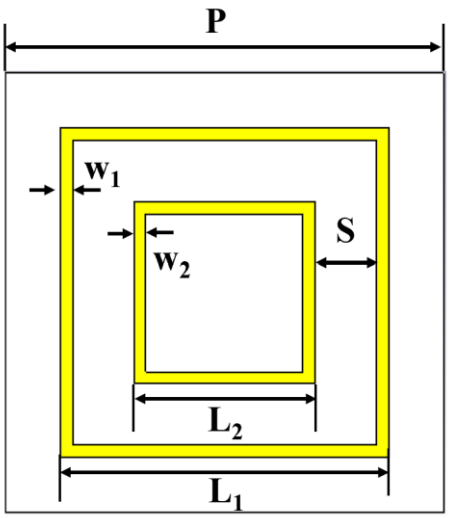

Fig. 3. 11. Geometry and dimensions of Design #1.

Fig. 3. 12 shows how the transmission coefficient changes as the length of the outside of the loop L_1 is varied. As can be seen, the design has the two resonant points at L_1=36 mm and L_1=57 mm. Fig. 3. 13 shows the relationship between the transmission amplitude and phase in a polar diagram. We compare the results obtained through calculation against those obtained through computer simulation in CST Microwave Studio. The blue solid circle represents the theoretically calculated behavior of single conducting layer, which was introduced in previous Section 3.2. The red solid circle depicts the computer simulation behavior of the single-conducting layer. From Fig. 3. 13, it can be seen that the simulation results agree well with the theoretical calculations. No matter how we change the length of the outside of the loop, the relationship between transmission amplitude and phase always coincides with the theoretical calculations in

the polar diagram. Thus, the calculated relationship between the transmission amplitude and phase of a single-conducting layer is verified by computer simulations.

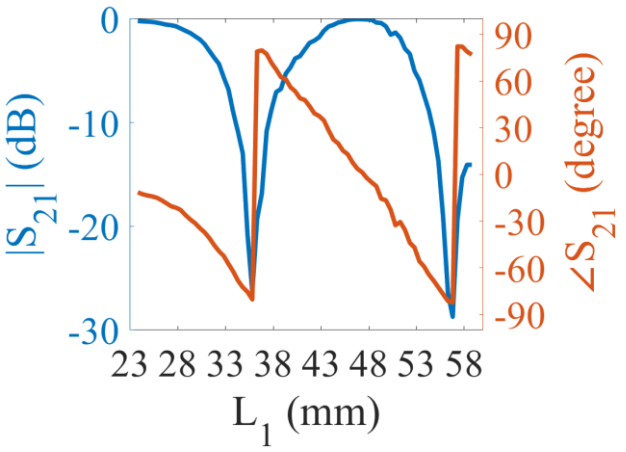

Fig. 3. 12. Transmission coefficient of the single-conducting layer versus the outer side loop length.

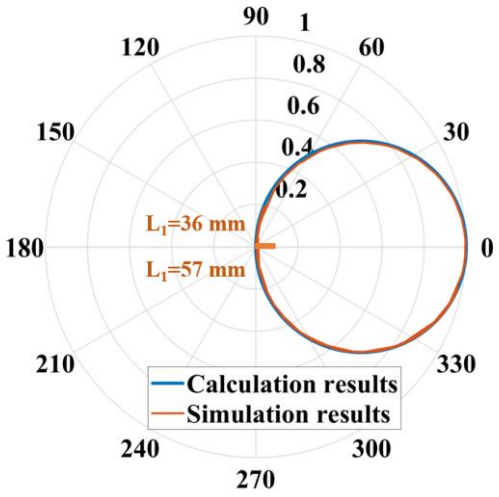

Fig. 3. 13. Comparison of the relationship between the transmission amplitude and phase in a polar diagram.

3.5.2 Simulation of A Unit Cell Having Two Conducting Layers

Fig. 3. 14 shows the structure of a unit cell that was designed for the purpose of validating the results presented in Section 3.3.1. For convenience, we will refer to this as Design #2. Design #2 incorporates two conducting layers that are located on the

opposite sides of a dielectric substrate. The resonators on each of the conducting layers are shaped in the form of a split-ring. The parameters of the resonator are as follows: R = 14.5 mm, w = 2 mm. The design operates at a central frequency of 2.5 GHz, and the periodicity of the unit cell is $0.32\lambda_0$, where: λ_0 is the free-space wavelength (P = 38.4 mm). The substrate has an electrical thickness (βL_d) βL_d of 45°. The electrical thickness of the substrate was not varied during the study. θ_1 and θ_2 represent the angles within the split ring resonators on the uppermost and lowermost conducting layers, respectively. By separately tuning the angles of these gaps within the allowed range (i.e. θ_1: 5° to 235°; θ_2: 5° to 235°), the [S] matrix of each conducting layer may be varied independently. We compare the results obtained through calculation against those obtained through computer simulation in CST Microwave Studio.

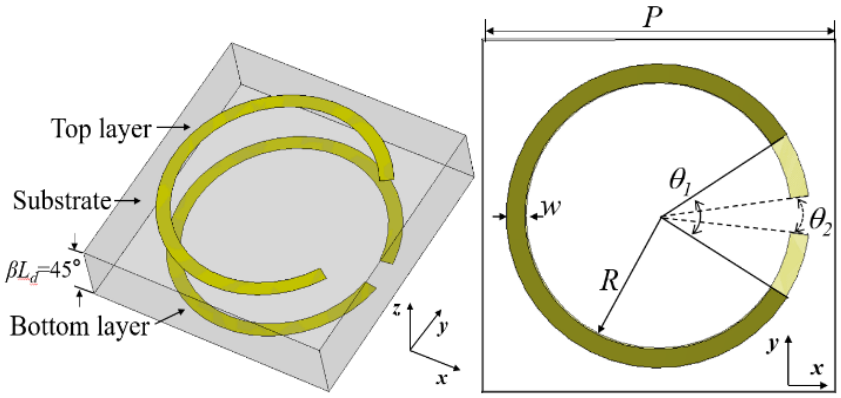

(a) (b)

Fig. 3. 14. Geometry and dimensions of Design #2. (a) Perspective view; (b) Top view. The uppermost layer of metal is shown in dark yellow, and the lowermost layer of metal is shown in light yellow.

Fig. 3. 15 shows the relationship between the overall amplitude and phase of S_{21} ($\angle S_{21}$) for different permittivity values. The red dotted curves represent the behavior of unit cells in which the geometries of the resonators on both conducting layers are varied in sympathy with one another. The green curves depict the behavior of unit cells in which the geometries of the resonators on both conducting layers are varied independently.

From Fig. 3. 15, it can be seen that the simulation results agree well with the theoretical calculations. The best amplitude performance, for a unit cell incorporating two conducting layers, corresponds to the situation in which the resonators, on the different layers, are identical in: geometry, size, and orientation, as expected. Agreement between simulation and theoretical results is better when the substrate permittivity is low as shown in Fig. 3. 15 (b). At some points in Fig. 3. 15 (a), there is a small deviation between the simulation results and those predicted by theory. This deviation can be attributed to the higher-order mode coupling between layers which is accounted for within the simulations but not modelled by the theoretical analysis.

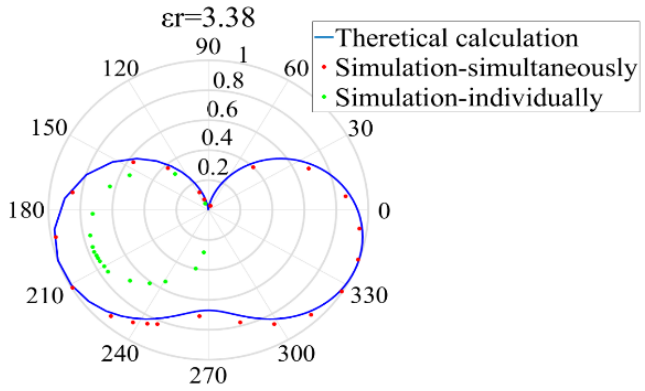

(a)

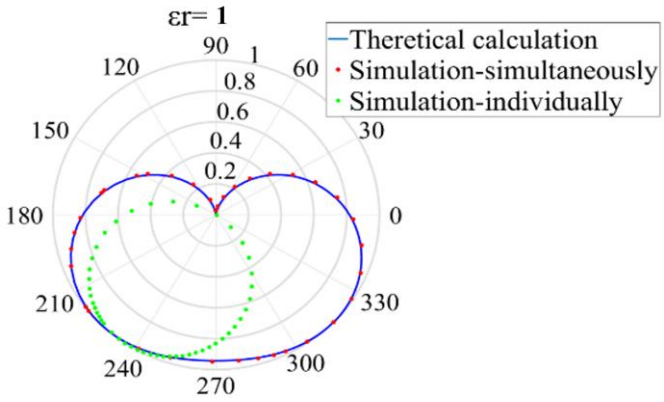

(b)

Fig. 3. 15. The relationship between the S_{21} amplitude and phase for Design #1. Permittivity is a parameter. ($\beta L_d = 45°$)

.

3.5.3 Simulation of A Unit Cell Having Three Conducting Layers

Fig. 3. 16 shows the structure of a unit cell that was designed for the purpose of validating the results presented in Section 3.3.2. For convenience, we will refer to this as Design #3. Design #3 incorporates three conducting layers and 2 dielectric substrates. Design #3 incorporates different resonator geometries on each of the three conducting layers. An arrow-shaped conductor, as illustrated by the solid line in Fig. 3.16 (b), is orientated diagonally and located on the middle layer. It has the capability to convert the polarization of a propagating wave. The split ring resonators, located on the uppermost and lowermost conducting layers, have the same size, as one another, but different orientations. Specifically, the incident wave along +Z-axis with X-axis polarization excites the unit cell. Due to the action of the arrow-shaped resonator, the output wave is polarized along the Y-axis. The length of the arrowhead (L) is varied from 10 mm to 29 mm in order to vary the phase shift through the structure.

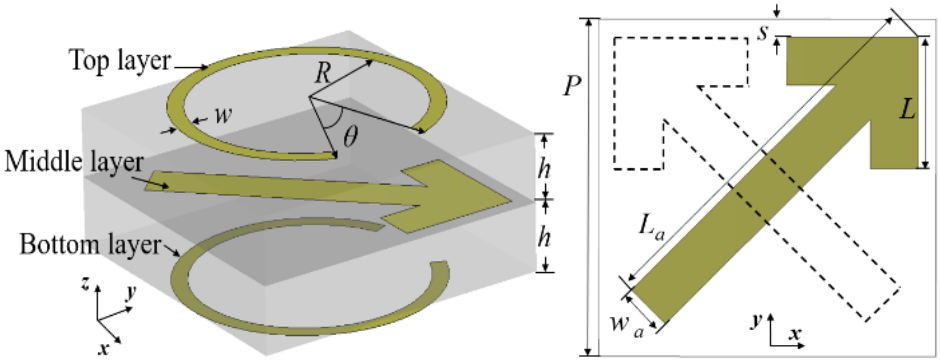

(a) (b)

Fig. 3. 16. Geometry and dimensions of Design #2. (a) Perspective view. (b) Top view of the middle layer and its mirrored image shown by the dashed outline. P = 38.4, R = 13.5, w = 2, θ = 15°, h = 7.6, s = 2, w_a = 5.5, L_a = 38.4. All dimensions are in mm. The dielectric substrates have a relative dielectric constant of 3.38.

Fig. 3. 17 presents the simulation results for the S_{21} amplitude and phase versus frequency. From Fig. 3. 17, we can see that for an S_{21} amplitude of -1 dB, a ~230° phase shifting range is achieved at 2.5 GHz. An additional 180° phase shift is obtained by

simply mirroring the arrow-shaped resonator about the Y-axis. The resulting structure is shown by the dash outline, in Fig. 3. 16 (b). The total phase shift for the resulting unit cell is then over 360°. For that reason, the proposed unit cell validates the theoretical calculations. Note that for a phase shifting range of 360°, the maximum S_{21} amplitude of the proposed unit cell is actually -0.7 dB (*L*: 18 mm to 28 mm) which, as expected, is worse than the theoretical amplitude limit calculated in Section 3.4.

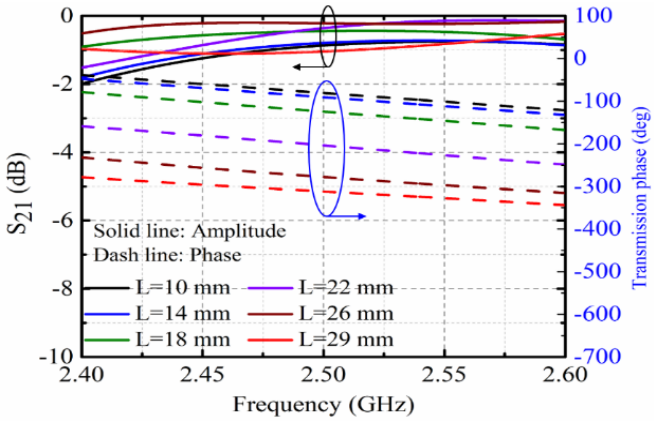

Fig. 3. 17. S_{21} amplitude and phase versus frequency of some representative parameters.

3.6 Chapter Summary

This chapter presents theoretical calculations which yield the transmission performance limits for multi-layer transmit-array antenna unit cells. To the best of our knowledge, this paper is the first to analyze the performance limits of unit cells incorporating resonators that have different: sizes, geometries, orientations or perhaps all three on the different layers. Based on the proposed analysis, for an S_{21} amplitude of -1 dB, the phase shifting ranges of unit cells having two conducting layers and three conducting layers are 170° and 360°, respectively. These phase shift values are achieved when the geometries of the resonators on the different layers are varied in sympathy and independently, respectively. Additionally, we also propose a new method for calculating the maximum S_{21} amplitude for a 360° phase shifting range. The calculation

was performed as a function of the thickness and permittivity of the dielectric substrate. For the first time, the paper explains why a dielectric substrate having a higher permittivity usually leads to a worse S_{21} amplitude. The paper shows that the optimum electrical thickness, for a unit cell, is a quarter-of-a-wavelength. These conclusions are validated through computer simulations. The proposed methodologies are valuable to guide future transmit-array unit cell designs.

Chapter 4 A Reconfigurable Transmit-Array Unit Cell Employing Liquid Metal

Building on the theoretical study presented in Chapter 3, in this chapter we design a reconfigurable transmit-array unit cell. It has a low profile with only three conducting layers. Compared with other reconfigurable unit cells, it also has lower insertion loss. Firstly, we give the design process for the unit cell, then we show the unit cell configuration and simulation results. Next, we describe the approach used to fabricate a hardware prototype and measure its performance. The proposed unit cell was fabricated and measured within an open-ended waveguide. The measured results agree well with the simulations and verify that we can model the unit cell correctly within the simulation environment. It is the first time that a transmit-array unit cell, reconfigured using liquid metal, provides this combination of low insertion loss and large phase shifting range.

4.1 Introduction

Transmit-array antennas are attracting increasing research attention due to their advantages, including: low profile, high gain, and beam steering capabilities. They convert the spherical phase front, available from the feed, into a planar plane pointing towards a specific direction. This is achieved by compensating a progressive phase shift between unit cells forming the transmit-array antenna. Dynamic reconfiguration of the transmission phase of each unit cell enables beam steering. Commonly, the following devices are used to reconfigure the phase of a transmit-array unit cell: 1) varactor diodes [65], [68]; 2) PIN diodes [57], [113]; or 3) microelectromechanical system (MEMS) switches [114]. These devices have the advantages of fast response time and programmable features, which could be automatically controlled by a computer

program. However, PIN diodes exhibit intermodulation distortion and significant power loss which will reduce the radiation efficiency. Compared to the existing devices for reconfiguring the phase, fluidic material is a promising approach which yields lower power losses and is expected to allow greater power handing capability together with enhanced tuning range. In particular, liquid metal, based on gallium alloys, has attracted more attention recently due to the above advantages together with its low toxicity, high conductivity, and good flexibility. Several antenna designs employing liquid metal have recently been published, including: a tunable monopole antenna [115], a slot antenna [116], and a helical antenna [117]. However, only a few designs employing liquid metal have successfully achieved reconfigurable phase shift. For example, [100] presents a fluidically reconfigurable transmit-array unit cell based on a fifth-order bandpass structure. By moving droplets of liquid metal through a small distance, the frequency response, and thus the transmission phase of the unit cell, can be continuously tuned. In this way, a 360° phase shifting range can be achieved with 1 dB of insertion loss. Their work demonstrates the potential for employing liquid metal in transmit-array unit cells. However, the fifth-order bandpass response consisting of nine metal layers and eight dielectric substrates increases the difficulties involved in fabrication and the actuation (or movement) of liquid metal.

This chapter presents a reconfigurable transmit-array unit cell employing liquid metal. The unit cell has a low profile together with only three conducting layers. By actuating the liquid metal into/out of the channels, the conductive regions can be reconfigured. As a result, the transmission phase of the unit cell can be tuned. Using this approach, a transmit-array unit cell operating at 3.3 GHz has been designed. It provides more than 300° of linear phase shifting range with an insertion loss of ~1.5 dB. Compared to conventional reconfigurable transmit-array unit cells using varactors or switches, the proposed unit cell provides a good improvement on the insertion loss. We fabricate a

hardware prototype and measure its performance using open-ended waveguide method. The measured results agree well with simulated results and verify that we can model the unit cell correctly within the simulation environment.

4.2 Unit Cell Design and Simulation Results

In this section, we firstly introduce the design process for the unit cell. We discuss several designs, from the literature, that provided inspiration for the proposed unit cell design. Then we show the configuration of the proposed unit cell along with the simulated results. All of the simulated results presented in this section were obtained using CST Microwave Studio 2019.

4.2.1 Design Process

Split Ring Resonator (SRR) is commonly used within microwave circuits and antennas. Recently, it was demonstrated that an SRR tunable filter incorporating liquid metal can be tuned by adjusting the size and position of the air gap within the section of liquid metal [101]. This paper was discussed in Section 2.4. It inspires us to employ a split-ring resonator within our transmit-array unit cell to achieve a phase shift by changing the size of the gap. Based on the theoretical study, presented in Chapter 3, we know that the simple structure proposed in [101] cannot provide the phase shifting range required by a transmit-array antenna. However, we use a SRR as our starting point.

Let us begin by discussing the principle by which an SRR can provide a phase shift. A single SRR (see Fig. 4. 1) can be modelled using a lumped element LC circuit.

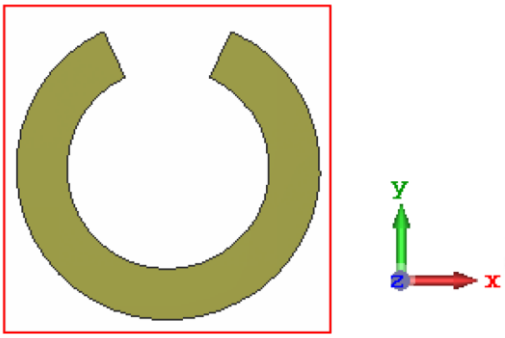

Fig. 4. 1. The configuration of an SRR structure.

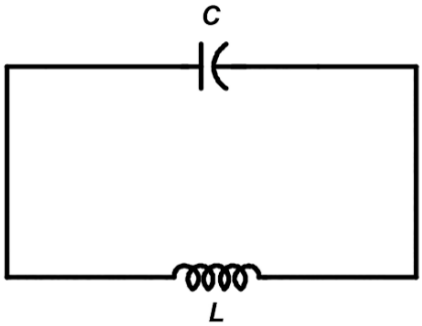

Fig. 4. 2. Equivalent circuit of a single SRR structure.

Fig. 4. 2 shows the equivalent LC circuit. The resonant frequency (ω_0) of the SRR is given by [118]:

$$\omega_0 = \sqrt{\frac{1}{LC}} \tag{4.1}$$

where the capacitance (C) is associated with the gap and the inductance (L) is related to the conducting track. The values of capacitance and inductance can thus be determined from the geometrical parameters. For example, if we change the size of the gap, the capacitance will be changed. Generally, a small gap corresponds to a high capacitance, thus resulting in a low resonant frequency. The shift of resonant frequency results in a phase shift at a single frequency. This explains the reason why it is possible to achieve phase shift by using the SRR structure.

Next, inspired by [118], we build and simulate an SRR unit cell with two conducting layers. The unit cell is shown in Fig. 4. 3. The phase shift, provided by the SRR, can be altered by varying the geometric parameters of the SRR. The two conducting layers have the same geometric parameters, while the SRR on the lower metal layer is rotated by 90° relative to that on the upper metal layer. The relative permittivity of the substrate is 4.3. By changing the size of the gaps (g) and the outer radius R_1, the phase shift can be changed, while the other parameters are constant. The initial fixed parameters of our design are as follows: P = 8.72 mm, t = 1.6 mm, R_1 = 4.3 mm, R_2 = 3.15 mm, g = 1 mm.

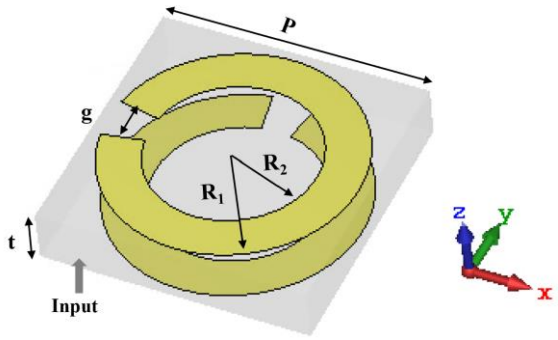

Fig. 4. 3. An SRR unit cell with two conducting layers.

It can be assumed that a normally incident x-polarization electromagnetic waves travels along the +z-direction onto the polarization converter. Specifically, the incident wave along +Z-axis is polarized along the X-axis. This wave excites the unit cell. Due to the function of the polarization converter, the output wave is converted into a wave that is polarized along the Y-axis. The sides of x and y are set as periodic boundary conditions and the z direction is set to open boundary conditions (open space). The simulated results are shown in Fig. 4. 4.

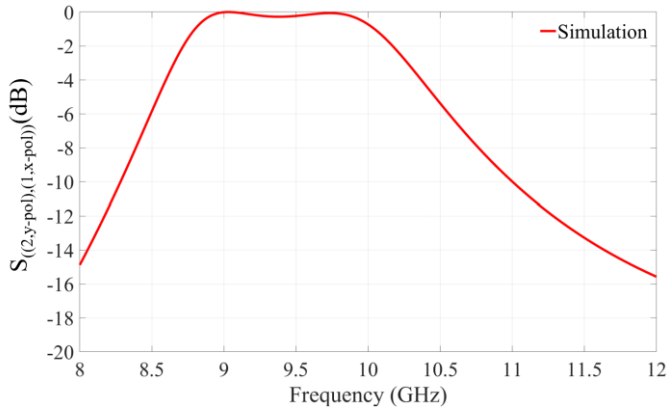

(a)

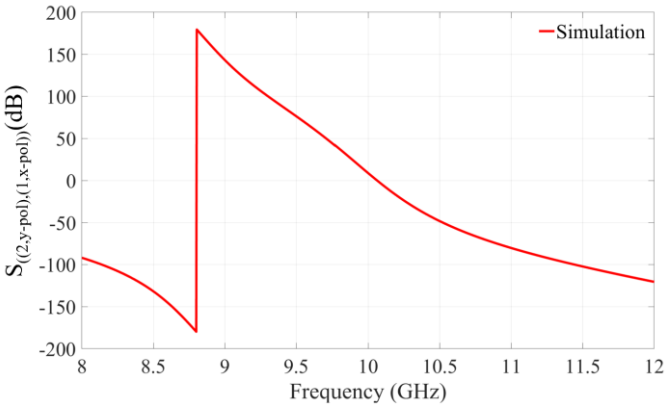

(b)

Fig. 4. 4. Transmission coefficients and phase shift figures of SRR unit cell. (a) transmission coefficients (S_{21}); (b) Phase shift of S_{21}.

When we tune the size of gap (i.e. *g* in Fig. 4. 3), the resonator frequency would change, leading to a change in the phase shift provided by the unit cell. As shown in Fig. 4. 5, by adjusting the size of gap from 1 mm to 2.2 mm, the SRR unit cell can achieve the phase shifting range from 8° to 143° at 10 GHz. It is worth noting that a high transmission coefficient (<-1dB) is kept when we tune the parameters of the unit cell, which is shown in Fig. 4. 5 (a). Fig. 4. 5 indicates that the SRR unit cell with double conducting layers is not enough to provide the desired phase shifting range., thus it is necessary to add some other resonators to improve the performance.

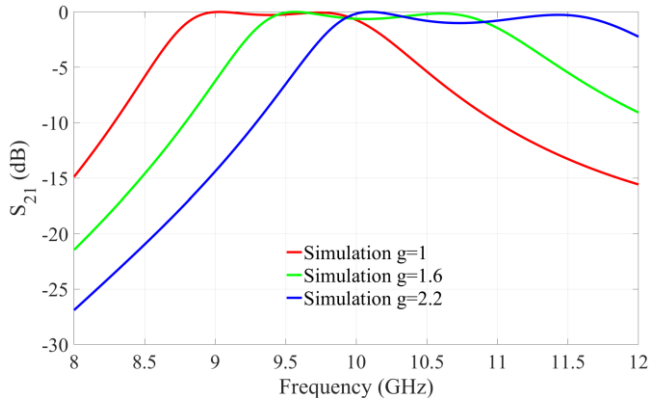

(a)

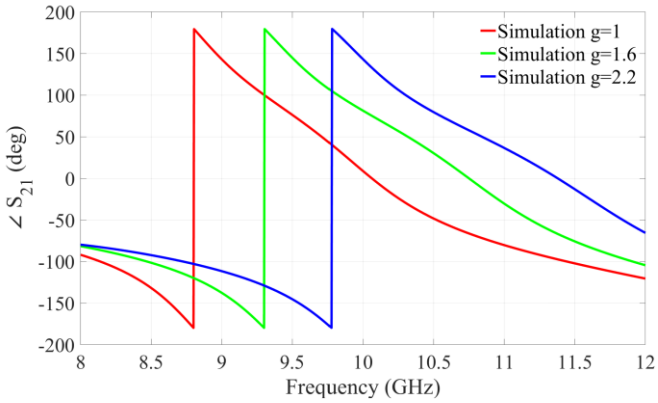

(b)

Fig. 4. 5. Transmission behaviors of SRR unit cell. (a) Transmission coefficients (S_{21}) and (b) the phase shift figures versus the different size of gap.

Recently, H. Yi, et al, published an arrow shaped structure in [120], which efficiently converts the linear polarization wave into another vertical linear polarization wave. The structure in the paper operates at a frequency in the Terahertz range.

Inspired by [120], we simulated a similar arrow-shaped structure which operates at a frequency of 60 GHz to check its phase shift capability. Fig. 4. 6 shows the structure. As observed, the arrow-shaped resonator is placed in the middle layer, with its symmetrical axis along the diagonal of the unit cell. It serves as the phase-shift component with arm length *L*, width *W*, and shaft length *La*. By changing *L*, the unit cell can control the transmission phase of the unit cell. On the upper and bottom layers, two metallic uniform grid polarizers with a width w_1 and a gap w_2 are orthogonally

arranged. After numerous simulations of the structure, the unit cell has a good matching and transmission coefficient at around 60 GHz. The relative permittivity of the substrates is 2.2, and the height of each layer is h=0.5 mm. Other parameters were fixed to the following values: T=1.6 mm, w_1=0.2mm, w_2=0.2mm, La=1.6mm, and w=0.2.

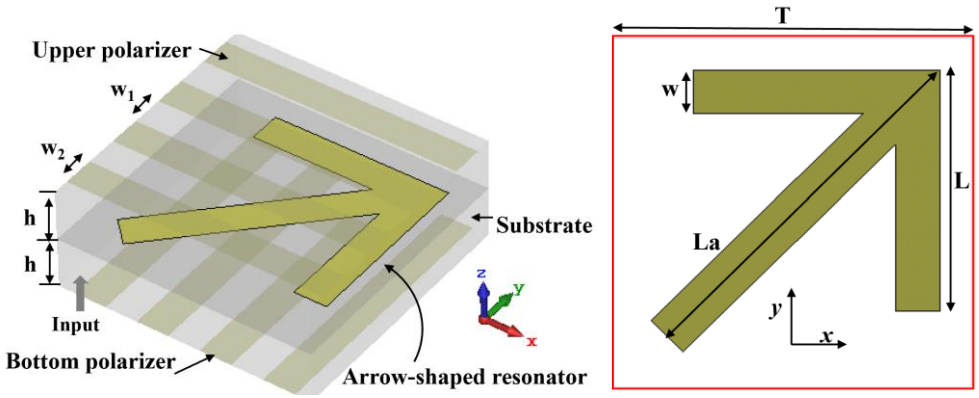

(a) (b)

Fig. 4. 6. Three-dimensional view of the arrow shaped structure. (a) 3-D view; (b) top view of arrow-shaped resonator.

It can be assumed that a normally incident x-polarization electromagnetic waves travels along the +z-direction onto the polarization converter, as shown in Fig. 4. 6 (a). The sides of x and y are set as periodic boundary conditions and the z direction is set to open boundary conditions (open space). Fig. 4. 7 shows the simulated results.

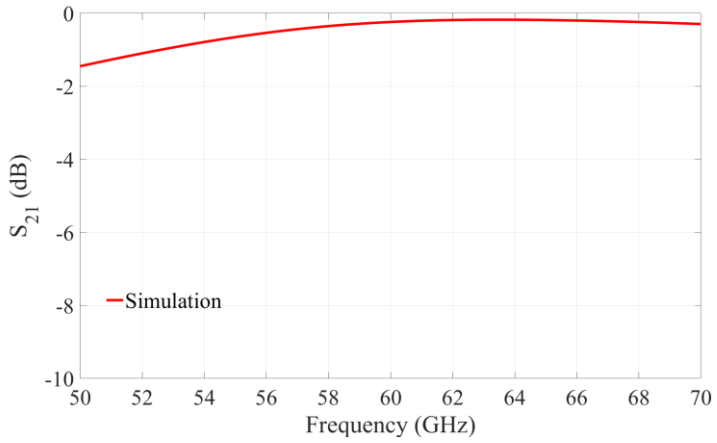

(a)

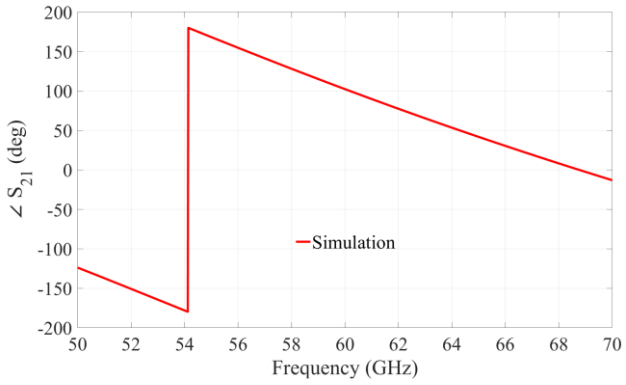

(b)

Fig. 4. 7. Transmission coefficients and phase shift figures of arrow shaped structure. (a) transmission coefficients (S_{21}); (b) Phase shift of S_{21}.

When we change the values of *L* parameters from 0.3 mm to 1.3 mm, the transmission phase would cover more than 200° at 60 GHz, as shown in Fig. 4. 8. From Fig. 4. 8 (a), it can be seen that a high transmission coefficient (<-1dB) is maintained when we tune the parameters of the unit cell. It is worth noting that an additional 180° of phase shift can be obtained by simply mirroring the arrow-shaped resonator about the Y-axis. The mirror shaped resonator can easily be created using printed circuit board technology, but it would be difficult to achieve this mirroring dynamically.

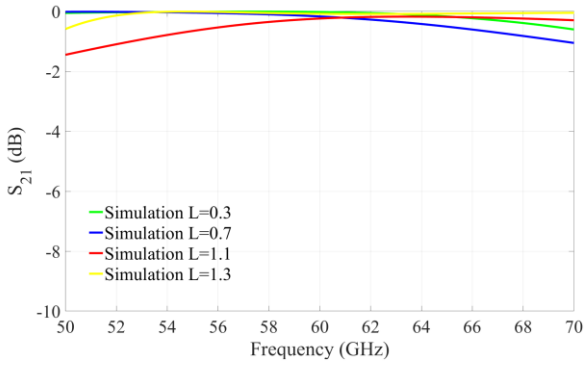

(a)

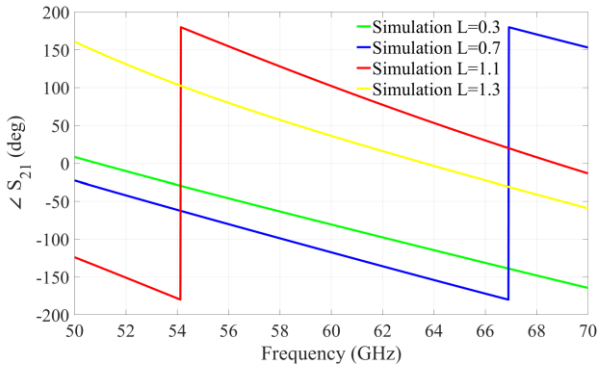

(b)

Fig. 4. 8. Transmission behaviors of the arrow-shaped unit cell. (a) Transmission coefficients (S_{21}) and (b) phase shift figures versus the different length of *L*.

In the following section, the combination of this arrow shaped structure and the SRR unit cell is proposed to extend the phase shifting range.

4.2.2 Unit Cell Configuration

Based on the afore-mentioned simulation, we found that the two structures, shown in Fig. 4. 3 and Fig. 4. 6 both have the capability to convert the polarization of the wave. Thus, we combine them together to expand the phase shifting range of unit cell.

Fig. 4. 9 shows the three-dimensional (3D) view of the proposed unit cell. It consists of three conducting layers separated by dielectric substrates. The dielectric substrates are RO4003c with a permittivity of 3.55 and a loss tangent of 0.0027. Each of the three conducting layers incorporates a different resonator geometry. The arrow-shaped resonator has the capability to convert the polarization of a propagating wave [107]. It is orientated diagonally and placed on the middle layer. The split ring resonators, on the upper and lower conducting layers, have the same size but different orientations. Specifically, the incident wave with Y-axis polarization excites the unit cell. Due to the action of the arrow-shaped resonator, the output wave is polarized along the X-axis, as shown in Fig. 4. 9.

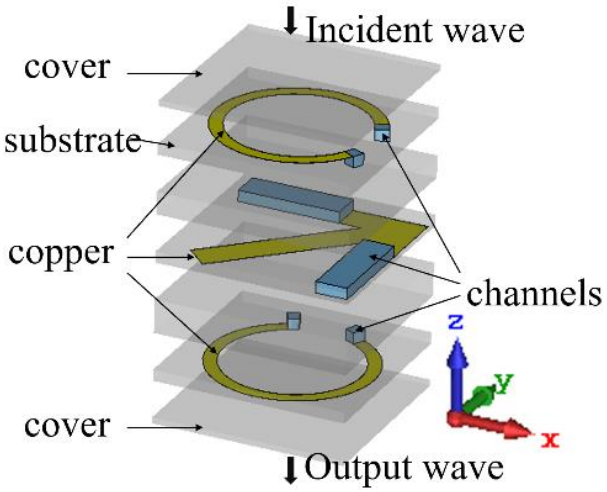

Fig. 4. 9. Three-dimensional (3D) view of the proposed unit cell.

Fig. 4. 10 (a) and (b) show the top views of the split ring and the arrow, respectively. Table 4. 1 gives the optimized parameters of the unit cell. By tuning the length of the arrow arm along with the gaps of the split rings, the transmission behavior of the unit cell can be tuned. To do this, the channels within the unit cell must be filled with liquid metal. Fig. 4. 10 (c) shows the cross-sectional view of the proposed unit cell that can be tuned using liquid metal. The air channels are marked by blue color. These channels are made by cutting some slots into the dielectric substrates. The channel has a depth of 1.52 mm These channels are placed beneath/above each conducting layer. In that case, the liquid metal can be in contact with the printed copper, thus the expected parameters (i.e. the arrow arm length and the gaps of the split rings) can be tuned. Another two substrate layers are employed to form the uppermost and lowermost layers and act as covers to prevent the liquid metal from leaking out of the channels.

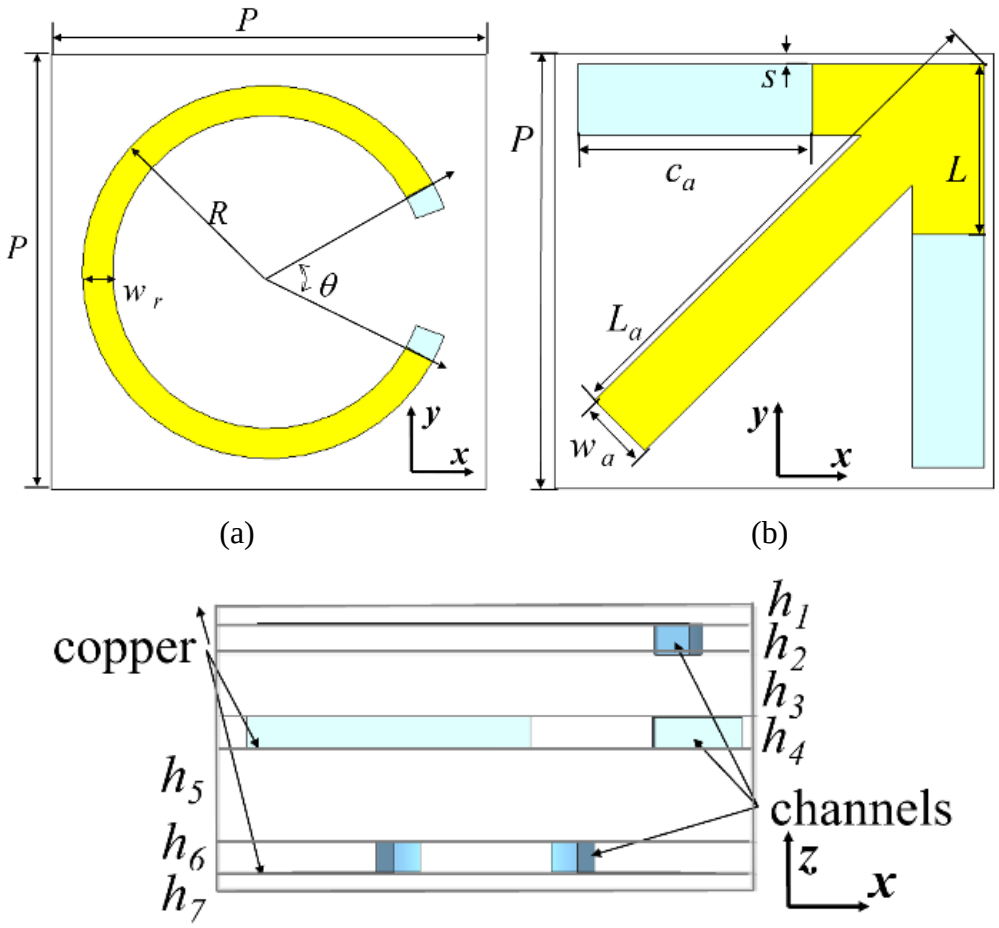

Fig. 4. 10 Top view of the (a) split ring resonator, and (b) arrow-shaped resonator. (c) Cross-sectional view of the unit cell in the XZ-plane.

Table 4. 1. Optimized Dimensions of The Design Unit Cell (Unit: mm)

P	***R***	w_r	w_a	***s***	c_a	***L***
26	11.16	1.8	4.2	0.68	13.9	10.1
L_a	***θ***	h_1	h_2	h_3	h_4	h_5
26	57	0.813	1.52	3.04	1.52	4.56
h_6	h_7					
1.52	0.813					

4.2.3 Simulated Results

The transmit-array unit cell is designed in an infinite array environment with Floquet ports excitation using CST Microwave Studio 2019. The arrow arm length and the gaps within the split rings are tuned by injecting liquid metal into the channels. In turn, this tunes the transmission behavior of the unit cell including the resonant frequencies and transmission phase. The tuning process has two steps: 1) tune the gaps of the double split rings simultaneously; 2) tune the length of two arrow heads. Table 4. 2 shows three typical states. When there is no liquid metal in all channels, the state is called State 1. When the gaps within the split rings on different conducting layers are full of liquid metal, the state is called State2. State 3 is obtained when all of the channels are filled with liquid metal. Those channels include the gaps of within the double split rings and the arrow heads. Fig. 4. 11 shows the simulated results for the three stated, shown in Table 4. 2. From Fig. 4. 11 (a), it can be seen that the resonant frequency alters as the state alters. Fig. 4. 11 (b) shows the corresponding transmission phase ($\angle S_{21}$) for the three states. When the state of unit cell alters from State 1 to State 2, the transmission phase is tuned from -57° to -147° at 3.3 GHz. When the state of unit cell alters from State 2 to State 3, the transmission phase is tuned from -147° to -377°. As a result, the total phase shifting range of the unit cell for the two tuning steps is around 330° at 3.3 GHz with 1.5 dB insertion loss. The unit cell has a 3-dB transmission bandwidth from 3.2 GHz to 3.43 GHz.

Table 4. 2. States of Liquid Metal

State *i*	Channels	
	Double-rings channels	Arrow-head channels
1	No liquid metal	No liquid metal

2	Full of liquid metal	No liquid metal
3	Full of liquid metal	Full of liquid metal

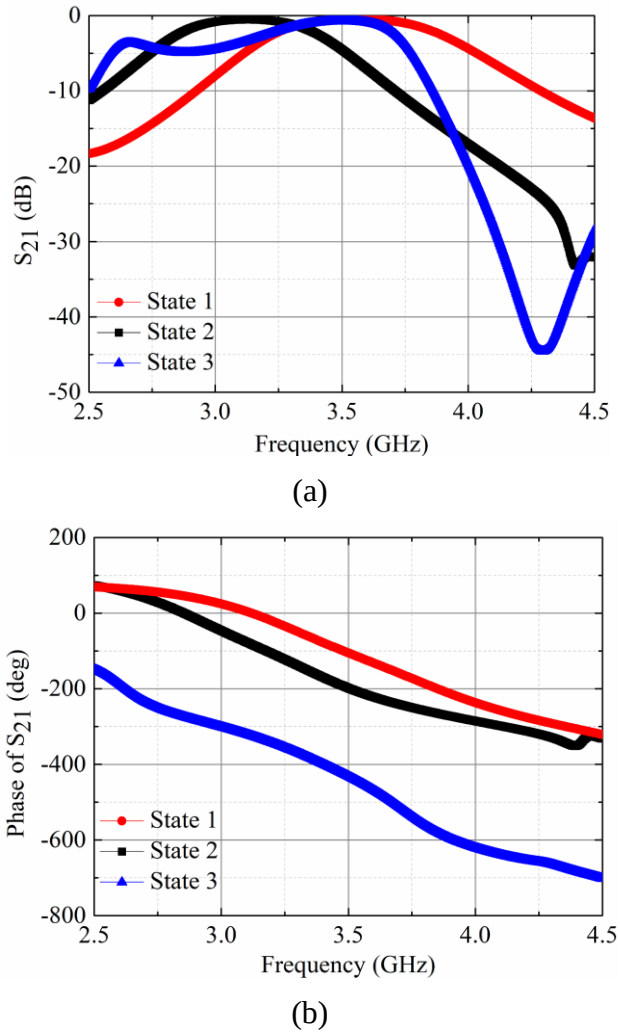

Fig. 4. 11. (a) Transmission coefficient and (b) transmission phase of the three states.

A parameter study has been performed in order to investigate the sensitivity of the proposed unit cell. The study was undertaken within the full-wave simulation tool CST Microwave Studio. Based on our parametric study, the widths of spit rings and arrow (including the width of liquid metal channels) primarily determine the resonant frequency and transmission coefficient of the unit cell, respectively. As shown in Fig. 4. 12, increasing the width of split rings increases the resonant frequency, and increasing the width of the arrow section reduces the transmission coefficient. The

transmission phase shift will not be significantly influenced. Actually, the insertion loss of the proposed unit cell could be further improved by tuning the widths of rings and arrow sections. However, to reduce the difficulty of injecting the liquid metal in practice, we tried to make the channels wider whilst still providing an acceptable transmission coefficient.

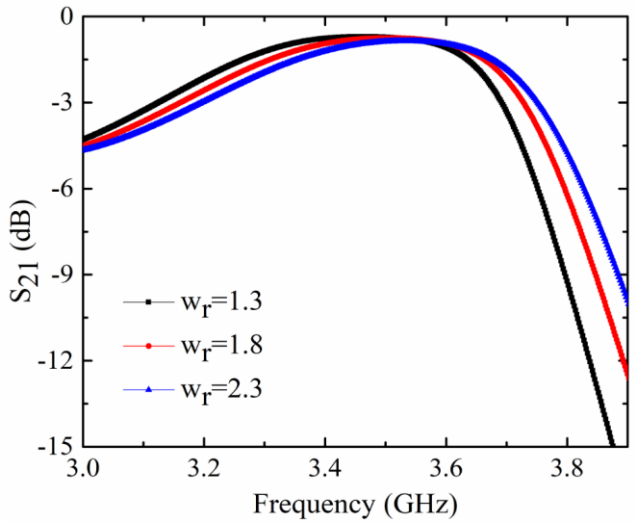

(a)

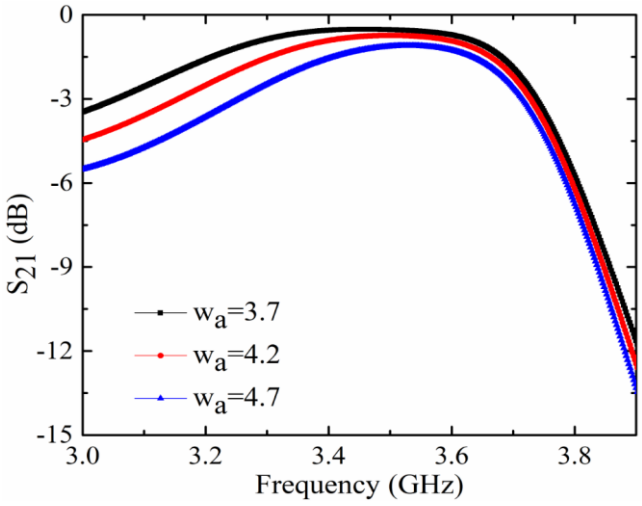

(b)

Fig. 4. 12. Parameter studies on (a) the width of rings and (b) the width of arrow.

4.3 Fabrication and Measured Results

In this section, we firstly discuss our fabrication of channels and injection of liquid

metal. Then we discuss the measurement setup and measured results of the proposed unit cell. Finally, we do some investigation on different actuations of liquid metal.

4.3.1 Fabrication of Channels and Injection of Liquid Metal

Generally, Polydimethylsiloxane (PDMS) is used to fabricate the liquid metal channels due to its high gas permeability. It needs three main processes, namely: 1) master mold fabrication; 2) microfluidic device fabrication; 3) bonding the device to PCB. Different from the above approach, we fabricated the liquid metal channels by cutting slots into a dielectric substrate. Fig. 4. 13 shows the fabricated unassembled unit cell and its channels. This approach is suitable for channels that do not have a complex 3D shape. Additionally, microwave dielectric substrates provide good and stable RF performance, which will not worsen the performance of antenna a lot, whilst PDMS would bring a lot of uncertainties. For example, the major manufacturer of PDMS (Dow Corning) reports two values for the 184 kit (mix two components 10:1) with a permittivity of 2.72 and a loss tangent of 0.0025 at 100 Hz and with a permittivity of 2.68 and a loss tangent of 0.0013 at 100 kHz. Both values are at relatively very low frequencies. Some literature reported that the permittivity and loss tangent of PDMS at higher frequencies. In [120], the permittivity and loss tangent of PDMS are 2.8 and 0.02 at about 0.8 GHz to 7.9 GHz, respectively. However, in [121], it reports that the loss tangent of PDMS shows a linear rise with frequency. As a result, the effect of these uncertainties on properties of PDMS would worsen the performance of antenna.

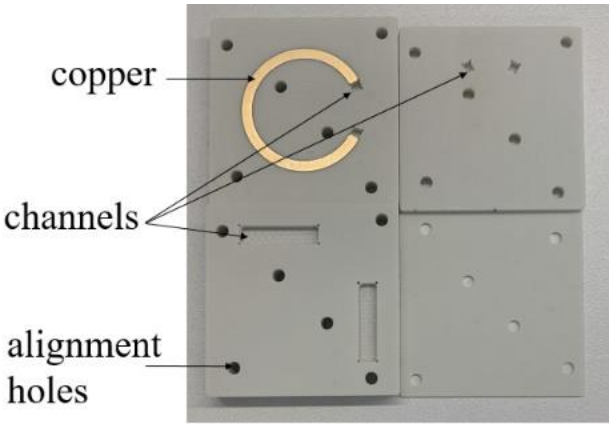

Fig. 4. 13. The unassembled unit cell and its channels.

In the proposed design, we employ the liquid metal based around an alloy consisting of 75% Gallium and 25% Indium, which is commercially available. The conductivity of such gallium-based liquid metal is 3.4×10^6 S/m. As discussed in Section 2.3 of Chapter 2, it is liquid at room temperature and non-toxic. The liquid metal was moved into (or withdraw out of) desired positions using a syringe. Fig. 3. 14 shows the ground plane drained by a syringe. This technique is widely used in the literature within proof-of-concept designs [99], [122]. Other possible approaches for actuating liquid metal will be discussed in the later Section 4.3.3.

Fig. 4. 14. The ground plane drained by a syringe.

4.3.2 Measurement Setup and Measured Results

The transmit-array unit cell was simulated with periodic boundary conditions and Floquet port excitation. This means that the unit cell was simulated within a structure which is infinite. However, it is impossible to fabricate such an infinite structure and test the performance of a unit cell which is optimized under the above condition. The waveguide method is an effective alternative to verify the performance of a unit cell, and several previous works have used such measurement approach [57], [100]. When using waveguide method, two standard waveguides need to be added at both ends of the unit cell. However, unit cell usually does not have the same size with the standard waveguide. For that reason, two additional tapered transitions between the standard waveguides and the unit cell are needed. Such an additional transition structure will increase the complexity. Besides, due to the polarization rotation of the proposed unit cell, the above test structure is not suitable here.

Fig. 4. 15 shows the assembled unit cell inside at the end of waveguide. In this work, an open-ended waveguide measurement setup is employed. The unit cell is excited by a standard WR284 waveguide (72×34 mm^2) on one side. The unit cell does not have the same cross-sectional dimensions as the end of the waveguide. For that reason, a metallic holder was fabricated to hold the unit cell at the end of the waveguide. By injecting liquid metal into the channels, it will be possible to alter the gaps within the split rings (θ) and the length of the arrow heads (Ca). In this chapter, we demonstrate a design having three reconfigurable states, as shown in Table 4. 2 of Section 4.2.3. We manually injected the liquid metal using a syringe as mentioned above.

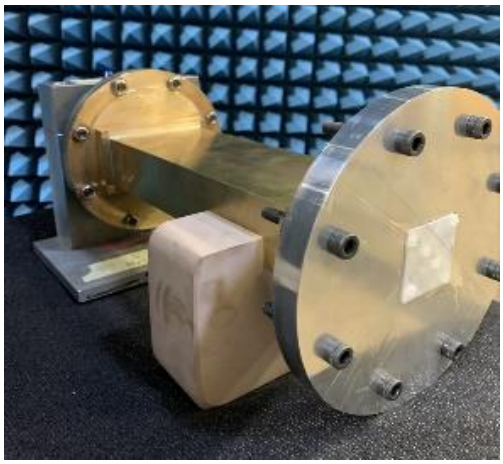

Fig. 4. 15. The unit cell inside at the end of waveguide.

Fig. 4. 16 (a) shows the measurement setup system. A horn antenna was used to receive the signal transmitted from the section of waveguide incorporating the unit cell. The horn was placed at a distance of one meter from the unit cell. Due to the different environment between simulation and measurement, there should be a difference between the measured results and the simulated results shown in Fig. 4. 11. As a result, we cannot directly compare the measured results with the simulated results, shown in Fig. 4. 11. In this case, a system with the electrical boundary conditions as the measurement was simulated. Fig. 4. 16 (b) shows the configuration of this measurement system. We compare the measured results with the simulated results of Fig. 4. 16 (b) to verify that we can model the unit cell correctly within the simulation environment. If so, we could assume that the simulated results of the previous unit cell with periodic boundary conditions are also correct.

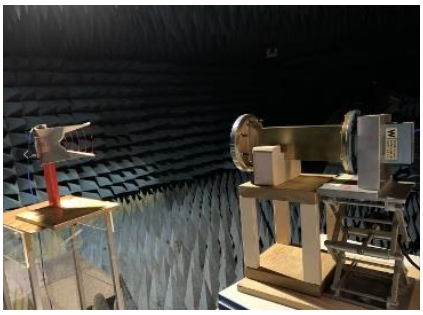

(a)

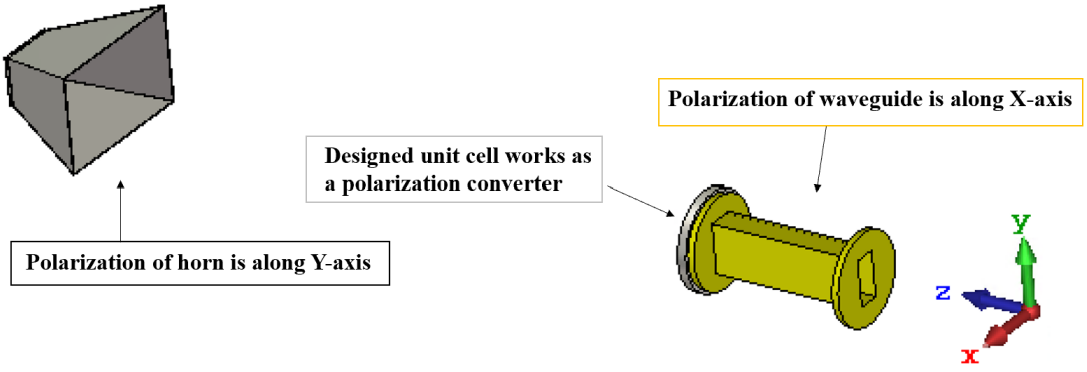

(b)

Fig. 4. 16. The experimental setup of the open-ended waveguide. (a) The setup testing system. (b) The configuration of the simulation system which has the same settings as the measurement.

Fig. 4. 17 shows the comparison between measured and simulated results of the proposed unit cell for three reconfigurable states. It plots the transmission coefficients (S_{21}) and phases for the States 1, 2, and 3 with respect to frequency. It can be seen that the measured results agree well with the simulations. The black curves in Fig. 4. 17 (a), (b) and (c) show the simulated transmission coefficients of the unit cell for three states. The red curves in Fig. 4. 17 (a), (b) and (c) show the measured transmission coefficients of the proposed unit cell for corresponding states.

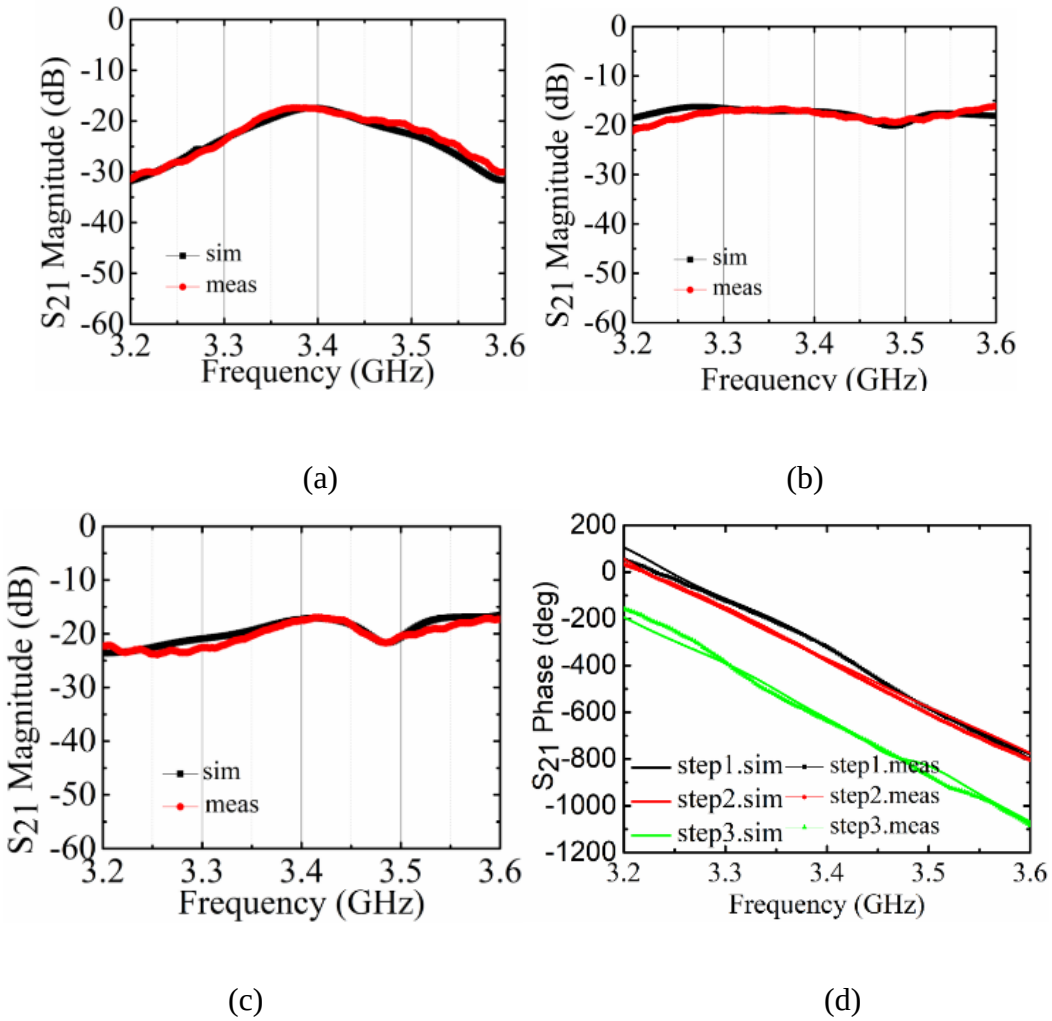

Fig. 4. 17. Simulated and measured transmission coefficient of the transmit-array unit cell under the measurement setup for (a) State1, (b) State2, and (c) State3. (d) Simulated and measured transmission phases of the States 1, 2, and 3 versus frequencies.

Form Fig. 4. 17 (a), (b) and (c), it can be seen that the measured transmission coefficients are around 0.2 dB lower than the simulated values. This might be caused by alignment errors, fabrication errors, or larger material loss. It is worth noting that the measured transmission coefficients have lower values than simulated results, under periodic boundary conditions, shown in Fig. 4. 11. This is mainly due to the open space, between the horn and the unit cell, which increases the attenuation of the transmission coefficient by introducing free-space path loss. Additionally, the difference in size between the unit cell and the cross-sectional dimensions of the waveguide introduce

additional attenuation. Based on the good agreements, it is clear that we can model the unit cell correctly within the simulation environment. Consequently, it is reasonable that the simulations of the previous unit cell with periodic boundary conditions are correct. They can be verified if we could provide the same boundary conditions in practice. We assume that there would be a constant the difference between the simulation and the measurement. In that case, the measured transmission coefficient of unit cell under periodic boundary conditions should also be 0.2 dB lower than the simulations. Thus, it is assumed to be 1.6 dB.

Fig. 4. 17 (d) shows the simulated and measured transmission phase for States 1, 2, and 3. The measured transmission phase shifts are in good agreement with the simulated ones. It can be seen that the measured phase shifting range remains more than 300°, and the phase difference between simulation and measurement is ~10°, which is only ~3% of the phase shifting range.

In summary, based on the measured results, we reasonably presume that the proposed transmit-array unit cell can provide a more than 300° phase shifting range within transmission coefficient of 1.6 dB. This represents a good improvement on the insertion loss compared with designs, reported previously in the literature, for electronically reconfigurable unit cells involving varactors. Table 4. 3 compares the transmission properties of reconfigurable transmit-array unit cell, reported previously in the literature, with those of the unit cell reported in this chapter.

Table 4. 3. Comparison for Unit Cell Performance

Ref.	Frequency (GHz)	Phase shifting range (deg)	Insertion loss (dB)	Control method
[18]	5.4	360°	2.8	Varactors
[19]	4.8	360°	5.1	Varactors

[65]	5	400°	3.6	Varactors
[67]	5.2	245°	3	Varactors
Our work	3.3	330°	1.6	Liquid metal

4.3.3 Discussion on Actuation of Liquid Metal

Ideally, we could continuously tune the arrow arm length and the gaps within the split rings. In that case, the phase of the proposed transmit-array unit cell could also be continuously tuned over a range of 300°. However, in this chapter, we only measure the design having three reconfigurable states, shown in Table 4. 2 of Section 4.2. The number of achievable states is limited by the accuracy with how the liquid metal can be controlled. As a result, the continuous control is not currently possible due to limitations on our controlling method. We try to improve it in our future work and did some review on this topic as follows.

Commonly, the liquid metal can be controlled mechanically or electronically. The following methods are commonly used to control liquid metal:

1. Pressure controlling method: using external pressure through syringe or pump to actuate the liquid metal.

2. Electrochemically controlled capillarity (ECC): liquid metal is on one side of the channel and electrolyte solution, such as Sodium Hydroxide (NaOH), is on the other side of channel. There will be an oxide layer at the intersection of the two materials. By adding a forward or reverse bias voltage, it causes a change in the charge on the oxide layer. This leads to a change in the surface tension of the liquid metal and drives the flow of liquid metal.

3. Continuous electrowetting (CEW): liquid metal is placed in a channel filled with

the electrolyte solution. By adding bias voltage on the two sides of electrolyte solution, the charge on the surface of liquid metal is asymmetric. This results in different surface tensions on the two sides of liquid metal, which causes the movement of liquid metal.

Different methods have their own advantages and disadvantages. For example, mechanical method (Method 1) is easy to actuate, but it is difficult to integrate with antennas. Electronical method (Methods 2 or 3) is easy to integrate with antennas and to accurately control the movement of liquid metal. However, the bias voltage is complex and makes the antenna efficiency low. Fig. 4. 18 shows the components that would be involved in the electronic controlling systems.

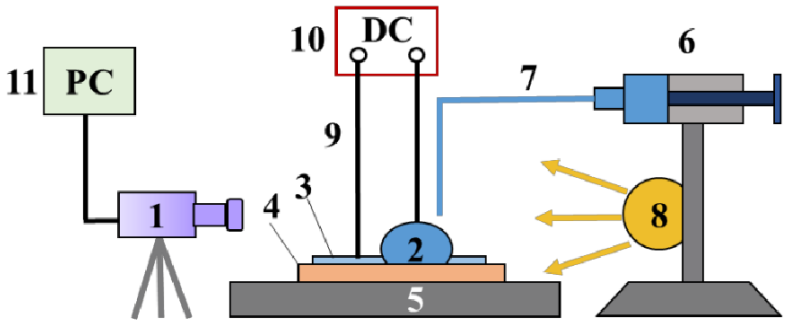

Fig. 4. 18. Diagram of the electronic control system.

Where 1 is camera, 2 is liquid metal, 3 is electrolyte solution (like NaOH solution), 4 is liquid metal channels, 5 is the experiment platform, 6 is injection pump, 7 is tube, 8 is light, 9 is link wire, 10 is DC power, and 11 is a computer. The system shown in Fig. 4. 18 has five sub-systems, namely: 1) liquid metal system (including 2, 3, 4, and 5); 2) injection system (including 6 and 7); 3) lighting system (including 8); 4) voltage supply system (including 9 and 10); and 5) image acquisition system (including 1 and 11).

In our experiments liquid metal was injected into and removed from the unit cell using a syringe. This actuation approach is commonly used, and several papers adopt this approach for actuation of liquid metal [159]-[167]. Several other actuation techniques are also reported in literature such as: 1) the use of a micropump [102], [169]-[172] or 2) the use of electrochemically controlled capillary action [168], [173]. Although liquid metal actuation is not within the scope of the research reported in this chapter, it is important to enable practical application of the technology. To make the design more practical, we did some experiments to improve the actuation of liquid metal. Our preferred method of actuating the liquid metal is to use a pump. Fig. 4. 19 illustrates the injection of liquid metal into a test antenna using the pump system. This is a simple control system now. Given more time we would further improve it.

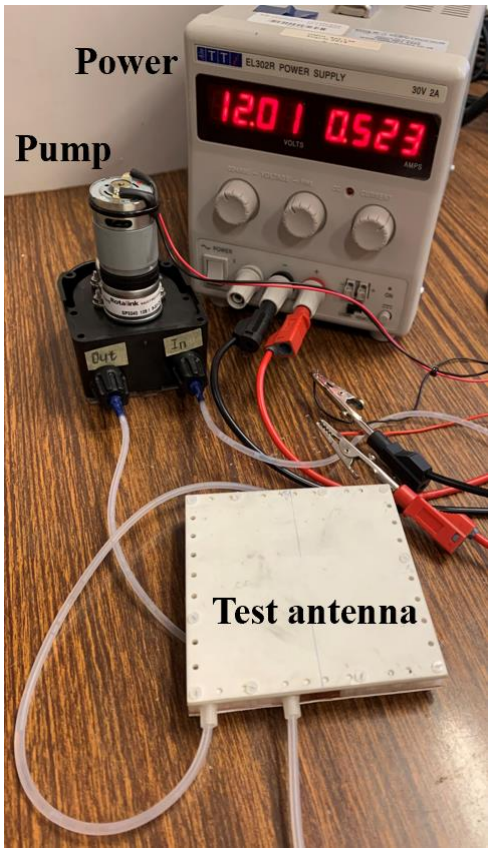

Fig. 4. 19. The injection of liquid metal into a test antenna using the pump system.

4.4 Chapter Summary

This chapter presents a reconfigurable unit cell for use within transmit-array applications. It is tuned by employing liquid metal. The proposed unit cell incorporates three conducting layers with different geometries. Several channels are placed beneath/above the conducting layers. The transmission behavior of the unit cell can be changed by changing the geometrical parameters of the unit cell. This is achieved by injecting liquid metal into the channels. The proposed unit cell was fabricated and measured within an open-ended waveguide. The measured results agree well with the simulations and verify that we can model the unit cell correctly within the simulation environment. Based on the measurement, it is reasonable to get a conclusion that the proposed unit cell could provide a more than 300° phase shifting range with a maximum S_{21} of ~ -1.6 dB. The proposed unit cell exhibits 3 dB of insertion loss over a bandwidth ranging from 3.2 GHz to 3.43 GHz. Compared with other electronically reconfigurable unit cells using varactors, the proposed unit cell yields a good improvement on the insertion loss. The proposed prototype is an attractive candidate for future transmit-array applications. A discussion about the actuation of liquid metal is also given at the end of this chapter. Those work could be done to improve the design in the future study.

Chapter 5 Reconfigurable Microstrip Patch Antennas with Switchable Liquid-Metal Ground Plane

Two beam switchable patch antennas are presented in this chapter. The proposed antennas employ two approaches in unison to switch the direction of the main beam. Specifically, the antennas use the parasitic steering approach together with a switchable ground plane. To the best of my knowledge, this is the first time that the antenna is capable of reconfiguring its radiation pattern by reshaping the ground plane using liquid metal. These antennas operate at 5.9 GHz, and they are termed Design #1 and Design #2. Design #1 provides five switchable beams. The beam switching angles are evenly distributed. The maximum switching angle is ±40° with less than 0.5 dB of scan loss. Design #2 provides three switchable beams, namely 0° and ±68° with ~2 dB of scan loss. The proposed antennas were fabricated and measured. The measured results agree well with the simulated results. Measured results validate the effectiveness of the proposed antennas and the novel switching technique. The switching technique will find numerous applications within future wireless communications systems.

5.1 Introduction

Emerging wireless communication scenarios require high-capacity channels to support a large number of users. Reconfigurable antennas are one of the solutions due to their advantages, including: ability to enhance communication security, improve channel capacity, and adapt to changing channel conditions [124] - [129]. For example, a pattern reconfigurable antenna can alter its main beam direction to transmit or receive preferentially from different directions. This could be used to accommodate multiple users. The first reconfigurable antenna was proposed by Schaubert in 1983 [129]. Since then, many different types of reconfigurable antennas have been proposed. Typical

reconfigurable antennas have the capability of changing the operating frequency, polarization, radiation pattern, or a combination of the above [131] - [133]. Among them, pattern reconfigurable antennas have gained widespread attention. Microstrip antennas are one of the most popular candidates in designing the reconfigurable antennas due to their low cost, low profile and conformal ability.

Commonly, a pattern reconfigurable microstrip antenna may be controlled mechanically or electronically. For example, pattern reconfiguration can be achieved by mechanically changing the distance between the antenna and the reflector [89]. However, mechanical moving parts are undesirable, for many applications, because they require periodic maintenance, repair, and replacement. Electrically controlled reconfigurable antennas widely use PIN diodes, varactors or microelectromechanical switches (MEMS). For example, parasitics with varactors can realize pattern reconfiguration by changing the antennas input impedance [95]. Microwave switches, such as PIN diodes or MEMS, are widely used in various different designs, including: altering the current path [85], [134], switching the load [96], switching the feed network [85], and switching parasitic elements on or off [134]. Conventional microwave switches have fast response time but also suffer from high insertion loss and nonlinear distortion. Liquid metal as the new material could be electrically controlled, and it still has the advantages of low insertion loss, low harmonic distortion, and large tuning ranges [97], [99], [98].

In previous literature, pattern reconfiguration was achieved by changing the ground plane [72], [73], [81], [82]. Approaches involve altering the eigenmode supported by the radiator [72], [81], or using parasitic elements to direct or reflect beams [73], [82]. For example, a reconfigurable patch antenna was proposed in [72]. By tuning on the

different combinations of switches, it is possible to connect vertical metal walls to the patch antenna. The main beam direction is thus altered by varying the eigenmode supported by the patch antenna. However, the antenna proposed in [72] exhibits more than 2 dB scan loss over a scan angle range of ±20°. The vertical metal walls also increase the profile of antenna. The slot antenna, proposed in [82], has low profile. It incorporates one slot which acts as a radiator together with four slits which act as parasitics. By tuning on the different switches, located within the slits, it is possible to alter the behavior of the slits and thus control the beam reconfiguration. However, the antenna can only steer its beam to a maximum angle of ±15°. The geometry of the design in [75] looks similar to the design presented herein. However, the working principle is different since the design presented in [75] only applies parasitic patches but no switchable ground, whilst our design combines the parasitic patches with switchable ground plane. This enables the proposed design to switch beam up to ±40° with only 0.5 dB of scan loss, while the design in [75] achieves a maximum angle of ±15° with 1.3 dB of scan loss. As a result, our design differs from the designs, discussed above, in both approach and performance. Using liquid metal to form and reshape the ground plane is a totally new method to reconfigure the radiation pattern of an antenna. Also, this is the first time that liquid metal has been used to reshape the ground plane. The proposed antennas have a -10 dB reflection coefficient bandwidth range from 5.5 GHz to ~ 6 GHz. They were fabricated and measured at the center frequency of 5.9 GHz. The measured results show that the antennas have good beam switching performance.

5.2 Beam Switching Approaches

The proposed antennas utilize two beam switching techniques in concert. We will refer to the first technique as a parasitic steering technique. The second beam switching

technique involves switching the ground plane. To the best of my knowledge, this is the first time that someone has achieved beam switching by switching the ground plane. In this section, we will present the operating principle and the beam switching techniques in detail.

5.2.1 Design Procedure of the Patch Antenna

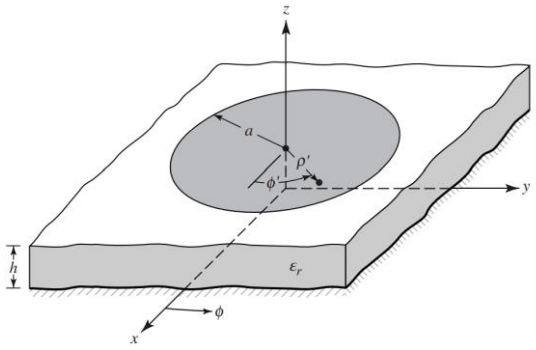

Fig. 5. 1. Geometry of circular microstrip patch antenna [135].

Fig. 5. 1 shows a conventional circular patch antenna. This structure received considerable attention from the research community in the 1970s and 1980s. The fundamental mode supported by the circular patch antenna is the TM_{110} mode. Changing the radius of the patch alters the resonant frequency of the antenna. Equation (5.1) shows the relationship between the radius of patch and the resonant frequency of the antenna.

$$R = \frac{1.8412 * c}{2\pi f_r \sqrt{\varepsilon_r}} \tag{5.1}$$

Where ε_r is the permittivity of the substrate, R is the radius of the patch, and f_r is the resonant frequency of the antenna. Equation 5.1 can be used to roughly approximate the operating frequency of the antenna proposed here [135]. The proposed antenna incorporates several parasitic elements that are coupled to the driven element. This coupling will alter the operating frequency of the driven element. The radius of the

driven element was approximated using Equation (5.1) and then the precise value was determined from the results of a parametric study performed in CST Microwave Studio 2019.

5.2.2 Parasitic Steering Technique

[75] reports an antenna consisting of a driven patch and four parasitics, which is very similar to the configuration shown in Fig. 5. 2. It is a Yagi-Uda antenna, which consists of a radiating patch as well as reflectors and directors. The antenna reported in [75] is capable of switching its main beam direction. Inspired by it, we design a structure with the same geometry as [75] but different parameters. Fig. 5. 2 shows the designed antenna. Table 5. 1 shows the optimized parameters of the antenna. It incorporates two metallic layers separated by a dielectric substrate. The dielectric substrate is RO4003c. The substrate has a thickness of 1.62 mm, a permittivity of 3.55, and a loss tangent of 0.0027. The uppermost metal layer incorporates a driven element and four parasitics denoted parasitic A, B, C, and D. Both driven element and parasitics are circular microstrip patches having the same radius. The parasitics are positioned around the driven element. The lowermost metal layer incorporates the ground plane. The driven patch is excited via a coaxial probe. The coaxial probe is offset along the y-axis by 3.6 mm in order to yield optimum impedance matching. The antenna operates at 5.9 GHz. Another difference between [75] and our design is that in our design liquid metal is used, for the first time, to activate and deactivate the via connections to ground. This is only a small development compared with what has been reported in [75], but we take it as a beginning of our later design.

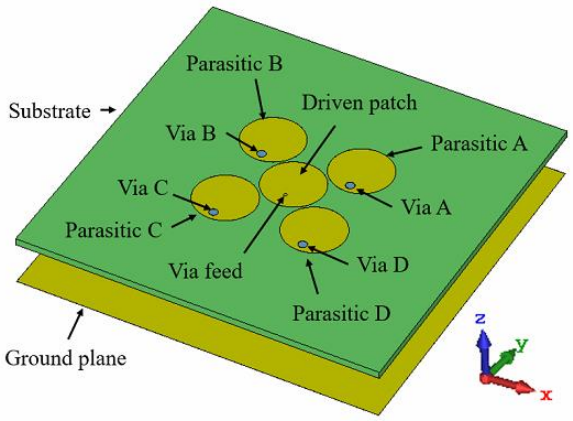

(a)

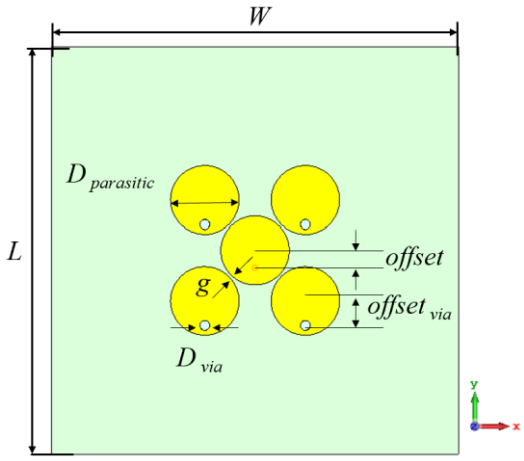

(b)

Fig. 5. 2. (a) Exploded view of the antenna structure. (b) Top view of the antenna.

Table 5. 1. Optimized Dimensions of The Antenna (Unit: MM)

L	***W***	***D parasitic***	***D via***	***g***	***offset***	***offset via***
83	83	14	2	0.5	3.6	5

The operating principle of this design is that of a Yagi-Uda antenna, which consists of a radiating patch as well as reflectors and directors. In this designed antenna, the central patch acts as the driven element and four surrounding patches act as parasitics. Each parasitic incorporates a single drill hole. The drill holes can be filled or emptied of liquid metal. When a particular drill hole is filled with liquid metal, a via is formed and the parasitic is said to be switched ON. Under this condition the associated parasitic

element is connected to ground and acts as a reflector. When the drill hole is emptied, no via is formed and the parasitic is said to be switched OFF. Under this condition the associated parasitic acts as a director. With the aid of these reconfigurable vias it is possible to reconfigure the directions of the radiation patterns.

Based on the above analysis, we know the operating principle. Then a simulation is given to show the beam switching capability of this structure. Table 5. 2 gives the operating states of the proposed structure at 5.9 GHz.

Table 5. 2. States of Drill Holes

State *i*	Via State			
	Via A	Via B	Via C	Via D
1	Off	Off	Off	Off
2	On	Off	Off	On

Fig. 5. 3 shows the reflection coefficients (S_{11}) and the radiation patterns for the different operating states of the antenna shown in Table 5. 2. From Fig. 5. 3, it can be seen that the beam switches towards 0° when all vias are turned OFF for State 1. The beam switches towards -10° in the XZ-plane when vias A and D are turned ON for State 2, i.e. parasitics A and D are connected to the ground plane. Both states of the antenna have good impedance matching at 5.9 GHz.

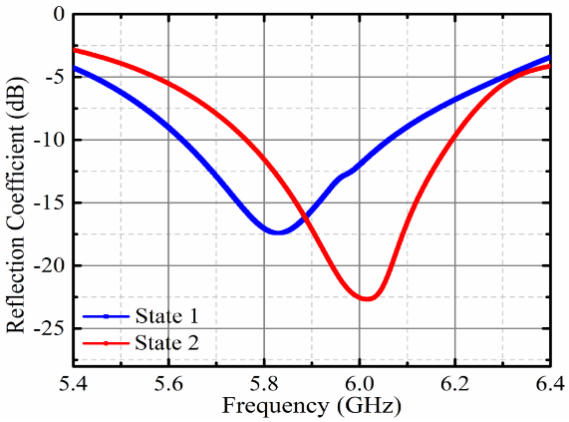

(a)

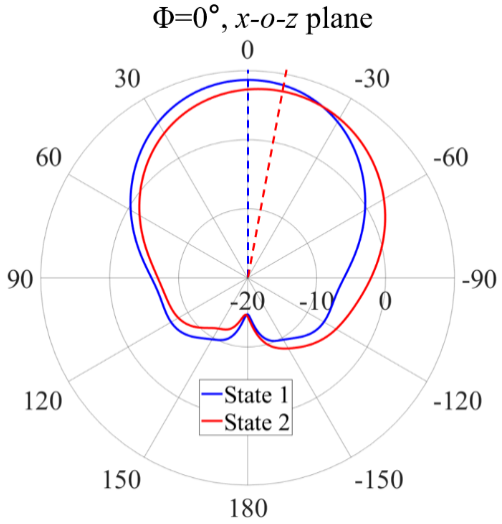

(b)

Fig. 5. 3. (a) Reflection coefficients and (b) radiation patterns of the antenna at 5.9 GHz for different states.

As a result, we can conclude that the parasitic steering technique is an effective method for switching the main beam direction. It is worth noting that the structure is symmetrical along the Y-axis. For this reason, beam pointing towards +X-axis directions could be obtained by simply mirroring the states of vias along with the Y-axis.

5.2.3 Switchable Ground Plane

Inspired by the parasitic steering technique, we think it might be possible to switch the

main beam direction if sections of the ground plane could be switched in or out. Consequently, we built a circular-patch antenna with several switchable ground planes, as shown in Fig. 5. 4. It consists of a circular patch and five rectangular ground planes. We assume that the four ground planes are switchable, and the center ground plane is permanentl. The substrate is FR-4 with a permittivity of 4.4 and a thickness of 3.6 mm. When all grounds are present, the antenna provides a broadside beam. When one of the parasitic grounds is removed, then the beam switches towards the direction in which the ground plane has been removed. Fig. 5. 4 (b) shows the case when the Ground 2 is removed. Fig. 5. 5 shows the radiation pattern of this case. It can be seen that the beam switches towards -30°. More importantly, we found that the width of Ground 2 primarily effects the switching angle, which will be discussed in detail in the next paragraph. As a result, we combine the switchable ground plane together with the parasitic patches.

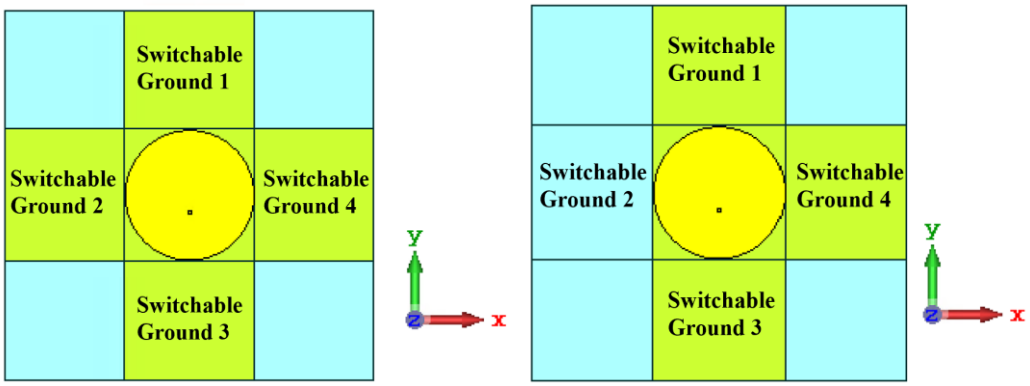

(a) (b)

Fig. 5. 4. A circle-patch antenna with several parasitic grounds. (a) All switchable grounds are present; (b) Switchable Ground 2 is removed.

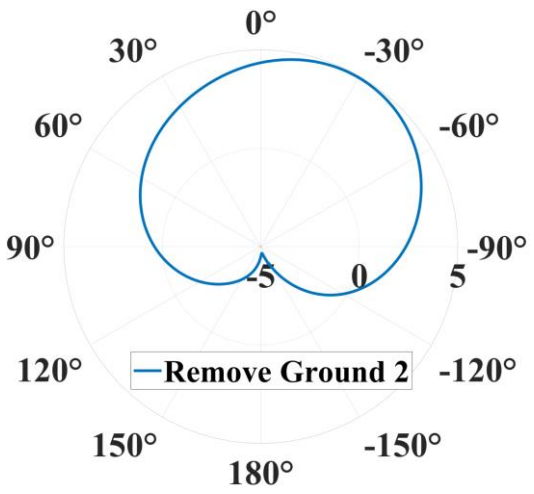

Fig. 5. 5. The radiation pattern of antenna when the Ground 2 is removed.

Fig. 5. 6 shows the sketch of the proposed switchable ground plane together with parasitic patches. It involves switching segments of ground plane ON and OFF. Specifically, we segment the ground plane around the driven element into three pieces, named Ground 1, Ground 2, and Ground 3. This approach preserves the symmetry about the Y-axis, shown in Fig. 5. 6. The section of ground plane located directly below the driven element is named Ground 2 and is permanently in place. The sections of ground plane located to the left and right, of the driven element, are named Ground 1 and Ground 3. Ground 1 and Ground 3 are formed from liquid metal. This enables them to be added (switched ON) or removed (switched OFF) as required. Doing so influences the main beam direction. Fig. 5. 7 shows the sketch of main beam directions for different states of ground. The beam switches towards the direction in which the ground plane has been removed as mentioned earlier. So, for example, the beam switches towards the –X-axis direction when we switch the Ground 3 ON. The angle of the main beam can be controlled by altering the width of Ground 2. This can be achieved by altering the value of $offset_{ground}$. Fig. 5. 8 shows the effect of changing $offset_{ground}$ from 0 mm to 5 mm. It can be seen that the beam switches to 20° when $offset_{ground}$ is set to 0 mm for this structure. The main beam angle decreases when the width of Ground 2 (i.e.

offset $_{ground}$) increases. From Fig. 5. 8 (a), we know that the reflection coefficient at 5.9 GHz remains below -10 dB for all of the *offset* $_{ground}$ values considered. Thus, the switchable ground plane is also an effective approach to reconfigure the pattern of antenna.

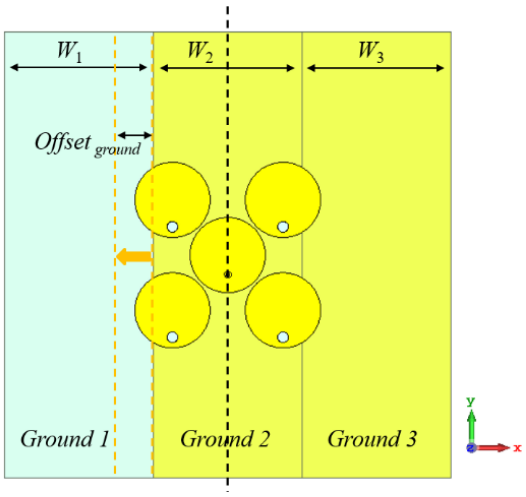

Fig. 5. 6. The sketch of the switching ground plane. W_1= W_2= W_3=27.6 mm.

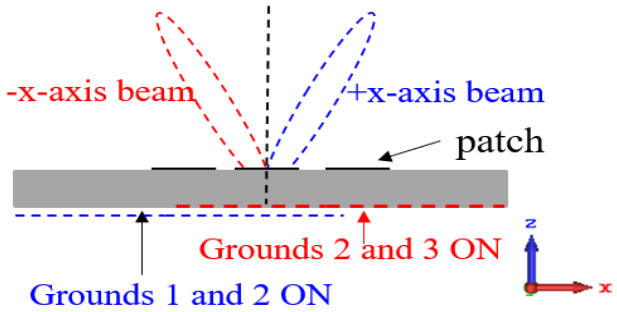

Fig. 5. 7. The sketch of beam directions for different states of ground.

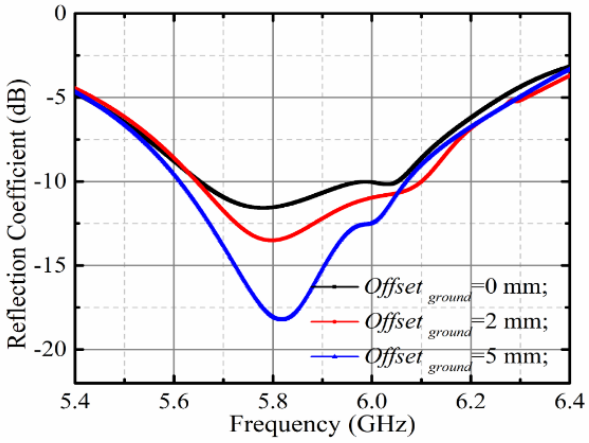

(a)

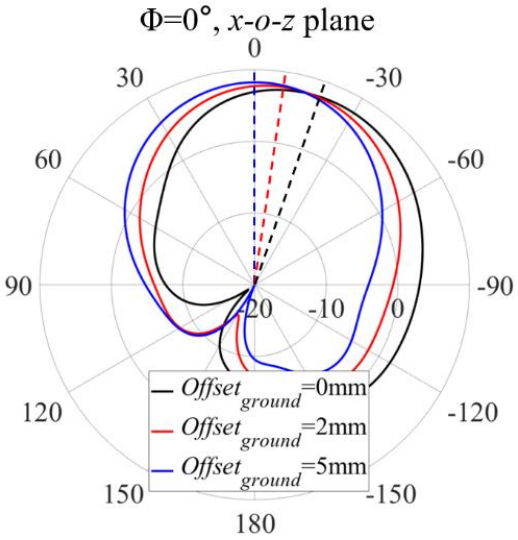

(b)

Fig. 5. 8. (a) Reflection coefficients and (b) radiation patterns of the antenna at 5.9 GHz when we tune the ground plane.

5.3 Antenna Design and Fabrication

We propose two pattern reconfigurable antennas, which we will refer to as Design #1 and Design #2. The only difference between them is that Design #1 incorporates a metallic reflector whilst Design #2 has no reflector. For that reason, we mainly introduce the geometry and dimensions of Design #1 in this section.

5.3.1 Antenna Design

Fig. 5. 9 shows the geometry and parameters of the antenna. Table 5. 3 shows the optimized parameters of the antenna. The antenna consists of a driven patch surrounded by four parasitics. The driven patch and parasitics are all circular in shape. Energy is fed into the antenna using a coaxial fed probe. The probe is offset along the Y-axis by 3.6 mm in order to yield optimum impedance matching. The antenna is constructed using four layers of substrate, namely L_1 to L_4. Each layer of substrate is formed from a piece of Rogers RO4003c having a thickness of 0.813 mm, a permittivity of 3.55, and a loss tangent of 0.0027. Each parasitic incorporates a single drill hole which passes through substrate layers L_2 and L_3. The lowermost and uppermost layers of the substrate (i.e. L_1 and L_4) are employed as covers to prevent the liquid metal from leaking out. Two large channels are formed in substrate layer L_2. When those channels are filled with liquid metal, they form Ground 1 and Ground 3. Ground 2 is formed from copper and remains permanently in place. It is worth noting that a metallic reflector is placed behind the antenna for Design #1, as shown in Fig. 5. 9 (c). Design #2 has the same structure and geometrical parameters as Design #1. However, it does not incorporate a metallic reflector.

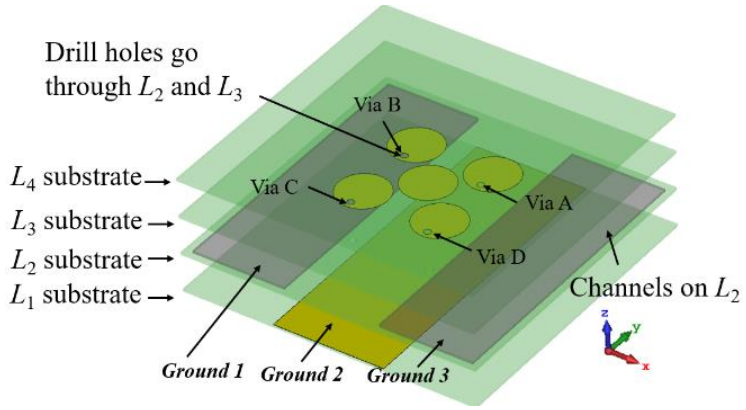

(a)

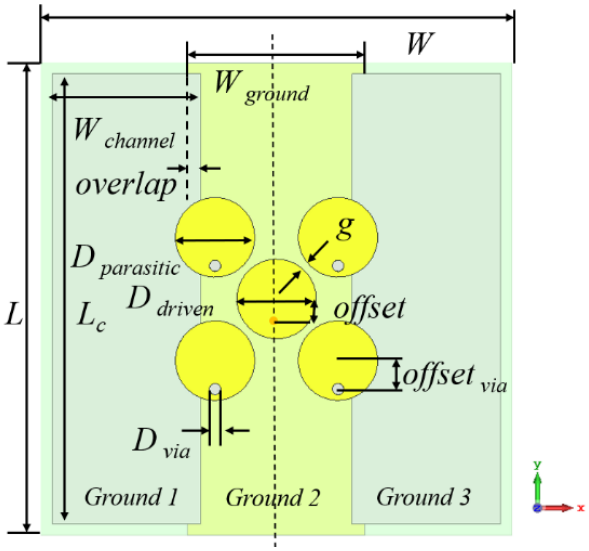

(b)

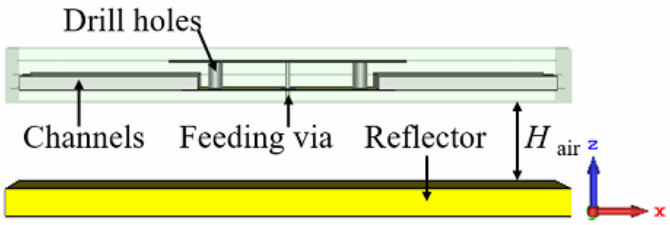

(c)

Fig. 5. 9. Geometry and parameters of the pattern-reconfigurable antenna. (a) Perspective view; (b) Top view; (c) Side view of Design #1.

Table 5. 3. Optimized Dimensions of The Design #1 Antenna (Unit: MM)

L	***Lc***	***W***	***W channel***	***W ground***	***D driven***	***D parasitic***
83	79	83	26.1	31.26	14	14
D via	*g*	*offset*	*offset via*	*overlap*	*H air*	
2	1.3	3.6	5	2.3	5	

The proposed antenna employs two approaches in unison, as mentioned above, to switch the direction of the main beam. The first approach, for beam switching, involves parasitic steering. In the proposed antennas, the central patch acts as the driven element and four surrounding patches act as parasitics. Each parasitic incorporates a single drill hole. The drill holes can be filled or emptied of liquid metal. When a particular drill

hole is filled with liquid metal, a via is formed and the parasitic is said to be switched ON. Under this condition the associated parasitic element is connected to ground and acts as a reflector. When the drill hole is emptied, no via is formed and the parasitic is said to be switched OFF. Under this condition the associated parasitic acts as a director. With the aid of these reconfigurable vias it is possible to reconfigure the directions of the radiation patterns. The second approach involves the switchable ground plane. This is achieved by using liquid metal to form and reshape the ground plane. Specifically, whole segments of ground plane are added or removed by using liquid metal. Ground 1 and Ground 3 can be formed from liquid metal. This enables them to be added (switched ON) or removed (switched OFF) as required. Doing so influences the beam direction. In particular, the beam switches towards the direction from which the ground plane has been removed. Above Fig. 5. 7 shows that directional beams are obtained by altering the shape of the ground plane using liquid metal. To the best of my knowledge, this is the first antenna that is capable of reconfiguring its radiation pattern by reshaping the ground plane using liquid metal.

5.3.2 Antenna Fabrication

Fig. 5. 10 shows a photograph of the fabricated antenna. Fig. 5. 10 (c) shows the side view of assembled antenna for Design #1. This antenna incorporates a metallic reflector. The antenna was fabricated using Printed Circuit Board (PCB) fabrication techniques. A series of screws, located around the edge of the substrate, were used to secure the layer L_4 in position. The layer L_4 is required to prevent the liquid metal from leaking out. The reflector was formed from a piece of FR-4 substrate incorporating copper on the upper side. A series of spacers were used to set the correct separation between the antenna and reflector.

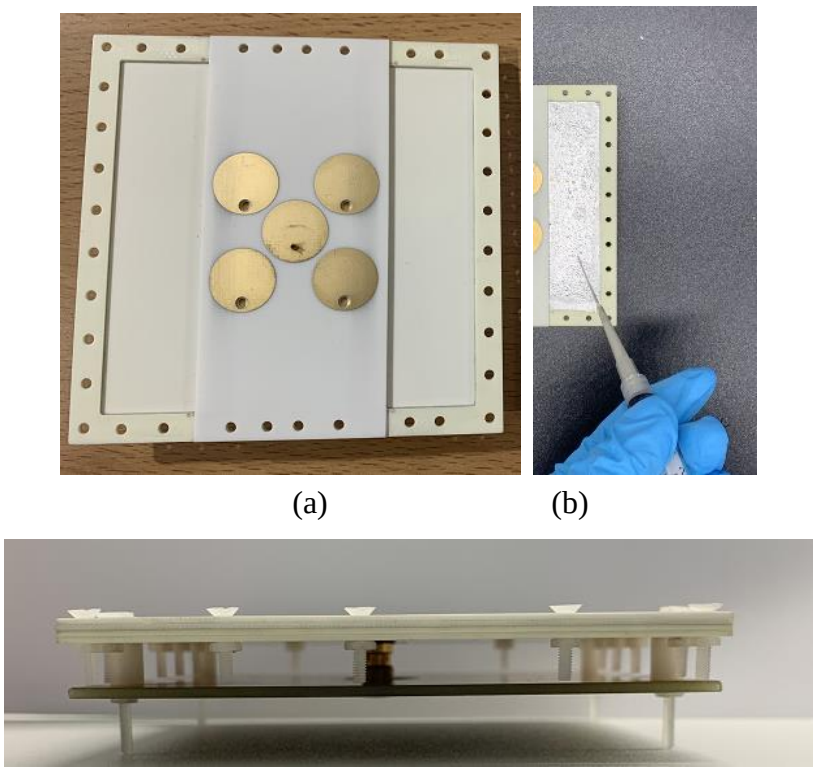

(a) (b)

(c)

Fig. 5. 10. Photographs of the fabricated antenna. (a) Top view without cover layer; (b) Ground drained by a syringe; (c) Side view of assembled antenna for Design #1.

5.3.3 Actuation and Removal of Liquid Metal

The liquid metal employed, for the work reported in this chapter, is based around an alloy consisting of 75% Gallium and 25% Indium. The conductivity of this liquid metal is 3.4×10^6 S/m. As discussed in Chapter 4, the liquid metal channels were fabricated by cutting slots into dielectric substrates. This approach is suitable for channels that do not have a complex 3D shape. The liquid metal was moved into (or withdraw out of) desired positions using a syringe. This technique is widely used in the literature within proof-of-concept designs [99], [103]. Fig. 5. 10 (b) shows the ground plane drained by a syringe. It is worth noting that due to the oxide film of liquid metal as discussed in Chapter 2, it is difficult for liquid metal to distribute evenly in an open area. In that case, a brush was also used to help evenly distribute the liquid metal in the open ground plane. This situation is improved by optimizing the channel design in Chapter 6.

Another important process is the removal of liquid metal from the channels, for the purpose of reconfiguring the antenna. Unfortunately, when liquid metal is removed from a channel it tends to leave a stain (known as a residual) on the inside surface of the channel. Here we list three methods that are widely used for removing the residuals of liquid metal. They are classified into mechanical, chemical, and electrochemical methods. For mechanical method, ethanol can be used as an eraser to remove thin liquid metal films. One has much freedom in using this method. However, it is difficult to make an eraser with small geometrical size thus difficult to remove liquid metal from the fine areas. For chemical method, alkalis and acids can be used to remove liquid metal. These chemical materials could react with the gallium oxide films or with liquid metal. To improve the safety of the experiment, the chemical materials used here are supposed to be nontoxic, environment friendly, and easy to remove. This method is efficient. However, some chemical materials may be corrosive to the channel materials, thus one has to choose suitable materials for channels. For electrochemical method, a specific voltage (e.g. 15 V) would be added to the target part to remove the liquid metal. This method allows people to control the direction of the liquid metal movement. However, the force generated is usually so weak that it can only be used to remove weakly liquid metal films.

In our experiments, we choose to employ a chemical method to remove residues of liquid metal from the inside surfaces of the channels. To this end we prepared a Sodium Hydroxide (NaOH) solution. The solution was prepared by dissolving 5 g of NaOH in 250 mL of water. We inject the NaOH solution into the channels to wash out the liquid metal. Following this we flushed the residues of NaOH solution out of the channels using water. However, one disadvantage of this approach is that the NaOH solution is corrosive to the channel materials that we used. For that reason, it was necessary to print copies of each channel and to replace failed channels, from time-to-time. Given

more time we would conduct further research to alleviate this disadvantage. The chemical equation for the reaction of NaOH with gallium oxides is as follows:

$$Ga_2O_3 + 2NaOH \rightarrow 2NaGaO_2 + H_2O \quad (5.2)$$

5.4 Simulation and measurement results Demonstrating Beam Switching

All of the simulated results presented in this section were obtained using CST Microwave Studio 2019. To verify the proposed designs, the hardware prototypes of the antennas were fabricated and measured. A vector network analyzer (Rohde & Schwarz ZNBT 8) was used for the measurement. The radiation patterns and the realized gains for the different operating states were measured using a far-field antenna test range.

5.4.1 Design #1 Performance

Fig. 5. 10 shows the prototype of Design #1 with a metallic reflector. Table 5. 4 shows different operating states of the antenna. The proposed antenna is symmetrical about the Y-axis, and it can provide five switchable beams in the XZ-plane. When all drill holes are empty and two ground segments are filled with liquid metal, a broadside beam is obtained. We term this known as State 1. When all drill holes are empty and one of ground segments is filled with liquid metal, a steered beam is obtained. We term those State 2 and State 3. When two drill holes and one ground segment on the same side are simultaneously filled with liquid metal, the antenna can obtain a beam directed at a larger angle. We term those State 4 and State 5.

Table 5. 4. States of Fluidic Channels and Radiation Patterns

State *i*	Via State				Ground State		Beam direction	Gain (dBi)	3-dB Beamwidth
	A	B	C	D	1	3			
1	Off	Off	Off	Off	On	On	0°	9.2	50.1°
2	Off	Off	Off	Off	Off	On	-20°	9.4	56.3°
3	Off	Off	Off	Off	On	Off	+20°		
4	On	Off	Off	On	Off	On	-40°	9.1	58.7°
5	Off	On	On	Off	On	Off	+40°		

Fig. 5. 11 depicts the simulated and measured reflection coefficients (S_{11}) associated with the States 1, 2 and 4. It is worth noting that we measured three different operating states, which yield beams directed towards 0°, -20°, and -40° in the XZ-plane. The structure is symmetrical along the Y-axis. For this reason, beams pointing towards other directions could be obtained by simply mirroring the states of vias along with the configuration of the ground plane. From Fig. 5. 11, it can be seen that the proposed antenna has a simulated -10 dB reflection coefficient bandwidth ranging from 5.5 GHz to 6 GHz. The discrepancies between the simulated and measured S_{11} are mainly caused by the offset of probe due to fabrication errors and assembly errors. The position of probe is not precise because we manually drill the feed hole of probe during the assembly process. In order to study the effect of the offset of the probe on reflection coefficients, we did a parametric study in simulation software. Specifically, Fig. 5. 12 shows the reflection coefficients of the designed antenna with different location of probe (*offset*). It can be seen that if the position of probe shifts from -3.6 m to -4 mm, the frequency of State 2 goes up and the -10 dB reflection coefficient bandwidth of State 4 gets narrower. These tendencies are the same as those observed in the measured results. Thus, we can conclude that errors in the probe offset is the reason for the

discrepancies observed in the measurements.

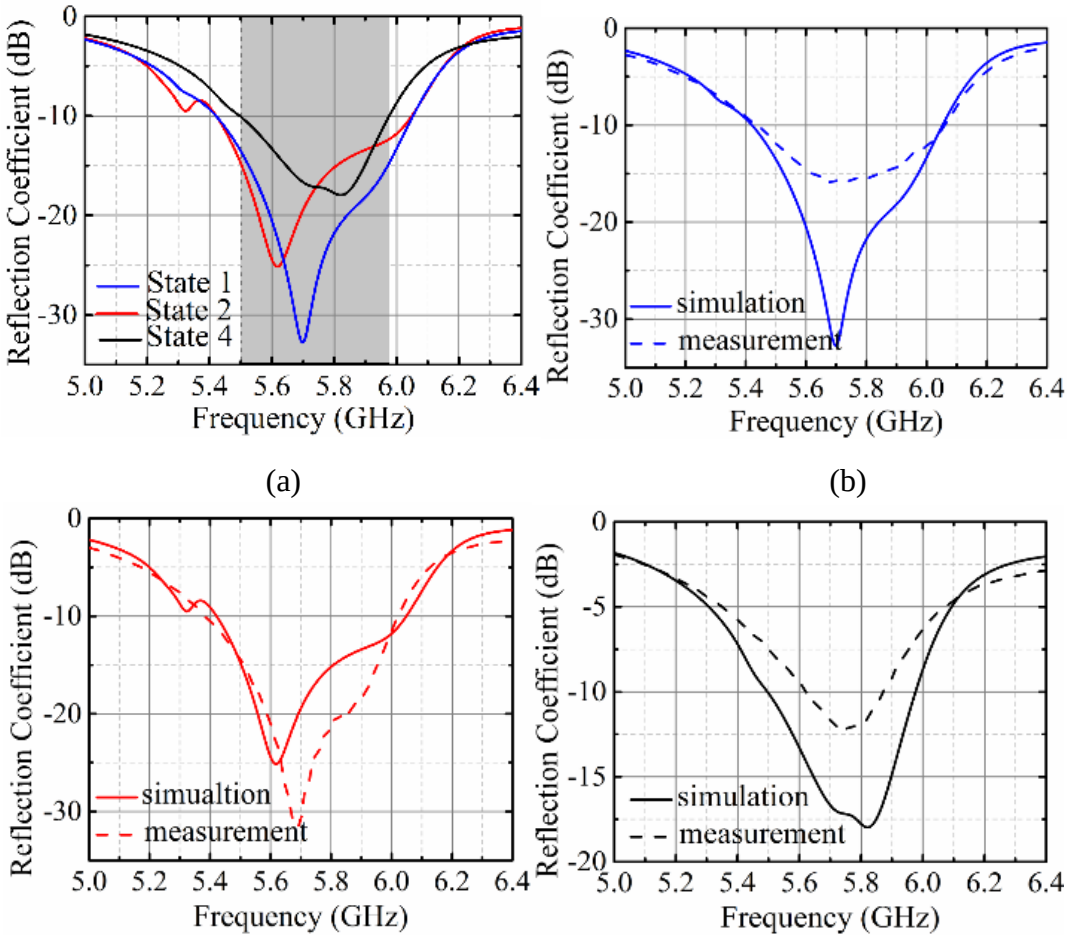

Fig. 5. 11. The reflection coefficient of the antenna as a function of frequency for different states. (a) Simulations for three states; Comparisons between simulation and measurement for (b) State 1, (c) State 2, and (d) State 4.

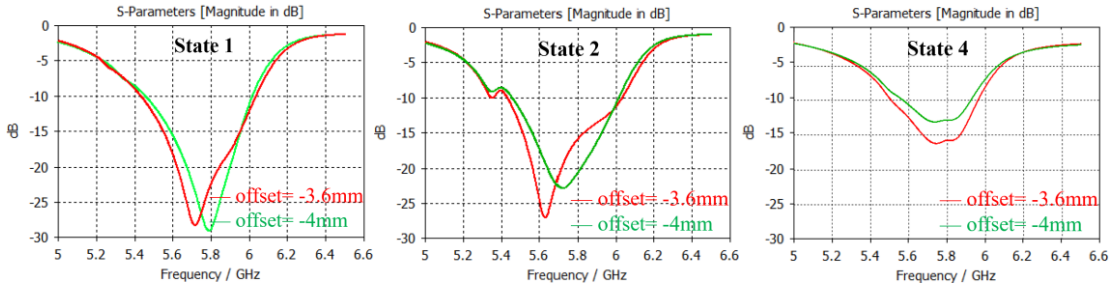

Fig. 5. 12. The reflection coefficients of the designed antenna with different offset of probe. (a) State 1; (b) State 2; (c) State 4.

The proposed antenna yields stable radiation performance at frequencies within the -10 dB reflection coefficient bandwidth. Fig. 5. 13 shows the simulated radiation patterns of the Design #1 for States 1, 2 and 4 at 5.9 GHz. Fig. 5. 14 shows fabricated antenna and the and the measured radiation patterns of the Design #1 for States 1, 2, and 4 at 5.9 GHz. From Fig. 5. 14, it can be seen that the proposed antenna is capable of switching its beams, in evenly distributed steps, by up to a maximum angle of ±40° whilst maintaining a Side Lobe Level (SLL) below -10 dB. It is clear that there is a good agreement between the measured and simulated results. Some discrepancies between the simulation and measurement results may be attributable to fabrication errors and assembly errors.

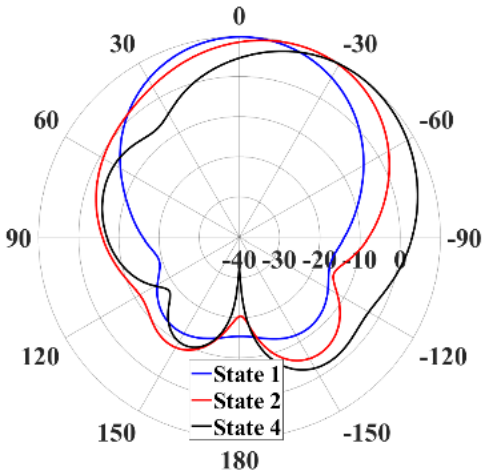

Fig. 5. 13. Simulated radiation patterns of the Design #1 working at 5.9 GHz.

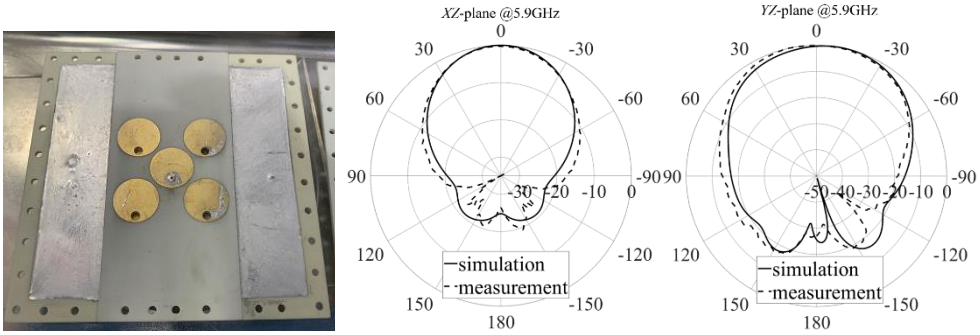

(a) (b) (c)

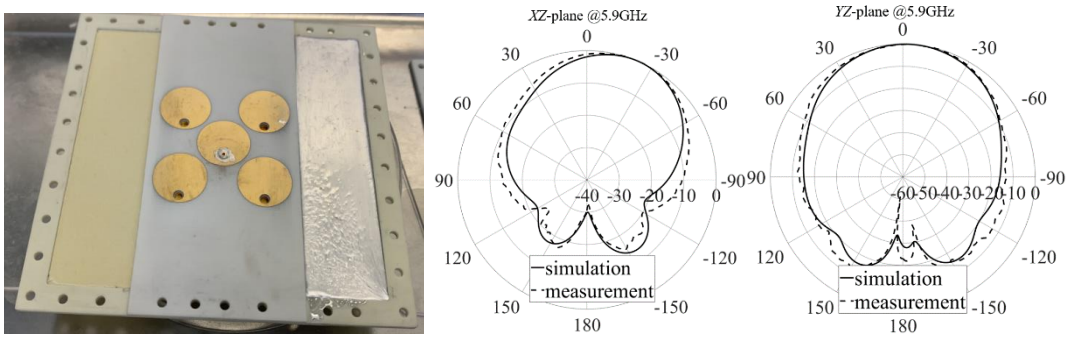

(d) (e) (f)

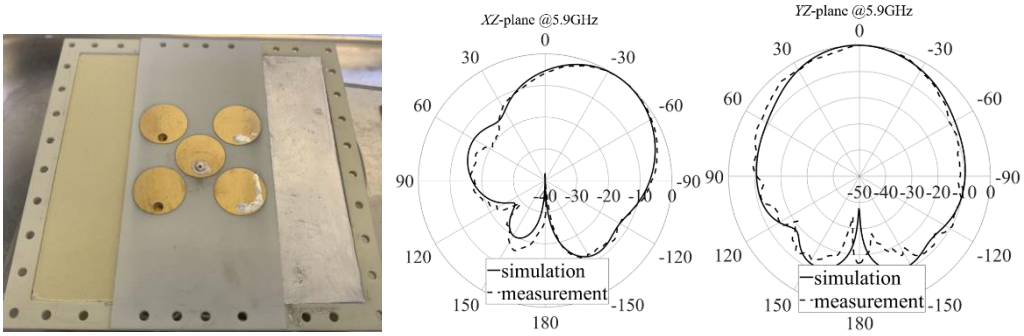

(g) (h) (i)

Fig. 5. 14. Fabricated antenna and the measured radiation patterns of the Design #1 working on (a), (b) and (c) State 1, (d), (e) and (f) State 2, and (g), (h) and (i) State 4. The measured radiation patterns are at 5.9 GHz. The first column shows States 1, 2, and 4; The second column shows the patterns on XZ-plane; The third column shows the patterns on YZ-plane.

Fig. 5. 15 shows the simulated gains and the measured gains for Design #1 associated with the different main beam directions. It can be seen that, the simulated gains for beams towards 0°, ±20°, and ±40° are 9, 9.4, and 9.1, respectively. The measured gains are less than 0.7 dB lower than the simulated results. The difference is due to the fabrication errors, assembly errors, and alignment of the measurement system. Besides, the difference between measured reflection coefficients and simulated ones also brings some errors in the reality. The measured scan loss is less than 0.5 dB across the beam scan angle range, which is the same as the simulations.

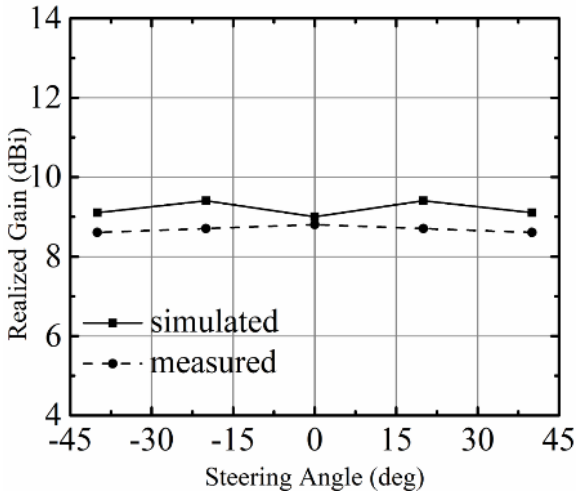

Fig. 5. 15. Simulated gains and measured gains versus steering angles at 5.9 GHz.

5.4.2 Design #2 Performance

Design #2 does not incorporate a metallic reflector. Table 5. 5 gives the operating states of Design #2 at 5.9 GHz and reports the performance. The proposed antenna is symmetrical about the Y-axis, and it can provide three switchable beams in the XZ-plane. When all drill holes are empty and two ground segments are filled with liquid metal, a broadside beam is obtained. We term this known as State 1. When two drill holes and one ground segment on the same side are simultaneously filled with liquid metal, the antenna can obtain a beam directed at a switchable angle. We term those State 2 and State 3. It is uncommon for a single antenna to be capable of steering beam to such a large angle. It is worth noting that we measured two different operating states, which yield beams directed towards 0° and -68° in the XZ-plane. The structure is symmetrical along the Y-axis. For this reason, beam pointing towards other direction could be obtained by simply mirroring the states of vias along with the configuration of the ground plane.

Table 5. 5. States of Fluidic Channels and Radiation Patterns (Design#2)

State *i*	Via State				Ground State		Beam direction	Gain (dBi)	3-dB Beamwidth
	A	B	C	D	1	3			
1	Off	Off	Off	Off	On	On	0°	9	51.4°
2	On	Off	Off	On	Off	On	-68°	7	125°
3	Off	On	On	Off	On	Off	+68°		

Fig. 5. 16 shows the reflection coefficient (S_{11}) of Design #2 for each of the two different operating states. Fig. 5. 17 shows the simulated and measured radiation patterns of Design #2 in two operating states shown in Table 5. 5. The measured and simulated radiation patterns are in good agreement. Fig. 5. 18 involves the simulated and measured realized gains for Design #1 and Design #2. These gain values were obtained at 5.9 GHz. The simulated gains of Design #2 are 9 dBi and 7 dBi for States 1 and 2, respectively. The measured gains are less than 0.8 dB lower than the simulated results. The reasons for the difference are the same as that for Design #1.

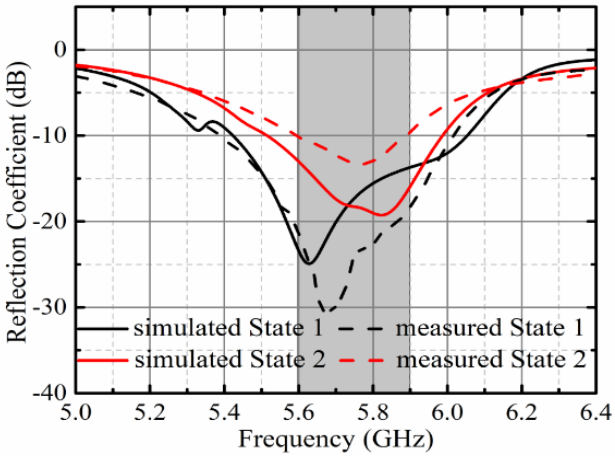

Fig. 5. 16. The reflection coefficient of Design #2 as a function of frequency for different states.

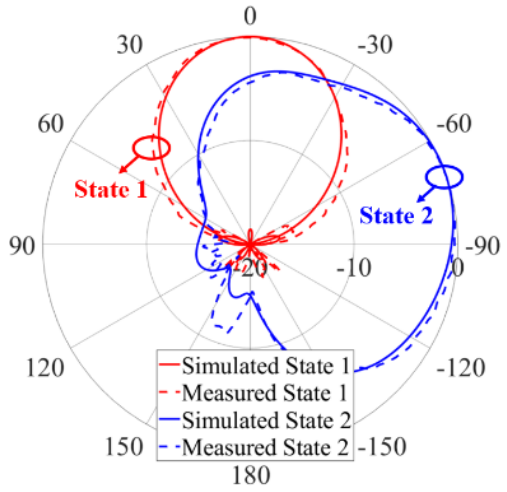

Fig. 5. 17. Simulated and measured radiation patterns of the Design #2 operating at 5.9 GHz in XZ-plane.

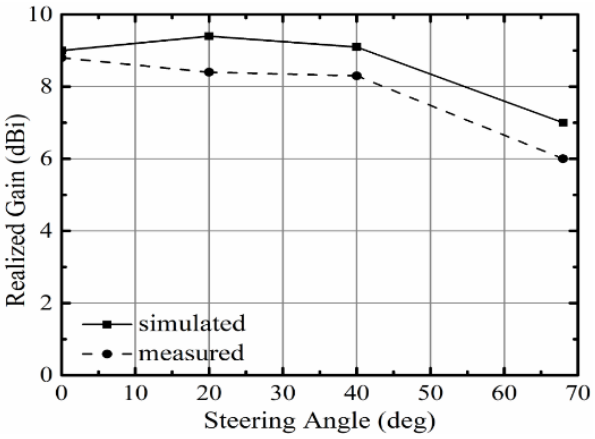

Fig. 5. 18. Simulated gains and measured gains versus steering angle of Design #1 and Design #2 at 5.9 GHz.

Table 5. 6 compares the performance of reconfigurable antennas reported previously in the literature against that of the antennas proposed in this chapter. It can be seen that the beam switching performances of the proposed antennas, including the scan angle and scan loss, are considerably improved. According to the simulated results, the proposed antennas provide radiation efficiencies, over the whole operating band and within all operating states, which are better than 90%. This efficiency value is higher than that of most of the pattern reconfigurable antennas reported in the literature. More

importantly, we propose a novel switchable ground plane technique, which is effective and valuable for future designs.

Table 5. 6. Comparison for Antenna Performance

Ref.	Frequency (GHz)	Scan angle	No. of beam	Scan loss (dB)	Radiation Efficiency	Control method
[75]	2.3	15°	5	2	>75%	PIN
[80]	2.45	±30°	3	1.6	Null	PIN
[95]	2.4	360°	4	0.5	83%	PIN
[97]	4.5	±54°	5	3.1	>90%	Liquid metal
[98]	2.4	±5°	5	0.7	>60%	Liquid metal
This Work	5.9 (Design #1)	±40°	5	0.5	>90%	Liquid metal
	5.9 (Design#2)	±68°	3	2	>90%	Liquid metal

Please note that the radiation efficiency is given by simulations in this chapter. Further measurement of radiation efficiency of antennas could be done in our future work. There are several methods of the measurement of radiation efficiency, including Wheeler Cap method, Full 3D-pattern measurement method, and Reverberation Chamber method. It is common to use the Wheeler Cap method to measure an antenna with small size. Using this method, people calculate the efficiency of the antenna by measuring the change in impedance of the antenna in free space. The full 3D-pattern measurement method is based on the radiation pattern of antennas. Using this method, people calculate the radiation efficiency by measuring the radiated power of the antenna at each point in space. A Reverberation Chamber is basically a shielded room with an arbitrarily shaped metallic rotating paddle. The paddle is designed to be non-symmetric and is used to create a continuously changing boundary condition of the electromagnetic fields, and rotating the paddle creates a statistical environment in a

Reverberation Chamber. In this environment, people calculate the radiation efficiency by comparing the transmission parameters of the reference antenna and the test antenna.

5.5 Considerations in Relation to Bandwidth, Mutual Coupling, and Actuation Rate of Liquid Metal.

Based on the above discussion, we know that the proposed antennas have good beam switching capability at 5.9 GHz. In this section, we will discuss some other related considerations. Specifically, we will discuss the performance of antenna over a band of frequencies, the effect of mutual coupling on patterns, as well as the rate at which liquid metal moves within a channel.

5.5.1 Consideration Related to Bandwidth

From above Fig. 5. 11 and Fig. 5. 16, it can be seen that both of the proposed antennas have a simulated -10 dB reflection coefficient bandwidth ranging from 5.5 GHz to 6 GHz. However, we mainly show the radiation performance of antennas at 5.9 GHz. Now let us investigate the performance of antennas over a band of frequencies.

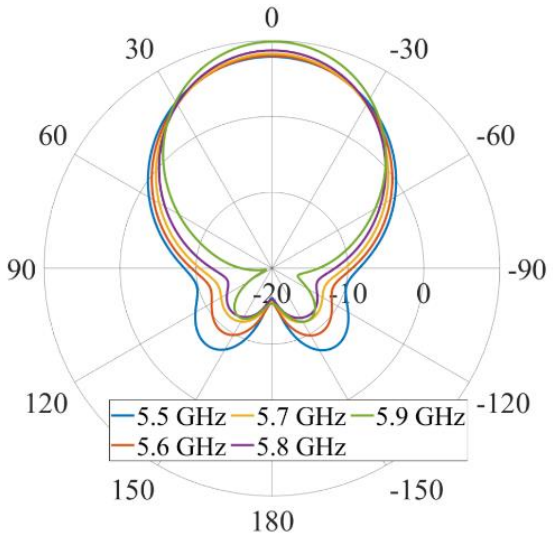

Fig. 5. 19. Simulated radiation patterns of Design #1-State1 at different frequencies in XZ-plane.

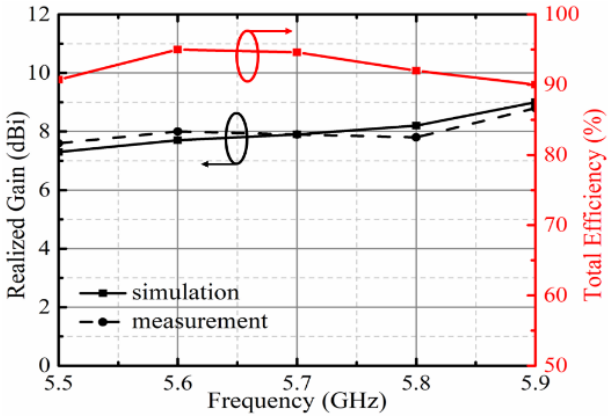

Fig. 5. 20. Realized gain and total efficiency of Design#1-State1 versus frequency.

Fig. 5. 19 shows simulated radiation patterns for Design #1 in state 1, at a range of different frequencies. Fig. 5. 20 shows the realized gain and the simulated radiation efficiency at the same set of frequencies. It can be seen that the radiation patterns as a function of frequency remain stable. Whilst the gain increases as the frequency increases. The highest gain value is obtained at 5.9 GHz. The measured gains agree well with the simulations. At some points, the measured gains are slightly higher than the simulated results. This is due to the calibration deviation of the standard horn. The antenna exhibits a similar tendency when operating in the other states. More

importantly, the gain fluctuates by more than 2 dB over the operating bandwidth. A similar value of gain fluctuation is also associated with other antennas reported in the literature [136], [137]. However, we see this as a limitation of the design. Additionally, this level of gain fluctuation is quite large compared with the level associated with a conventional patch antenna. In order to understand the cause of this gain fluctuation, we undertook some investigations within the simulation environment. Based on our simulations, the gain fluctuation is mainly attributable to two factors: 1) the presence of the dielectric cover (i.e. layer L_4); 2) the thickness of liquid metal channels. The discussion which follows explains our investigation process. First, to investigate the influence of layer L_4, we built a simple model similar to Design #1, as shown in Fig. 5. 9. However, the model did not incorporate a layer L_4 or channels within the ground plane. The entire ground plane was made of printed Copper. Such a simple patch antenna has a gain fluctuation of just 0.7 dB over the -10 dB reflection coefficient bandwidth. Then, we added the layer L_4, formed from RO4003c substrate and having a thickness of 0.813 mm. We found that the gain fluctuation over the bandwidth increases to 1.35 dB. It means that layer L_4 contributes another 0.65 dB to the overall gain fluctuation. To investigate the influence of the liquid metal channels, we modelled them in the simulation model. The results show that when the thickness of liquid metal channels is 0.813 mm, the gain fluctuation increases to 2.2 dB. In other words, the thickness of liquid metal channels contributes another 0.9 dB to the overall gain fluctuation. Further research could be undertaken to lower the gain fluctuation over the operating frequency band by reducing the thickness of layer L_4 as well as the thickness of the liquid metal channels.

5.5.2 Consideration of the Effect of Mutual Coupling on Patterns

A series of parameter studies has been conducted to shown how the mutual coupling

between driven patch and parasitics affects the radiation pattern of the proposed antenna. The studies are summarized in Fig. 5. 21, Fig. 5. 22, Fig. 5. 23. From Fig. 5. 21, it can be seen that increasing the distance between driven patch and parasitics increases the operating frequency of the structure. From Fig. 5. 22, it can be seen that increasing the distance between driven patch and parasitics has the effect of increasing the SLL of the structure. From Fig. 5. 23, it can be seen that increasing the distance between driven patch and parasitics increases steering angle of the structure. Thus, we can get a conclusion that for the proposed antenna, moving the parasitics closer to the driven patch creates higher mutual coupling which leads to a lower operating frequency, a lower SLL, and a smaller steering angle.

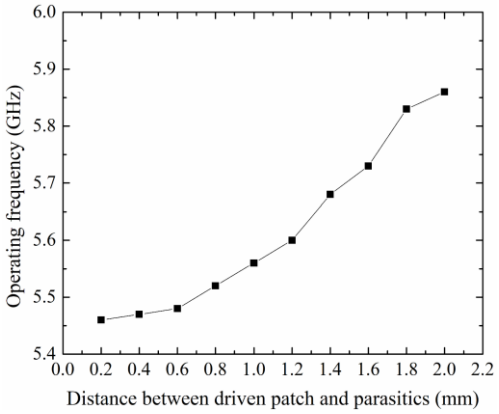

Fig. 5. 21. The relationship between the operating frequency and the distance between the driven patch and parasitics.

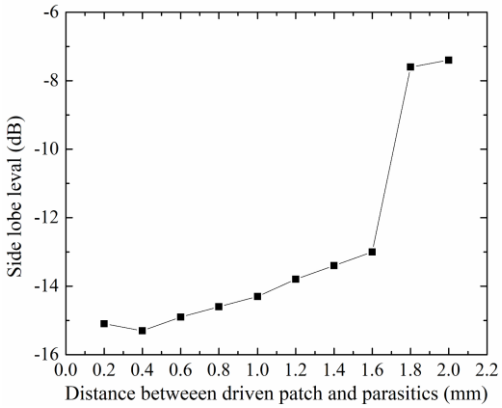

Fig. 5. 22. The relationship between the SLL and the distance between the driven patch and parasitics.

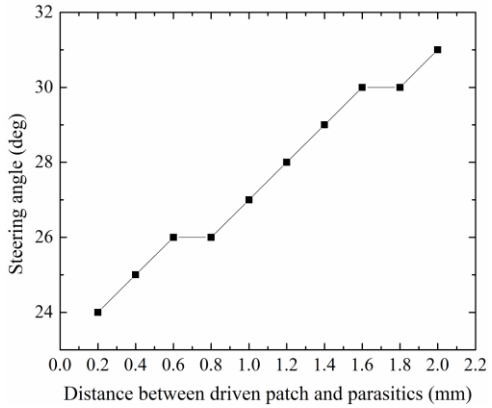

Fig. 5. 23. The relationship between the steering angle and the distance between the driven patch and parasitics.

5.5.3 Consideration of Actuation Rate of Liquid Metal

As shown in above Fig. 5. 10 (b), the liquid metal was currently moved into (or withdraw out of) desired positions using a syringe. This technique is widely used in the literature within proof-of-concept designs [103], [99]. However, in many applications, liquid metal could also be electronically controlled, as discussed in Section 4.3.3 of Chapter 4. The electrical technique has been shown capable of moving liquid metal at a rate of 30 cm/s [138]. In this case, it is likely for our design to take no more than 1.5 seconds to switch between two different states. Although the switching speed of liquid

metal may be not as fast as conventional electrical devices, it still could be used for some applications.

Forming narrow beams towards individual users, moving at high speed, would require fast switching. However, there are still many applications which do not require the fastest possible switching speeds. Two targeted applications are large intelligent surfaces (LIS) and user terminals for satellite internet. Specifically, LIS are employed to improve signal strength and link budget at mobile terminals. In this case, reconfiguration is occasionally needed when the environment changes. Generally, the factors which cause the environment to change do so slowly and include factors such as tree growth. Alternatively, LIS could be used to address coverage not-spots. To this end large intelligent surfaces may need to tilt a beam to expand or contract the coverage area. This could happen relatively slowly (<2 mins. for electrical beam tilting, at the base station, in 3G UMTS. For another application, Starlink, as a major contender for satellite internet. The antennas required for the ground station also do not require fast switching. It takes ~40s for a single Starlink satellite to cross the visible area of the sky above a user terminal. Typically, satellites are visible at a minimum elevation angle of 25°. The user terminal needs to steer a beam over a 130° angle range in 40s, which means the beam scanning rate is 3.25°/s. Thus, both require switching speeds ranging from milliseconds to seconds but require high gain and high efficiency.

5.6 Chapter Summary

This chapter presents two novel beam switchable antennas. The antennas are reconfigured using liquid metal and provide more than two states of radiation patterns. A novel switchable ground plane is employed in the designs. To the best of my knowledge, the antennas presented in this chapter are the first to employ a switchable ground plane reconfigured using liquid metal. The two antennas operate at 5.9 GHz,

they are capable of switching the main beam directions to a wide scan angle with low scan loss. Moreover, a reasonable -10 dB reflection coefficient bandwidth was obtained for all operating states. The simulated radiation efficiencies of the proposed antennas are better than 90% for all states. Compared with most of reconfigurable antennas using semiconductors reported earlier in the literature, the proposed antennas have improved performances on low scan loss, wide scan angle, and high radiation efficiency. The proposed antennas are attractive candidates for modern wireless communications.

Chapter 6 A Continuously Steerable Patch Antenna Employing Liquid Metal

Building on the designs proposed in Chapter 5, an improved antenna design is reported in this chapter. The improvement enables the antenna to achieve continuous beam steering. To this end we designed a liquid metal channel and fabricated it using a 3D printer. This chapter introduces in detail the effect of the choice of material and printing method on the antenna performance. With this improved channel, the updated patch antenna can provide continuous beam steering from -30° to +30°. This is the first microstrip patch antenna having the capability of continuous beam steering in the elevation plane.

6.1 Introduction

Beam steerable antennas are widely used in a range of emerging applications, including radar systems and satellite communications. They have the capability of enhancing communication security, improving channel capacity, and adapting to changing channel conditions [124] - [129]. A phased array antenna is a popular example of a beam steerable antenna [139] - [142]. A phased array antenna can achieve continuous beam steering. However, it requires phase shifters to control the phase, which are expensive and suffer from severe energy losses. Reflect-array or transmit-array antennas consist of many unit cells. Some reflect-array or transmit-array antennas can achieve continuous beam steering [143] - [148]. However, this increases the complexity of the structure. A microstrip patch antenna, is an example of a single-element antenna, that can be used as the basis for beam steerable antennas, due to its low cost, simple structure, and ease of fabrication [149] - [151]. However, in the existing literature on single-element antennas most of designs can only steer beams towards a discrete range

of different directions rather than provide continuous beam steering. [102] proposed a beam steerable patch antenna. It used parasitics as directors or reflectors. The movable parasitic director and reflector elements were implemented by liquid metal. The antenna is capable of performing fine resolution beam steering over a 360° range. However, it steers the beam in the azimuth plane. Only a few papers report microstrip patch antennas which can achieve continuous beam steering.

This chapter presents an improved version of the design, reported in Chapter 5. The design is capable of continuous beam steering. To this end we designed a liquid metal channel and fabricated it using a 3D printer. With this improved channel, the updated microstrip patch antenna can achieve a continuous beam steering up to ±30°. To the best of my knowledge, this is the first microstrip patch antenna having the capability of continuous beam steering in the elevation plane.

6.2 Antenna Design and Simulations

The antenna design presented herein is an improved version of the design reported in Chapter 5. So, the antenna configuration along with its parameters are presented directly at the beginning of this section. Then detailed analysis of the improved ground channel is given. Finally, some simulation and measurement results are given to validate the design and show its beam steering capacities.

6.2.1 Antenna Design

Fig. 6. 1 shows the geometry and parameters of the antenna. Table 6. 1 shows the parameters of the antenna. The antenna is constructed using four layers in total, namely h_1 to h_4. The first layer works as a cover and it is formed from a piece of Rogers RO4003c having a thickness of 0.813 mm, a permittivity of 3.55, and a loss tangent of

0.0027. The second layer works as the substrate of the patch antenna, and it is formed from a piece of Rogers RO4003c having a thickness of 1.524 mm. On the upper surface of this substrate layer, there is a driven patch surrounded by four parasitics. The driven patch and the parasitics are all circular in shape with the same diameters. Energy is fed into the antenna using a coaxial fed probe. The probe is offset along the y-axis by 4.9 mm in order to yield optimum impedance matching. Each parasitic incorporates a single drill hole which passes through this substrate layer. On the lower surface of this substrate, there is a rectangular ground plane named Ground 2. Ground 2 is formed from copper and remains permanently in place. The third layer was fabricated from Polylactic acid (PLA) using a 3D printer. It has a thickness of 6 mm, and a permittivity of 2.7. The third layer is located beneath the drill holes. The meandered channels are located in the middle of the third layer. The channel walls, located above and below the channel, are 2 mm thick, as shown in Fig. 6. 1 (c). When the channels are filled with liquid metal, they form Ground 1 and Ground 3. It is worth noting that Grounds 1 and 3 are not electrically connected to the Ground 2, they are actually floating conductors, but they have the same RF performance as connecting to Ground 2. It is because there are some overlapped places between Ground 1 and Ground 2 (or Ground 2 and Ground 3) as shown in Fig. 6.1 (a) and (c). This ensures that most of the energy could be reflected and only few of energy could leak from the gap, thus we still call these two floating conductors as “ground” here. The following section will show the comparison of channels connected and disconnected to the ground. Additionally, the third layer is employed as a cover to prevent the liquid metal from leaking out of the drill holes. A metallic reflector is placed behind the third layer, as shown in Fig. 6. 1 (c).

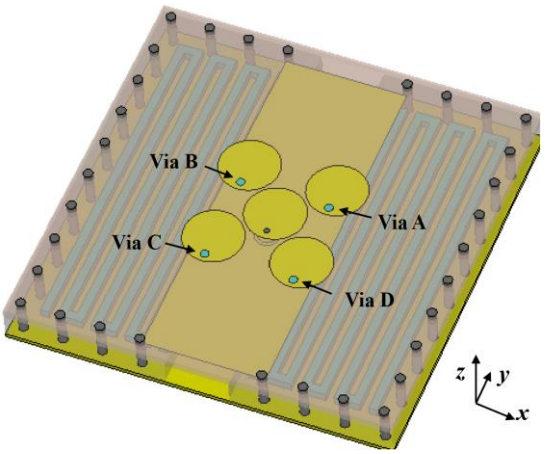

(a)

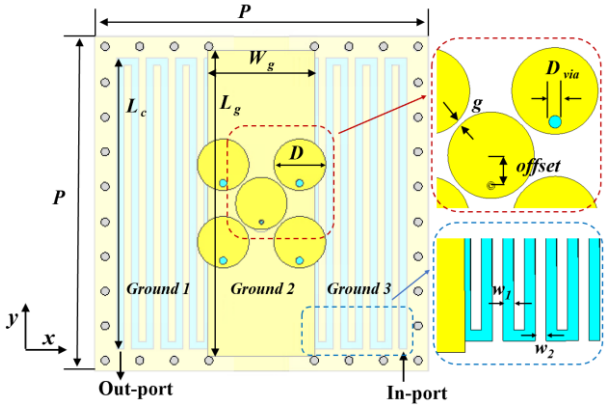

(b)

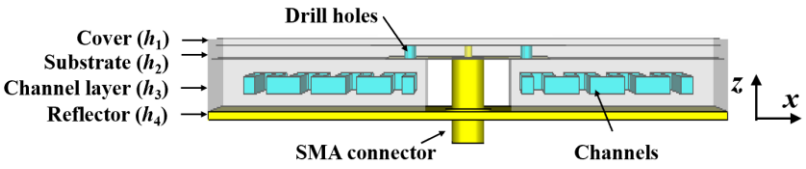

(c)

Fig. 6. 1. Geometry and parameters of the antenna. (a) Perspective view; (b) Top view; (c) Side view.

Table 6. 1. Optimized Dimensions of The Design #1 Antenna (Unit: MM)

P	L_g	L_c	W_g	D	D_{via}	g
91	83	79	29	7	2	0.7
offset	w_1	w_2	h_1	h_2	h_3	h_4

4.9	2	2	0.813	1.524	6	1

6.2.2 Metallic Ground Plane and Meandered Channel

The meandered channel designed for use within the proposed antenna has several advantages. Firstly, it enables continuous control of the main beam direction. Secondly, it can block waves polarised along the Y-axis. This is significant because the radiation from the patches is directed along the Y-axis. Specifically, Fig. 6. 2 shows the current distribution on the patches of the proposed antenna. It can be seen that electric field associated with the proposed antennas is polarised along Y-axis. We have examined and compared the performance of a solid metal ground plane with that of a meandered ground plane. Fig. 6. 3 (a) shows a solid metallic ground plane and Fig. 6. 3 (b) shows the meandered channel designed for use in the proposed antenna. Both structures were excited by waves polarised along the Y-axis. Fig. 6. 4 shows the reflection coefficient (S_{11}) associated with the solid metal ground plane and the proposed meandered channel. It can be seen that for waves polarised along Y-axis, most of the energy is reflected by the meandered channel and in fact the meandered channel behaves much the same as the solid ground plane. For this reason, when the channels are fully filled with liquid metal, we expect them to have the same reflective effect for the main polarization of wave associated with the patches, as a solid metallic ground plane.

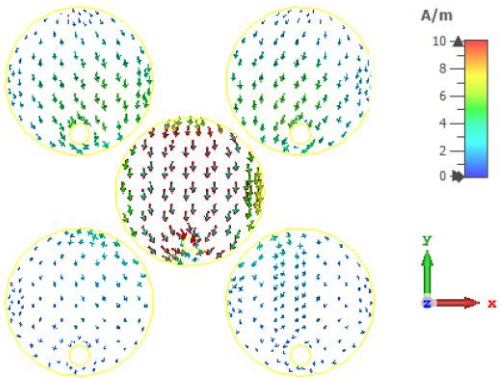

Fig. 6. 2. The current distribution on the patches of the designed antenna.

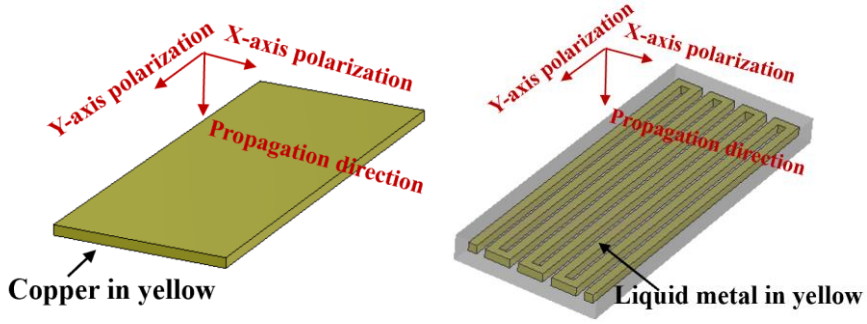

(a) (b)

Fig. 6. 3. Models of (a) a solid metallic ground plane and (b) the designed channel.

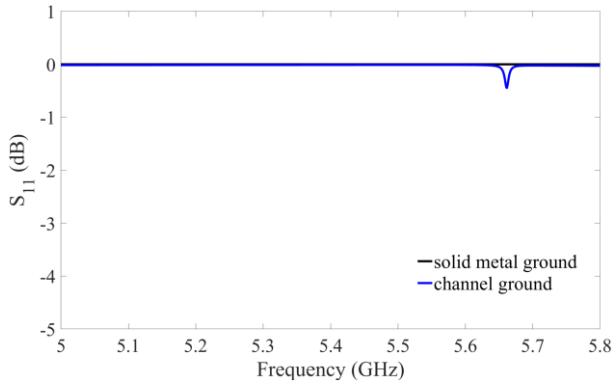

Fig. 6. 4. The reflection coefficients (S_{11}) of the designed channels and of a solid metallic ground plane for the waves polarised along Y-axis.

6.2.3 Beam Steering Capability

The proposed antenna employs two approaches in unison to steer the direction of the

main beam. Those approaches are the same as those used for the design reported in Chapter 5. However, it is worth noting that although the approaches applied in both Chapters are same, the design discussed in this chapter differs from the designs, discussed in Chapter 5, both in terms of the channel design and performance. Due to the improved channel design, presented in this chapter, it is possible to continuously vary the quantity of the liquid metal within the channel, and thus achieve continuous beam steering. To the best of my knowledge, this is the first microstrip patch antenna that is capable of continuously steering beam by reshaping the ground plane using liquid metal.

Table 6. 2. States of Fluidic Channels and Radiation Patterns

	Ground 1	**Ground 3**	**Beam direction**
All vias Off	Tuning	On	-10º to 0 º
All vias Off	On	Tuning	0º to +10º
Vias A and D On	Tuning	On	-30º to -10º
Vias B and C On	On	Tuning	+10º to +30º

Table 6. 2 shows the turning states of the antenna. When all drill holes are empty and whole ground plane is filled with liquid metal, a broadside beam is obtained. When all of the drill holes are empty and one of the ground plane channels is fully filled with liquid metal, then we can continuously tune the main beam direction by altering the length of the other ground plane channel. In this way it is possible to continuously steer the main beams by up to ±10°. When two of the drill holes and one ground plane channel on the same side are simultaneously filled with liquid metal, we can continuously tune the main beam direction by altering the length of the other ground plane channel. Under this condition it is possible to continuously steer the main beam direction by up to ±30°.

The simulation results presented in this section were obtained using CST Microwave Studio 2019. Fig. 6. 5 illustrates the beam steering capability of the antenna in the XZ-plane at 5.3 GHz. Fig. 6. 5 (b) shows a selection of beam directions, namely: 0°, ±10°, ±20°, and ±30°. However, the antenna is capable of continuously steering a beam up to a maximum angle of ±30°, as shown in Fig. 6. 5 (a). The simulated scan loss is 1.8 dB across the whole beam scan angle range. Fig. 6. 6 shows the simulated reflection coefficients (S_{11}) associated with the specific main beam directions, as shown in Fig. 6. 5 (b). It can be seen that the proposed antenna has a simulated -10 dB reflection coefficient bandwidth ranging from 5.3 GHz to 5.5 GHz.

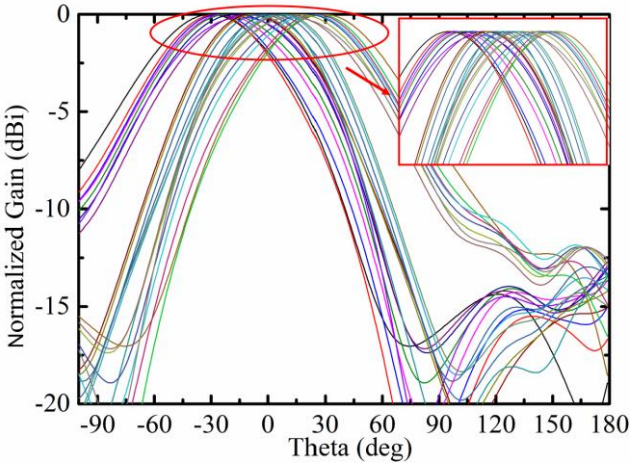

(a)

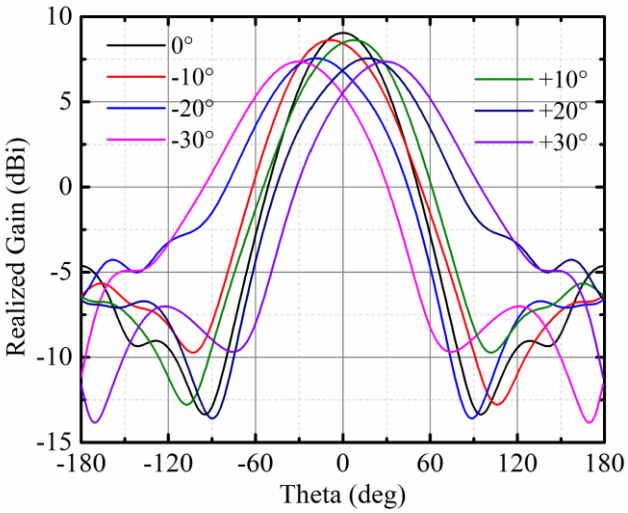

(b)

Fig. 6. 5. Simulated radiation pattern at 5.3 GHz in XZ-plane. (a) Continuous scanning; (b) several beams in XZ-plane.

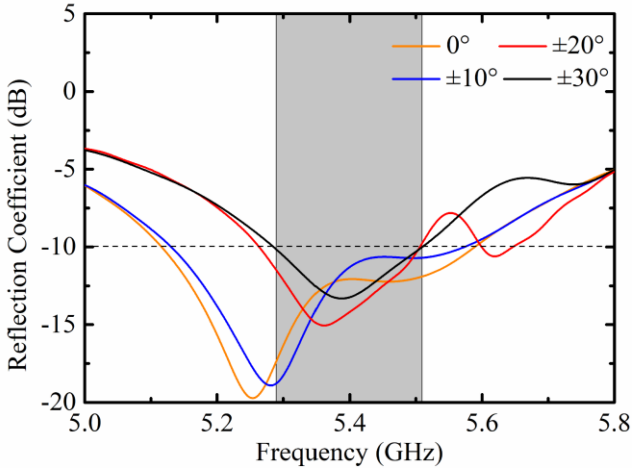

Fig. 6. 6. The reflection coefficients of the antenna as a function of frequency.

6.3 Antenna Fabrication and Measurement

6.3.1 3D Printing Channels

Fig. 6. 7 shows the photograph of the fabricated channels. Although the shape of the channel is not complicated, it is still difficult for traditional machining processes to fabricate such 3D structure in one piece. We chose to use a 3D printer to fabricate the channel. A 3D printer can easily fabricate complicated 3D objects. According to the specifications of the Ultimaker S3 3D printer, the finest feature that can be realized in the vertical direction is a 0.06 mm. The 3D printer has a fundamental resolution of 6.9 μm × 6.9 μm × 2.5 μm in x-, y-, and z-axes, respectively.

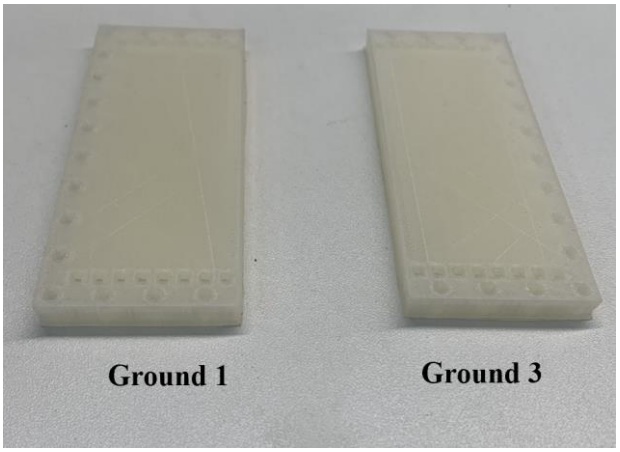

Fig. 6. 7. The photograph of the fabricated channel ground.

6.3.2 Effective Permittivity of Printed Object

The material used to print the channel is transparent Polylactic acid (PLA). Nominally PLA has a permittivity of 2.7 and a loss tangent of 0.017 [152]. However, it is possible to change the effective permittivity of the printed object by changing the settings of 3D printer. For example, we could change the effective permittivity of the printed object by altering the infill density. When an object is printed using a 3D printer it is built up, layer-by-layer, from strands of material which are laid down. There are air gaps between the strands. The infill density determines the ratio of air to PLA within the printed object. Fig. 6. 8 shows the view of two structures with the same shape but different infill densities.

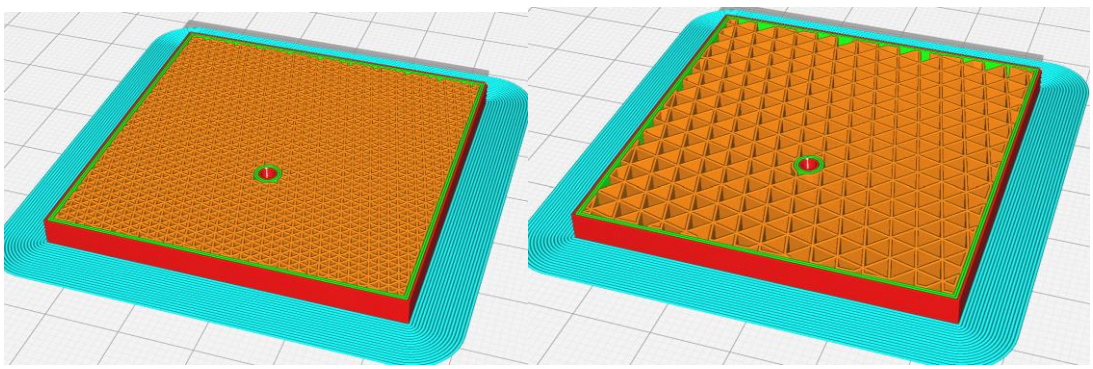

(a) (b)

Fig. 6. 8. The view of the same structure with different infill densities. (a) 100% infill density; (b) 40% infill density.

The following paragraph explains how we measured the effective permittivity of the PLA. There are several different methods that can be employed to measure the permittivity of solid material. These methods include: transmission line method, resonant cavity method, and other novel methods [153] - [157]. The antenna lab. within Queen Mary University of London (QMUL) has the necessary equipment for performing characterization via the free-space method. However, the chamber room used for free-space method in antenna lab. is designed for X-band frequencies, whilst we want to measure the material at around 5 GHz where the proposed antenna operates. For this reason, we chose to measure the effective permittivity of the printed object by using a resonant method. The particular method which we employed involved fabricating a simple microstrip patch antenna and comparing the measured result for that antenna with results obtained through full-wave computer simulations. The following sentences explain the specific measurement procedure. Two slabs of 3D printed material having different infill densities were used as the substrate for a microstrip patch antenna. To this end, the microstrip patch was formed from copper tape attached to the upper surface of the slab. The ground plane was also formed from copper tape. The patch was via fed. This was achieved by drilling a hole through the substrate, pushing the centre pin of an SMA connector through the hole, and soldering the pin to the patch. Fig. 6. 9 shows two measured patch antennas and their simulated and measured reflection coefficients (S_{11}). It can be seen that when the infill density goes down, the resonant frequency goes up which means that the effective permittivity of the printed layer is lower. Table 6. 3 shows the different effective permittivity values caused by different infill densities. Please note that there are only two samples because I wanted to verify that the effective permittivity of the printed object could be changed

by changing the infill density of printed slab. More work on measuring the permittivity of material has been finished by another PhD student in our group (Yihua Zhou). Her measured results agree with mine. Also, my results are broadly in line with those reported in the literature [152], [153]. For these reasons the results reported in Table 6. 3 are felt to be credible.

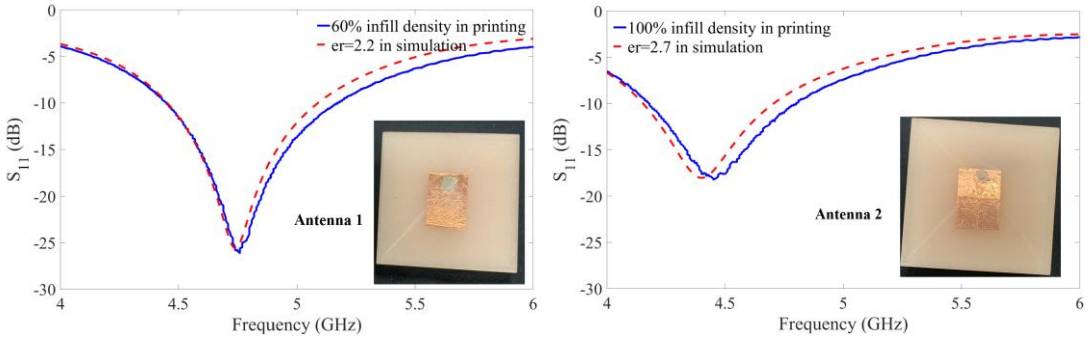

(a) (b)

Fig. 6. 9. Two measured patch antennas and their simulated and measured reflection coefficients. Patch antennas with (a) 60% infill density and (b) 100% infill density.

Table 6. 3. Measured Permittivity of Each Sample

Antenna	**Infill density (%)**	**Permittivity**
Antenna 1	60	2.2
Antenna 2	100	2.7

Based on some experimental verifications, the asymmetric Bruggeman (A-BG) effective equation explains the relationship between the effective permittivity and the printed object [158].

$$A\text{-}BG: \ \frac{\varepsilon_i - \varepsilon_{eff}}{\varepsilon_i - \varepsilon_h} = (1-p)\left(\frac{\varepsilon_{eff}}{\varepsilon_h}\right)^{1/3} \tag{6.1}$$

Where: ε_{eff} is the effective permittivity of the printed slab, ε_{i} is the permittivity of the

printing material, ε_h is the permittivity of the host material, p is the volume fraction of printing material. In our case, the printing material is transparent PLA material with the permittivity of 2.7, and the host material is air with the permittivity of 1. A lower infill density will lead to a lower volume fraction (p) of printing material. Consequently, the A-BG equation explains the general trend seen in the result, specifically that the effective permittivity is lower for a lower infill density of printing.

Based on the above discussion, it is known that it is possible to change the effective permittivity of the printed slab by altering the infill density. However, it is difficult for our design to change the effective permittivity by altering the infill density. The reasons for this are explained below. Fig. 6. 10 shows the views of two channels with different infill densities. It can be seen that for the designed meandered channels, the infill density of walls is always ~ 100% even if we use a different infill density. This is because the thickness of wall is too small to print air gaps between the strands. To the end, we set the infill density as 100% to print the channel.

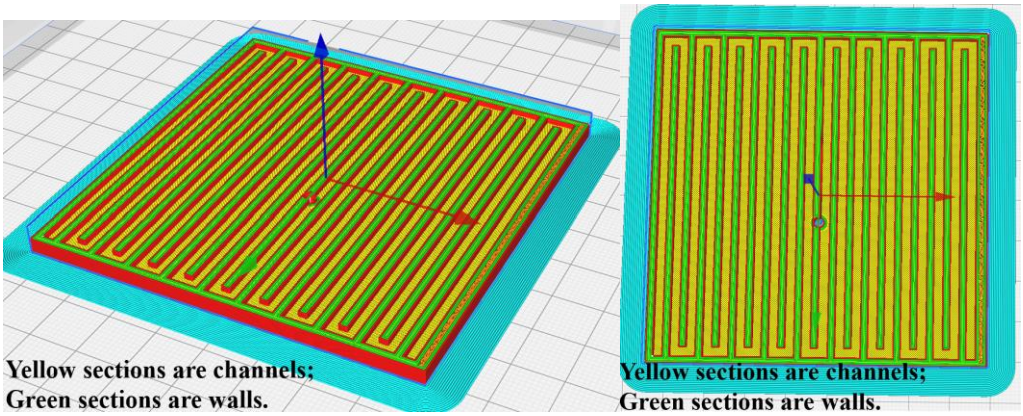

(a) (b)

Fig. 6. 10. The views of channels with different infill densities. (a) 100% infill density; (b) 60% infill density. However, there is basically no difference in actual printing objects.

6.3.3 Fabricated Antenna

This section presents the fabrication of the hardware prototype and the actuation of liquid metal. Fig. 6. 11 shows the fabricated prototype.

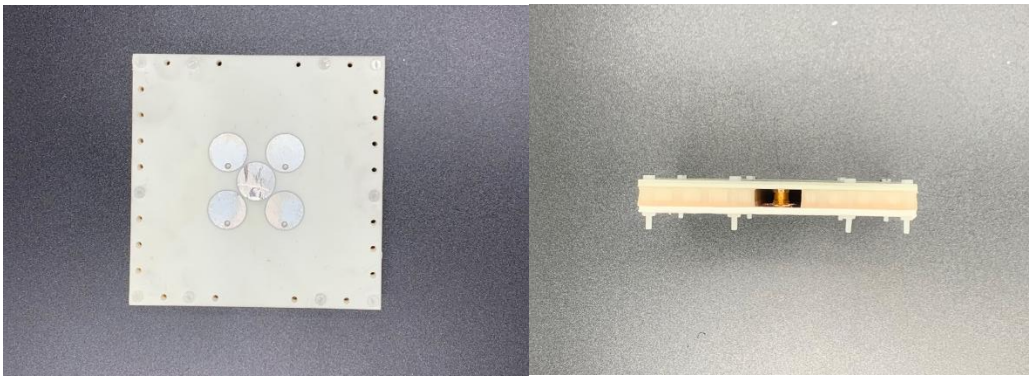

(a) (b)

Fig. 6. 11. The photograph of the fabricated prototype. (a) Top view; (b) side view.

The drill holes in the parasitics are used to contain and guide liquid metal. Effectively, therefore the drill holes form liquid metal channels. In order to ensure a good connection to the ground after injecting liquid metal, a channel design is used. Fig. 6. 12 shows the details of the channel design. The following text explains the fabrication procedure of these channels. Firstly, drill a through hole with a small diameter and plate it. This ensures that the plating within this small hole is connected to the ground plane. Secondly, drill a large hole from the top, which has only half of the depth of the previous one. Do not plate the later hole. As a result, the whole drill hole does not connect with the ground plane when there is no liquid metal. However, when we fill the hole with liquid metal it connects with the ground plane.

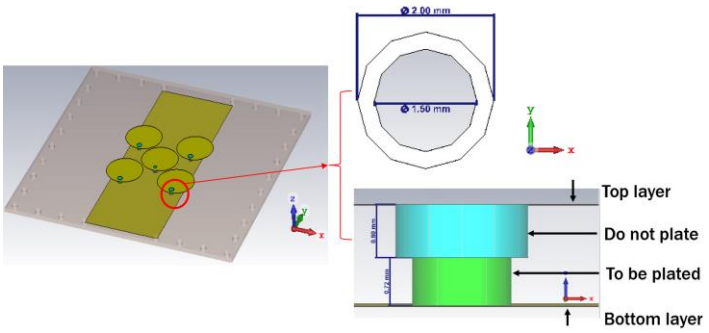

Fig. 6. 12. The fabrication of the drill holes.

(a) The designed meandered channel enables continuous control of the main beam direction. However, during the measurement, when liquid metal is injected into only part of the channel., i.e. the channel is not fully filled, the position of liquid metal in the channel may alter. The reason for this is that the antenna may be accidentally shaken during the measurement. To solve this problem, we simplify the channel to be some straight ones so that we can measure several typical states where only part of the channel is filled with liquid metal. (b)

(b) Fig. 6. 13 (a) shows a simplified structure for the ground in which straight channels are employed. (b)

(c) Fig. 6. 13 (b) shows the comparison of straight channels connected to the ground and meandered channels disconnected to the ground. As shown in (b)

(d) Fig. 6. 13 (b), there is almost no influence on RF performance of channels connected or disconnected to the ground. So, the design shown in (b)

Fig. 6. 13 (a) has the same RF performance as the original design shown in Fig. 6.1 and can fix the liquid metal into the required places. The reflector is put beneath the channels and serves as a cover which prevents the liquid metal from leaking out.

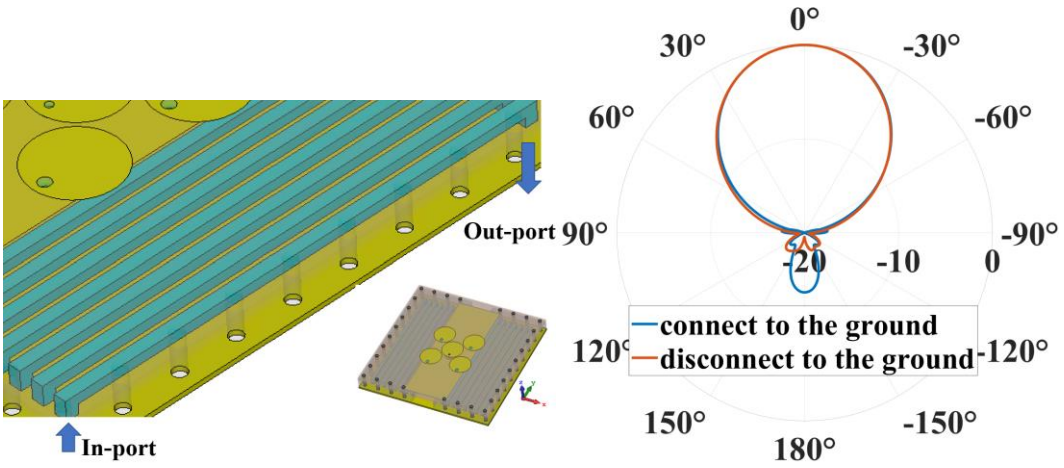

(e) (b)

Fig. 6. 13. (a) The simplified straight channels without liquid metal (in blue); (b) Comparison of straight channels connected to the ground and meandered channels disconnected to the ground.

A series of screws, located around the edge of the substrate, were used to fix the antenna and align the substrates, shown in Fig. 6. 9. The liquid metal employed here is based around an alloy consisting of 75% Gallium and 25% Indium. The conductivity of this liquid metal is 3.4×10^6 S/m. The liquid metal was moved into (or withdraw out of) desired positions using a syringe. This technique is widely used in the literature within proof-of-concept designs [159] - [167]. Fig. 6. 14 shows the actuation of the liquid metal. In this work, altering the method of actuation would have minimal effect on the RF performance of the proposed antenna because the actuation components would be located beneath the metallic reflector, where the electric and magnetic field strengths are minimal. Consequently, for this application, it is possible to control the liquid metal using a micropump [102] or electrochemically controlled capillary action [167]. Please note that liquid metal actuation is not within the scope of the work reported in this chapter. We focus solely on the beam steering technique and antenna design. However, based on the published literature, the electrical technique has been shown capable of moving liquid metal at a rate of 30 cm/s [138]. In our design, the overall length of the meandered channel for one ground (Ground 1 or Ground 3) is 66 cm. In this case, it

should be possible to fully fill the ground channel within 2.2 s, and thus the reconfiguration time for our design is expected to range from milliseconds to seconds. Although the switching speed of liquid metal may be slower than conventional electrical devices such as PIN diodes, it still could be used for some applications, such as airport radar and user terminals for satellite internet. Both require switching speeds ranging from milliseconds to seconds but require high power-handling capability and low loss.

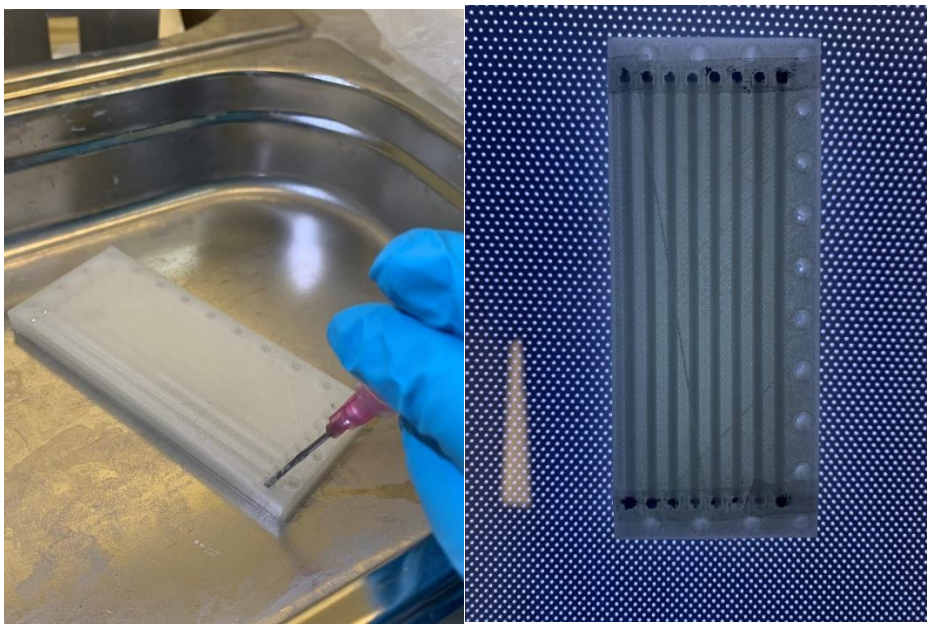

(a) (b)

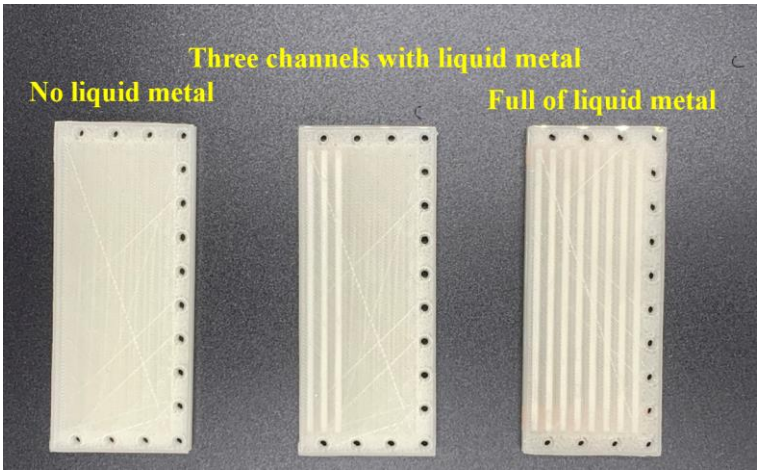

(c)

Fig. 6. 14. Actuation of the liquid metal. (a) Channels drained by a syringe; (b) Channels fully filled with liquid metal; (c) Channels with liquid metal in different states.

6.3.4 Measurement Results

A vector network analyzer (Rohde & Schwarz ZNBT 8) was used for the measurement. The radiation pattern and the realized gain for the different operating states were measured using a far-field antenna test range.

Fig. 6. 15 illustrates the simulation and measurement results associated with a selection of beam directions, namely: 0°, -10°, -20°, and -30° in the XZ-plane. It is worth noting that the structure is symmetrical along the Y-axis, and the beams pointing towards +X-axis direction could be obtained by simply mirroring the states of vias along with the configuration of the ground plane. The figures in the left column show the reflection coefficients (S_{11}), and the figures in the right column show the normalized radiation patterns. The measured results, for all states, agree well with the simulations. From inspection of Fig. 6. 15 (b), (d), (f) and (h), it is clear that the proposed antenna is capable of steering its beams up to a maximum angle of ±30° whilst maintaining a Side Lobe Level (SLL) below -10 dB.

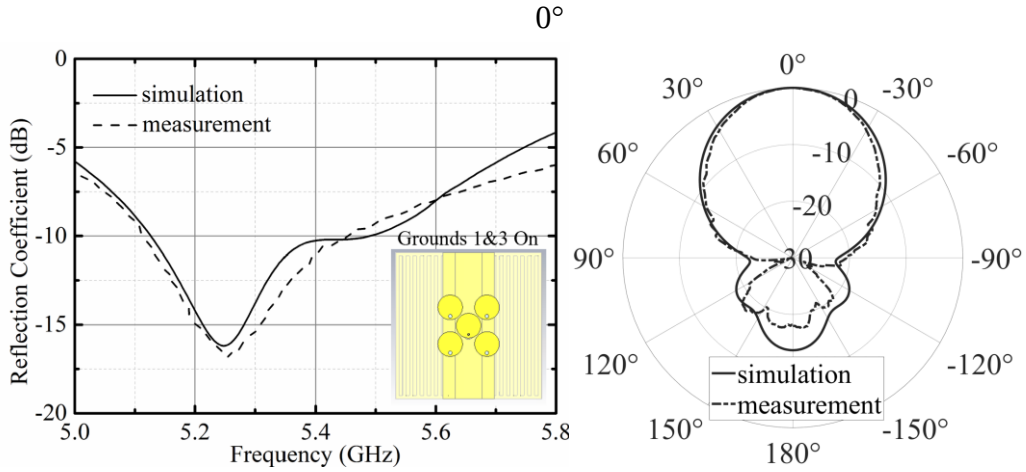

(a) (b)

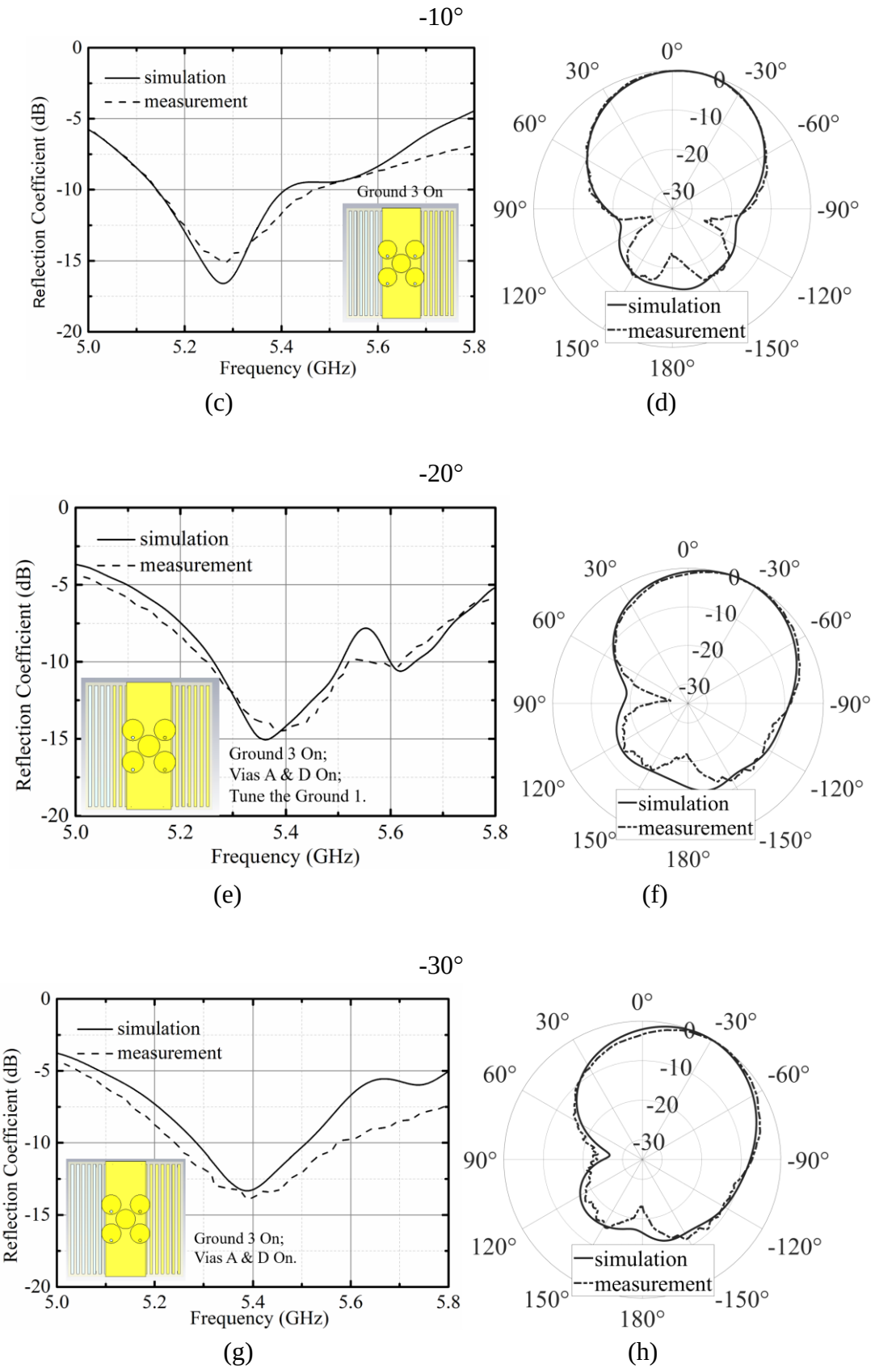

Fig. 6. 15. Simulation and measurement results associated with four beams directed towards 0°, -

10°, -20°, and -30° in the XZ-plane at 5.3 GHz. Figures (a), (c), (e), and (g) show the reflection coefficients of the antenna, figures (b), (d), (f), and (h) show the radiation patterns.

Fig. 6. 16 shows the simulated gains and the measured gains. Fig. 6. 16 (a) shows the gains associated with the different beam angles. It can be seen that, the measured gains at 5.3 GHz for main beam directions towards 0°, -10°, -20°, and -30° are 7.9 dBi, 8.1 dBi, 7 dBi, and 6.7 dBi, respectively. The maximum difference between measured gains and simulated gains is 1 dB. The difference between the simulation and measurement results may be attributable to fabrication errors, assembly errors, and the alignment of the measurement system. The measured scan loss is 1.4 dB across the whole beam scan angle range. Fig. 6. 16 (b) shows the gains of broadside beam over a range of different frequencies. The difference between measured gains and simulated gains are all smaller than 1 dB at different frequencies. Table 6. 4 compares the performance of single-element antennas reported previously in the literature against that of the antenna presented in this chapter. Please note that [102] illustrates beam steering in the horizontal plane whilst our work provides beam steering in the vertical plane which is totally different.

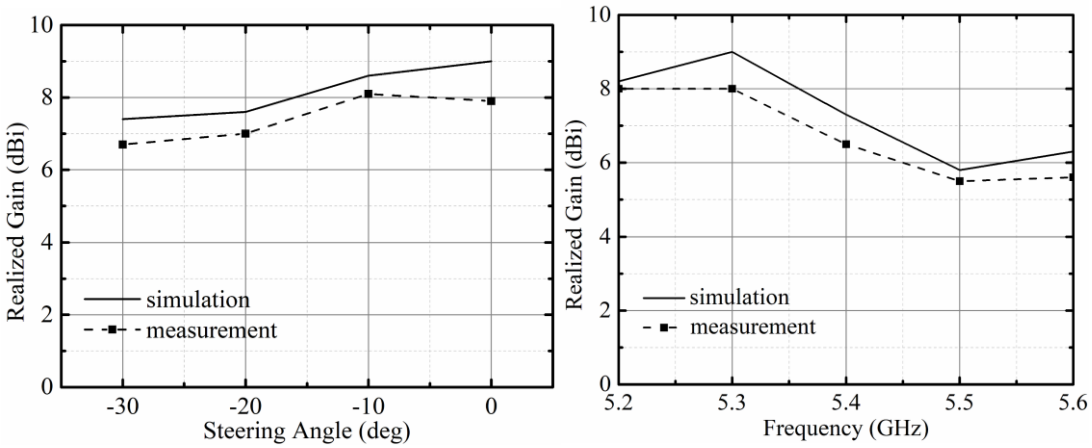

(a) (b)

Fig. 6. 16. Simulated gains and measured gains (a) versus scanning angles. (b) Simulated gains and measured gains of broadside beam versus frequencies.

Table 6. 4. Comparison for Antenna Performance

Ref.	Freq./ Bandwidth (GHz/MHz)	Gain (dBi)	Steer angle	No. of beam	Scan loss (dB)	SLL (dB)	Control
[75]	2.3/40(1.7%)	8.2	15°	5	2	15	PIN
[80]	2.45/60(2.4%)	7.2	±30°	3	1.6	9	PIN
[95]	2.4/150(6.2%)	6.1	360°	4	0.5	\	PIN
[97]	4.5/500(11%)	8.5	±54°	5	3.1	8	LM
[102]	1.8/70(3.8%)	< 3	360°	continuous	0.5	3	LM
Our work	5.3/200(3.8%)	8.1	±30°	continuous	1.4	12	LM

6.4 Conclusions

This chapter presents a continuously beam-steerable patch antenna using liquid metal. A tunable ground plane is employed in the design. Specifically, the designed meandered channel enables continuous control of liquid metal, which makes it possible for antenna to provide continuous beam steering. To the best of my knowledge, this is the first time that liquid metal has been used for a patch antenna to achieve continuous beam steering. The antenna operates at a center frequency of 5.3 GHz. The antenna was fabricated and measured. It can steer its main beam direction to a maximum angle of ±30° with 1.8 dB of scan loss. The proposed antenna is an attractive candidate for modern wireless communications.

Chapter 7 Conclusion and Future Work

In this chapter, we conclude the thesis first. Then we discuss the drawbacks of previous designs and provide some possible solutions to those drawbacks that could be developed in future work.

7.1 Conclusion

In this thesis, beam steerable antennas are proposed for the wireless communication systems, such as satellites, space exploration, and WIFI systems. The features targeted for the antennas proposed in this thesis are low cost, high efficiency, wide scan angle, and low scan loss. The course of this thesis has followed two aspects of actions: reconfigurable array unit cells employing liquid metal for beam steering applications, and reconfigurable microstrip patch antennas employing liquid metal for beam steering applications.

First, a theoretical calculation which establishes the performance limits for multi-layer transmit-array unit cells, is proposed in Chapter 3. It is the first study to be applicable to unit cells in which the metallic resonators, on the different layers, are shaped differently. A methodology for analyzing the limits of transmission amplitude of multi-layer transmit-array unit cells is also proposed. The results calculated from the proposed theory are then verified by computer simulations. The proposed theory aims to give a theoretical introduction for future designs. The proposed theory is then extended to a reconfigurable transmit-array unit cell employing liquid metal in Chapter 4. Compared with other reconfigurable unit cells, the proposed unit cell achieves a large phase shifting range with fewer conducting layers and lower insertion loss. The unit cell was measured within an open-ended waveguide. The characterization of liquid metal and the fabrication process of channels were discussed in Chapter 4.

In the section part (Chapters 5 and 6), beam steerable microstrip patch antennas are proposed. Chapter 5 presents two beam switchable patch antennas employing liquid metal. An equation which can be roughly approximate the operating frequency of the antenna is given at the beginning. Then the switchable ground plane as a novel technique is proposed. This is the first time that switchable beams are achieved by reshaping the ground plane employing liquid metal. The proposed two patch antennas have good performance on large scan angle and low scan loss. The fabrication of antenna and the actuation of liquid metal are discussed in Chapter 5. The antenna design reported in Chapter 6 is an improved version of the design reported in Chapter 5. The improvement enables antenna to achieve continuous beam steering. This is the first time that liquid metal has been used for a patch antenna to achieve continuous beam steering in elevation plane. Additive manufacturing technique, i.e. 3D printing, is utilized in Chapter 6.

All the designs in this thesis are related to the theme of beam steering employing liquid metal. The proposed antennas, including transmit-array unit cell and microstrip patch antennas, are promising candidates for wireless communication applications.

7.2 Future Work

The potential future work which can be conducted based on the work that has been presented in this thesis is summarized and not limited to the following.

1 We focus on the reconfigurable unit cells instead of the whole array in the thesis. The performance of the whole transmit-array could be built, simulated, and measured in the future.

2 The actuation of liquid metal in real situation is very important. This could be implemented by using a micropump or electrochemically controlled capillary. We discuss these actuating solutions in Chapter 4. A realistic complete control system needs to be completed in future work.

3 The switching speed of reconfigurable antennas employing liquid metal is always a concern. This could be improved in future work by optimizing the design of liquid metal channel and the development of the actuation technology.

4 As discussed in Chapter 5, when we use NaOH solution to clean the liquid metal within the channels, the channels printed with transparent PLA material will be corroded. This could be improved by using another material like glass.

5 The radiation efficiencies of designed antennas are given by simulations in the thesis. As discussed in Chapter 5, the measurement of radiation efficiencies could be included in the future.

6 The proposed designs operate at frequencies below 10 GHz. Liquid metal can be very attractive at high mm-wave frequency bands, where PIN diodes have very high loss or even cannot work well. In future work, attempts could be made to design antennas employing liquid metal in high frequency bands.

References

[1]. X. Wu, G. Eleftheriades, and T. van Deventer-Perkins, “Design and characterization of single- and multiple-beam mm-wave circularly polarized substrate lens antennas for wireless communications,” *IEEE Trans. Microw. Theory Techn.*, vol. 49, no. 3, pp. 431–441, Mar. 2001.

[2]. G. Godi, R. Sauleau, and D. Thouroude, “Performance of reduced size substrate lens antennas for Millimeter-wave communications,” *IEEE Trans. Antennas Propag.*, vol. 53, no. 4, pp. 1278–1286, Apr. 2005.

[3]. J. R. Costa, C. A. Fernandes, G. Godi, R. Sauleau, L. Le Coq, and H. Legay, “Compact Ka-band lens antennas for LEO satellites,” *IEEE Trans. Antennas Propag.*, vol. 56, no. 5, pp. 1251–1258, May 2008.

[4]. Artemenko, A. Mozharovskiy, S. Tikhonov, A. Myskov, and R. Maslennikov, “Multiple-feed integrated lens antenna with continuous scanning range,” *Proc. 11th Eur. Conf. Antennas Propag. (EUCAP)*, Mar. 2017, pp. 2795–2799.

[5]. D. Filipovic, S. Gearhart, and G. Rebeiz, “Double-slot antennas on extended hemispherical and elliptical silicon dielectric lenses,” *IEEE Trans. Microw. Theory Techn.*, vol. 41, no. 10, pp. 1738–1749, Oct. 1993.

[6]. C. A. Fernandes, E. B. Lima, and J. R. Costa, “Broadband integrated lens for illuminating reflector antenna with constant aperture efficiency,” *IEEE Trans. Antennas Propag.*, vol. 58, no. 12, pp. 3805–3813, Dec. 2010.

[7]. S. Raman, N. Barker, and G. Rebeiz, “A W-band dielectric-lens-based integrated monopulse radar receiver,” *IEEE Trans. Microw. Theory Techn.*, vol. 46, no. 12,

pp. 2308–2316, Jun. 1998.

[8]. N. T. Nguyen, R. Sauleau, M. Ettorre, and L. Le Coq, “Focal array fed dielectric lenses: an attractive solution for beam reconfiguration at millimeter waves,” *IEEE Trans. Antennas Propag.*, vol. 59, no. 6, pp. 2152–2159, Jun. 2011.

[9]. G. -B. Wu, S. -W. Qu and S. Yang, “Wide-Angle Beam-Scanning Reflectarray with Mechanical Steering,” *IEEE Trans. Antennas Propag.*, vol. 66, no. 1, pp. 172-181, Jan. 2018.

[10]. C. Mateo-Segura, A. Dyke, H. Dyke, S. Haq and Y. Hao, “Flat Luneburg Lens via Transformation Optics for Directive Antenna Applications,” *IEEE Trans. Antennas Propag.*, vol. 62, no. 4, pp. 1945-1953, April 2014.

[11]. M. A. Al-Joumayly and N. Behdad, “Wideband planar microwave lenses using sub-wavelength spatial phase shifters,” *IEEE Trans. Antennas Propag*., vol. 59, no. 12, pp. 4542–4552, Dec. 2011.

[12]. N. Gagnon and A. Petosa, “Using rotatable planar phase shifting surfaces to steer a high-gain beam,” *IEEE Trans. Antennas Propag.*, vol. 61, no. 6, pp. 3086–3092, Jun. 2013.

[13]. H. Yi, S. -W. Qu, K. -B. Ng, C. H. Chan and X. Bai, “3-D Printed Millimeter-Wave and Terahertz Lenses with Fixed and Frequency Scanned Beam,” *IEEE Trans. Antennas Propag.*, vol. 64, no. 2, pp. 442-449, Feb. 2016.

[14]. E. D. Cullens, L. Ranzani, K. J. Vanhille, E. N. Grossman, N. Ehsan, and Z. Popovic, “Micro-fabricated 130–180 GHz frequency scanning waveguide arrays,” *IEEE Trans. Antennas Propag.*, vol. 60, no. 8, pp. 3647–3653, Aug. 2012.

[15]. A. Stehle et al., “Rf-mems switch and phase shifter optimized for wband,” *Proc. 38th Eur.Microw. Conf. (EuMC)*, Oct. 2008, pp. 104–107.

[16]. S. Mueller, F. Goelden, P. Scheele, M. Wittek, C. Hock, and R. Jakoby, “Passive phase shifter for w-band applications using liquid crystals,” *Proc. 36th Eur. Microw. Conf. (EuMC)*, pp. 306–309, Sep. 2006.

[17]. M. Frank, F. Lurz, R. Weigel and A. Koelpin, “Electronically Reconfigurable 6 × 6 Element Transmitarray at K-Band Based on Unit Cells with Continuous Phase Range,” *IEEE Trans. Antennas Propag.*, vol. 18, no. 4, pp. 796-800, April 2019.

[18]. C. Huang, W. Pan, X. Ma, B. Zhao, J. Cui, and X. Luo, “Using reconfigurable transmitarray to achieve beam-steering and polarization manipulation applications,” *IEEE Trans. Antennas Propag.*, vol. 63, no. 11, pp. 4801–4810, Nov. 2015.

[19]. J. G. Nicholls and S. V. Hum, “Full-space electronic beam-steering transmitarraywith integrated leaky-wave feed,” *IEEE Trans. Antennas Propag*., vol. 64, no. 8, pp. 3410–3422, Aug. 2016.

[20]. F. Wu, J. Wang, K. -M. Luk and W. Hong, “A Wideband Low-Profile Efficiency-Improved Transmitarray Antenna with Over-1-bit Phase-Shifting Elements,” *IEEE Access*, vol. 8, pp. 32163-32169, 2020.

[21]. A. Artemenko, A. Mozharovskiy, A. Maltsev, R. Maslennikov, A. Sevastyanov and V. Ssorin, “Experimental Characterization of E-Band Two-Dimensional Electronically Beam-Steerable Integrated Lens Antennas,” *IEEE Antennas Wireless Propag. Lett.*, vol. 12, pp. 1188-1191, 2013.

[22]. M. Sazegar et al., “Beam Steering Transmitarray Using Tunable Frequency Selective Surface with Integrated Ferroelectric Varactors,” *IEEE Trans. Antennas Propag.*, vol. 60, no. 12, pp. 5690-5699, Dec. 2012.

[23]. L. Zhao, M. Li, C. Liu, S. V. Hanly, I. B. Collings and P. A. Whiting, “Energy Efficient Hybrid Beamforming for Multi-User Millimeter Wave Communication with Low-Resolution A/D at Transceivers,” *IEEE Journal on Selected Areas in Communications*, vol. 38, no. 9, pp. 2142-2155, Sept. 2020.

[24]. J. Du, W. Xu, H. Shen, X. Dong and C. Zhao, “Hybrid Precoding Architecture for Massive Multiuser MIMO With Dissipation: Sub-Connected or Fully Connected Structures?,” *IEEE Trans. Wireless Commun.*, vol. 17, no. 8, pp. 5465-5479, Aug. 2018.

[25]. J. Zhang, W. Liu, C. Gu, S. S. Gao and Q. Luo, “Multi-Beam Multiplexing Design for Arbitrary Directions Based on the Interleaved Subarray Architecture,” *IEEE Transactions on Vehicular Technology*, vol. 69, no. 10, pp. 11220-11232, Oct. 2020.

[26]. A. F. Molisch, M. Z. Win, Yang-Seok Choi and J. H. Winters, “Capacity of MIMO systems with antenna selection,” *IEEE Trans. Wireless Commun.*, vol. 4, no. 4, pp. 1759-1772, July 2005.

[27]. Y. Gao, H. Vinck and T. Kaiser, “Massive MIMO antenna selection: switching architectures, capacity bounds, and optimal antenna selection algorithms,” *IEEE Trans. Signal Process.*, vol. 66, no. 5, pp. 1346-1360, Mar., 2018.

[28]. A. Dua, K. Medepalli and A. J. Paulraj, “Receive antenna selection in MIMO systems using convex optimization,” *IEEE Trans. Wireless Commun.*, vol. 5, no.

9, pp. 2353-2357, Sept. 2006.

[29]. E. G. Erker, A. S. Nagra, Yu Liu, P. Periaswamy, T. R. Taylor, J. Speck, and R. A. York. “Monolithic ka-band phase shifter using voltage tunable basrtio3 parallel plate capacitors,” *IEEE Microwave and Guided Wave Letters*, 10(1):10–12, Jan 2000.

[30]. D. Kuylenstierna, A. Vorobiev, P. Linner, and S. Gevorgian. “Composite right/left handed transmission line phase shifter using ferroelectric varactors,” *IEEE Microwave and Wireless Components Letters*, 16(4):167–169, April 2006.

[31]. T. A. Lam, D. C. Vier, J. A. Nielsen, C. G. Parazzoli and M. H. Tanielian, “Steering Phased Array Antenna Beams to the Horizon Using a Buckyball NIM Lens,” *Proceedings of the IEEE*, vol. 99, no. 10, pp. 1755-1767, Oct. 2011.

[32]. A. Abbaspour-Tamijani, L. Zhang, G. Pan, H. K. Pan and H. Alavi, “Lens-enhanced phased array antenna system for high directivity beam-steering,” *2011 IEEE International Symposium on Antennas and Propagation (APSURSI)*, 2011, pp. 3275-3278.

[33]. P. -Y. Feng, S. -W. Qu, S. Yang, L. Shen and J. Zhao, “Ku-Band Transmitarrays With Improved Feed Mechanism,” *IEEE Trans. Antennas Propag.*, vol. 66, no. 6, pp. 2883-2891, June 2018.

[34]. P. -Y. Feng, S. -W. Qu and S. Yang, “Phased Transmitarray Antennas for 1-D Beam Scanning,” *IEEE Antennas Wireless Propag. Lett.*, vol. 18, no. 2, pp. 358-362, Feb. 2019.

[35]. A. Abbaspour-Tamijani, L. Zhang, H. K. Pan, “Enhancing the Directivity of

Phased Array Antennas Using Lens-Arrays [J],” *Progress in Electromagnetics Research M*, 2013, 29: 41-64.

[36]. H. Kawahara, H. Deguchi, M. Tsuji, et al, “Design of rotational dielectric dome with linear array feed for wide‐angle multibeam antenna applications[J],” *Electronics and Communications in Japan (Part II: Electronics)*, vol. 90, no. 5, pp. 49-57, 2007.

[37]. H. Kamoda, T. Iwasaki, J. Tsumochi, T. Kuki and O. Hashimoto, “60-GHz Electronically Reconfigurable Large Reflectarray Using Single-Bit Phase Shifters,” *IEEE Trans. Antennas Propag*., vol. 59, no. 7, pp. 2524-2531, July 2011.

[38]. H. Yang et al., “A 1-Bit 10 × 10 Reconfigurable Reflectarray Antenna: Design, Optimization, and Experiment,” *IEEE Trans. Antennas Propag*., vol. 64, no. 6, pp. 2246-2254, June 2016.

[39]. H. Yang, F. Yang, S. Xu, M. Li, X. Cao and J. Gao, “A 1-Bit Multipolarization Reflectarray Element for Reconfigurable Large-Aperture Antennas,” *IEEE Antennas Wireless Propag. Lett.*, vol. 16, pp. 581-584, 2017.

[40]. H. Zhang, X. Chen, Z. Wang, Y. Ge and J. Pu, “A 1-Bit Electronically Reconfigurable Reflectarray Antenna in X Band,” *IEEE Access*, vol. 7, pp. 66567-66575, 2019.

[41]. X. Pan, F. Yang, S. Xu and M. Li, “A 10 240-Element Reconfigurable Reflectarray with Fast Steerable Monopulse Patterns,” *IEEE Trans. Antennas Propag*., vol. 69, no. 1, pp. 173-181, Jan. 2021, doi: 10.1109/TAP.2020.3008623.

[42]. J. Han, L. Li, G. Liu, Z. Wu and Y. Shi, “A Wideband 1-bit 12 × 12

Reconfigurable Beam-Scanning Reflectarray: Design, Fabrication, and Measurement," *IEEE Antennas Wireless Propag. Lett.*, vol. 18, no. 6, pp. 1268-1272, June 2019.

[43]. J. -B. Gros, V. Popov, M. A. Odit, V. Lenets and G. Lerosey, "A Reconfigurable Intelligent Surface at mmWave Based on a Binary Phase Tunable Metasurface," *IEEE Open Journal of the Communications Society*, vol. 2, pp. 1055-1064, 2021.

[44]. F. Wu, R. Lu, J. Wang, Z. H. Jiang, W. Hong and K. -M. Luk, "A Circularly Polarized 1 Bit Electronically Reconfigurable Reflectarray Based on Electromagnetic Element Rotation," *IEEE Trans. Antennas Propag*., vol. 69, no. 9, pp. 5585-5595, Sept. 2021.

[45]. B. Xi, Y. Xiao, K. Zhu, Y. Liu, H. Sun and Z. Chen, "1-Bit Wideband Reconfigurable Reflectarray Design in Ku-Band," *IEEE Access*, vol. 10, pp. 4340-4348, 2022.

[46]. O. Bayraktar, O. A. Civi and T. Akin, "Beam Switching Reflectarray Monolithically Integrated With RF MEMS Switches," *IEEE Trans. Antennas Propag*., vol. 60, no. 2, pp. 854-862, Feb. 2012.

[47]. H. Luyen, J. H. Booske and N. Behdad, "2-Bit Phase Quantization Using Mixed Polarization-Rotation/Non-Polarization- Rotation Reflection Modes for Beam-Steerable Reflectarrays," *IEEE Trans. Antennas Propag*., vol. 68, no. 12, pp. 7937-7946, Dec. 2020.

[48]. H. Luyen, Z. Zhang, J. H. Booske and N. Behdad, "Wideband, Beam-Steerable Reflectarrays Based on Minimum-Switch Topology, Polarization-Rotating Unit

Cells," *IEEE Access*, vol. 7, pp. 36568-36578, 2019.

[49]. W. Zhang, Y. Li and Z. Zhang, "A Reconfigurable Reflectarray Antenna With an 8 μm-Thick Layer of Liquid Crystal," *IEEE Trans. Antennas Propag*., vol. 70, no. 4, pp. 2770-2778, April 2022.

[50]. J. Yang et al., "Fully Electronically Phase Modulation of Millimeter-Wave via Comb Electrodes and Liquid Crystal," *IEEE Trans. Antennas Propag*., vol. 20, no. 3, pp. 342-345, March 2021.

[51]. X. Meng, M. Nekovee and D. Wu, "The Design and Analysis of Electronically Reconfigurable Liquid Crystal-Based Reflectarray Metasurface for 6G Beamforming, Beamsteering, and Beamsplitting," *IEEE Access*, vol. 9, pp. 155564-155575, 2021.

[52]. T. H. Hand and S. A. Cummer, "Reconfigurable Reflectarray Using Addressable Metamaterials," *IEEE Antennas Wireless Propag. Lett.*, vol. 9, pp. 70-74, 2010.

[53]. X. Yang et al., "A Broadband High-Efficiency Reconfigurable Reflectarray Antenna Using Mechanically Rotational Elements," *IEEE Trans. Antennas Propag*., vol. 65, no. 8, pp. 3959-3966, Aug. 2017.

[54]. X. Yang et al., "A Mechanically Reconfigurable Reflectarray With Slotted Patches of Tunable Height," *IEEE Antennas Wireless Propag. Lett.*, vol. 17, no. 4, pp. 555-558, April 2018.

[55]. P. Mei, S. Zhang and G. F. Pedersen, "A Wideband 3-D Printed Reflectarray Antenna With Mechanically Reconfigurable Polarization," *IEEE Antennas*

Wireless Propag. Lett., vol. 19, no. 10, pp. 1798-1802, Oct. 2020.

[56]. P. Mei, S. Zhang and G. F. Pedersen, "A Low-Cost, High-Efficiency and Full-Metal Reflectarray Antenna with Mechanically 2-D Beam-Steerable Capabilities for 5G Applications," *IEEE Trans. Antennas Propag*., vol. 68, no. 10, pp. 6997-7006, Oct. 2020.

[57]. L. Di Palma, A. Clemente, L. Dussopt, R. Sauleau, P. Potier and P. Pouliguen, "1-Bit Reconfigurable Unit Cell for Ka-Band Transmitarrays," *IEEE Antennas Wireless Propag. Lett.*, vol. 15, pp. 560-563, 2016.

[58]. W. Li, Y. Wang, S. Sun and X. Shi, "An FSS-Backed Reflection/Transmission Reconfigurable Array Antenna," *IEEE Access*, vol. 8, pp. 23904-23911, 2020.

[59]. F. Diaby, A. Clemente, R. Sauleau, K. T. Pham and L. Dussopt, "2 Bit Reconfigurable Unit-Cell and Electronically Steerable Transmitarray at Ka -Band," *IEEE Trans. Antennas Propag*., vol. 68, no. 6, pp. 5003-5008, June 2020.

[60]. Y. Wang, S. Xu, F. Yang and M. Li, "A Novel 1 Bit Wide-Angle Beam Scanning Reconfigurable Transmitarray Antenna Using an Equivalent Magnetic Dipole Element," *IEEE Trans. Antennas Propag*., vol. 68, no. 7, pp. 5691-5695, July 2020.

[61]. L. Di Palma, A. Clemente, L. Dussopt, R. Sauleau, P. Potier and P. Pouliguen, "Circularly-Polarized Reconfigurable Transmitarray in Ka-Band with Beam Scanning and Polarization Switching Capabilities," *IEEE Trans. Antennas Propag*., vol. 65, no. 2, pp. 529-540, Feb. 2017.

[62]. M. Wang, S. Xu, F. Yang and M. Li, "Design and Measurement of a 1-bit

Reconfigurable Transmitarray with Subwavelength H-Shaped Coupling Slot Elements," *IEEE Trans. Antennas Propag.*, vol. 67, no. 5, pp. 3500-3504, May 2019.

[63]. Y. Xiao, B. Xi, M. Xiang, F. Yang and Z. Chen, "1-Bit Wideband Reconfigurable Transmitarray Unit Cell Based on PIN Diodes in Ku-Band," *IEEE Antennas Wireless Propag. Lett.*, vol. 20, no. 10, pp. 1908-1912, Oct. 2021

[64]. J. Tang, S. Xu, F. Yang and M. Li, "Design and Measurement of a Reconfigurable Transmitarray Antenna With Compact Varactor-Based Phase Shifters," *IEEE Antennas Wireless Propag. Lett.*, vol. 20, no. 10, pp. 1998-2002, Oct. 2021.

[65]. J. Y. Lau and S. V. Hum, "A Wideband Reconfigurable Transmitarray Element," *IEEE Trans. Antennas Propag.*, vol. 60, no. 3, pp. 1303-1311, March 2012.

[66]. W. Pan, C. Huang, X. Ma and X. Luo, "An Amplifying Tunable Transmitarray Element," *IEEE Antennas Wireless Propag. Lett.*, vol. 13, pp. 702-705, 2014.

[67]. J. R. Reis, R. F. S. Caldeirinha, A. Hammoudeh and N. Copner, "Electronically Reconfigurable FSS-Inspired Transmitarray for 2-D Beamsteering," *IEEE Trans. Antennas Propag.*, vol. 65, no. 9, pp. 4880-4885, Sept. 2017.

[68]. J. Y. Lau and S. V. Hum, "Analysis and Characterization of a Multipole Reconfigurable Transmitarray Element," *IEEE Trans. Antennas Propag.*, vol. 59, no. 1, pp. 70-79, Jan. 2011.

[69]. M. Frank, F. Lurz, R. Weigel and A. Koelpin, "Electronically Reconfigurable

6 × 6 Element Transmitarray at K-Band Based on Unit Cells with Continuous Phase Range," *IEEE Antennas Wireless Propag. Lett.*, vol. 18, no. 4, pp. 796-800, April 2019.

[70]. P. Mei, S. Zhang and G. F. Pedersen, "A Low-Profile and Beam-Steerable Transmitarray Antenna: Design, Fabrication, and Measurement [Antenna Applications Corner]," *IEEE Antennas and Propagation Magazine*, vol. 63, no. 5, pp. 88-101, Oct. 2021.

[71]. E. Erdil, K. Topalli, N. S. Esmaeilzad, Ö. Zorlu, H. Kulah and O. Aydın Civi, "Reconfigurable Nested Ring-Split Ring Transmitarray Unit Cell Employing the Element Rotation Method by Microfluidics," *IEEE Trans. Antennas Propag*., vol. 63, no. 3, pp. 1163-1167, March 2015.

[72]. G. Yang, J. Li, D. Wei, S. -g. Zhou and R. Xu, "Pattern Reconfigurable Microstrip Antenna with Multidirectional Beam for Wireless Communication," *IEEE Trans. Antennas Propag*., vol. 67, no. 3, pp. 1910-1915, March 2019.

[73]. T. Aboufoul, C. Parini, X. Chen and A. Alomainy, "Pattern-Reconfigurable Planar Circular Ultra-Wideband Monopole Antenna," *IEEE Trans. Antennas Propag*., vol. 61, no. 10, pp. 4973-4980, Oct. 2013.

[74]. S. Alkaraki, J. Kelly and Z. Wang, "Reconfigurable Antenna Using Liquid Metal Vias," *2021 IEEE International Symposium on Antennas and Propagation and USNC-URSI Radio Science Meeting (APS/URSI)*, 2021, pp. 315-316.

[75]. M. Jusoh, T. Sabapathy, M. F. Jamlos and M. R. Kamarudin, "Reconfigurable Four-Parasitic-Elements Patch Antenna for High-Gain Beam Switching Application," *IEEE Antennas Wireless Propag. Lett.*, vol. 13, pp. 79-82, 2014.

[76]. X. -S. Yang, B. -Z. Wang, W. Wu and S. Xiao, “Yagi Patch Antenna with Dual-Band and Pattern Reconfigurable Characteristics,” *IEEE Antennas Wireless Propag. Lett.*, vol. 6, pp. 168-171, 2007.

[77]. A. Iftikhar et al., “Planar SIW Leaky Wave Antenna with Electronically Reconfigurable E- and H-Plane Scanning,” *IEEE Access*, vol. 7, pp. 171206-171213, 2019.

[78]. Y.-L. Lyu, X.-X. Liu, P.-Y. Wang, D. Erni, Q. Wu, C. Wang, N.-Y. Kim, and F.-Y. Meng, ‘‘Leaky-wave antennas based on noncutoff substrate integrated waveguide supporting beam scanning from backward to forward,’’ *IEEE Trans. Antennas Propag.*, vol. 64, no. 6, pp. 2155–2164, Jun. 2016.

[79]. R. Henry and M. Okoniewski, ‘‘A broadside scanning substrate integrated waveguide periodic phase-reversal leaky-wave antenna,’’ *IEEE Antennas Wireless Propag. Lett.*, vol. 15, pp. 602–605, 2015.

[80]. Z. -L. Lu, X. -X. Yang and G. -N. Tan, “A Multidirectional Pattern-Reconfigurable Patch Antenna with CSRR on the Ground,” *IEEE Antennas Wireless Propag. Lett.*, vol. 16, pp. 416-419, 2017.

[81]. J. Ouyang, Y. M. Pan and S. Y. Zheng, “Center-Fed Unilateral and Pattern Reconfigurable Planar Antennas with Slotted Ground Plane,” *IEEE Trans. Antennas Propag.*, vol. 66, no. 10, pp. 5139-5149, Oct. 2018.

[82]. H. A. Majid, M. K. A. Rahim, M. R. Hamid and M. F. Ismail, “Frequency and Pattern Reconfigurable Slot Antenna,” *IEEE Trans. Antennas Propag.*, vol. 62, no. 10, pp. 5339-5343, Oct. 2014.

[83]. Q. -Y. Guo and H. Wong, “Wideband and High-Gain Fabry–Pérot Cavity Antenna with Switched Beams for Millimeter-Wave Applications,” *IEEE Trans.*

Antennas Propag., vol. 67, no. 7, pp. 4339-4347, July 2019.

[84]. W. Lin, H. Wong and R. W. Ziolkowski, "Wideband Pattern-Reconfigurable Antenna with Switchable Broadside and Conical Beams," *IEEE Antennas Wireless Propag. Lett.*, vol. 16, pp. 2638-2641, 2017.

[85]. Y. -F. Cheng, X. Ding, B. -Z. Wang and W. Shao, "An Azimuth-Pattern-Reconfigurable Antenna With Enhanced Gain and Front-to-Back Ratio," *IEEE Antennas Wireless Propag. Lett.*, vol. 16, pp. 2303-2306, 2017.

[86]. H. Wong, Q. -Y. Guo, A. Crunteanu and L. Huitema, "A MMW Reconfigurable Antenna with Switched Beams using Functional Materials," *2019 13th European Conference on Antennas and Propagation (EuCAP)*, 2019, pp. 1-3.

[87]. Z. Chen, J. Li, T. Yuan and H. Wong, "Reconfigurable DRAs with Liquid Materials," *2020 IEEE MTT-S International Microwave Workshop Series on Advanced Materials and Processes for RF and THz Applications (IMWS-AMP)*, 2020, pp. 1-3.

[88]. Z. Chen and H. Wong, "Wideband Glass and Liquid Cylindrical Dielectric Resonator Antenna for Pattern Reconfigurable Design," *IEEE Trans. Antennas Propag.*, vol. 65, no. 5, pp. 2157-2164, May 2017.

[89]. Y. -F. Lin, W. -C. Chen, C. -H. Chen, C. -T. Liao, N. -C. Chuang and H. -M. Chen, "High-Gain MIMO Dipole Antennas with Mechanical Steerable Main Beam for 5G Small Cell," *IEEE Antennas Wireless Propag. Lett.*, vol. 18, no. 7, pp. 1317-1321, July 2019.

[90]. Z. Hu, S. Wang, Z. Shen and W. Wu, "Broadband Polarization-Reconfigurable

Water Spiral Antenna of Low Profile," *IEEE Antennas Wireless Propag. Lett.*, vol. 16, pp. 1377-1380, 2017.

[91]. T. Daeneke et al., "Liquid metals: fundamentals and applications in chemistry," *Chemical Society Reviews*, 10.1039/C7CS00043J vol. 47, no. 11, pp. 4073-4111, 2018.

[92]. P. Nayeri et al., "3D Printed Dielectric Reflectarrays: Low-Cost High-Gain Antennas at Sub-Millimeter Waves," *IEEE Trans. Antennas Propag.*, vol. 62, no. 4, pp. 2000-2008, April 2014.

[93]. J. -M. Floch, B. El Jaafari and A. El Sayed Ahmed, "New compact broadband GSM/UMTS/LTE antenna realised by 3D printing," *2015 9th European Conference on Antennas and Propagation (EuCAP)*, 2015, pp. 1-4.

[94]. Aida Garcia Lopez, E. E. Lopez C., R. Chandra and A. J. Johansson, "Optimization and fabrication by 3D printing of a volcano smoke antenna for UWB applications," *2013 7th European Conference on Antennas and Propagation (EuCAP)*, 2013, pp. 1471-1473.

[95]. F. Farzami, S. Khaledian, B. Smida and D. Erricolo, "Pattern-Reconfigurable Printed Dipole Antenna Using Loaded Parasitic Elements," *IEEE Antennas Wireless Propag. Lett.*, vol. 16, pp. 1151-1154, 2017.

[96]. I. Lim and S. Lim, "Monopole-Like and Boresight Pattern Reconfigurable Antenna," *IEEE Trans. Antennas Propag.*, vol. 61, no. 12, pp. 5854-5859, Dec. 2013.

[97]. V. T. Bharambe and J. J. Adams, "Planar 2-D Beam Steering Antenna Using

Liquid Metal Parasitics," *IEEE Trans. Antennas Propag.*, vol. 68, no. 11, pp. 7320-7327, Nov. 2020.

[98]. J. Hao, J. Ren, X. Du, J. H. Mikkelsen, M. Shen and Y. Z. Yin, "Pattern-Reconfigurable Yagi–Uda Antenna Based on Liquid Metal," *IEEE Antennas Wireless Propag. Lett.*, vol. 20, no. 4, pp. 587-591, April 2021.

[99]. C. Wang, J. C. Yeo, H. Chu, C. T. Lim and Y. -X. Guo, "Design of a Reconfigurable Patch Antenna Using the Movement of Liquid Metal," *IEEE Antennas Wireless Propag. Lett.*, vol. 17, no. 6, pp. 974-977, June 2018.

[100]. M. Li and N. Behdad, "Fluidically Tunable Frequency Selective/Phase Shifting Surfaces for High-Power Microwave Applications," *IEEE Trans. Antennas Propag.*, vol. 60, no. 6, pp. 2748-2759, June 2012.

[101]. W. M. Zhu et al., "Metamaterial tunable filter with liquid metal," *2013 IEEE 26th International Conference on Micro Electro Mechanical Systems (MEMS)*, 2013, pp. 725-728.

[102]. D. Rodrigo, L. Jofre and B. A. Cetiner, "Circular Beam-Steering Reconfigurable Antenna with Liquid Metal Parasitics," *IEEE Trans. Antennas Propag.*, vol. 60, no. 4, pp. 1796-1802, April 2012.

[103]. X. Bai, M. Su, Y. Liu and Y. Wu, "Wideband Pattern-Reconfigurable Cone Antenna Employing Liquid-Metal Reflectors," *IEEE Antennas Wireless Propag. Lett.*, vol. 17, no. 5, pp. 916-919, May 2018.

[104]. A. H. Abdelrahman, A. Z. Elsherbeni, and F. Yang, "Transmission phase limit of multilayer frequency-selective surfaces for transmitarray designs," *IEEE Trans.*

Antennas Propag., vol. 62, no. 2, pp. 690–697, Feb. 2014.

[105]. R. Milne, "Dipole array lens antenna," *IEEE Trans. Antennas Propag.*, vol. AP-30, no. 4, pp. 704–712, Jul. 1982.

[106]. J. R. Reis *et al.*, "FSS-inspired transmitarray for two-dimensional antenna beam steering," *IEEE Trans. Antennas Propag.*, vol. 64, no. 6, pp. 2197–2206, Jun. 2016.

[107]. C. G. M. Ryan, M. Reza, J. Shaker, J. R. Bray, Y. M. M. Antar, and A. Ittipiboon, "A wideband transmitarray using dual-resonant double square rings," *IEEE Trans. Antenna Propag.*, vol. 58, no. 5, pp. 1486–1493, May 2010.

[108]. P.-Y. Feng, Qu S W. "60-GHz 2D Scan Phased Transmitarray with High Gain and Low Profile[C]," *2019 13th European Conference on Antennas and Propagation (EuCAP)*, 2019: 1-4.

[109]. P. Feng and S. Qu, "A Novel Three-layer Linearly Polarized Wideband Transmitarray Antenna," *2018 IEEE International Symposium on Antennas and Propagation & USNC/URSI National Radio Science Meeting*, Boston, MA, 2018, pp. 1767-1768.

[110]. S. Datthanasombat, "Analysis and Design of High-Gain Space-Fed Passive Microstrip Array Antennas," Doctoral dissertation, Univ. of Southern California, Los Angeles, CA, USA, 2003.

[111]. S. Datthanasombat, A. Prata, Jr., L. R. Amaro, J. A. Harrell, S. Spitz, and J. Perret, "Layered lens antenna," in *Proc. IEEE Antennas Propag. Soc. Int. Symp.*, Boston, MA, USA, 2001, pp. 777–780.

[112]. D. M. Pozar, Microwave Engineering, 3rd ed. New York, NY, USA: Wiley, 2005.

[113]. A. Clemente, L. Dussopt, R. Sauleau, P. Potier, and P. Pouliguen, "1-bit reconfigurable unit cell based on pin diodes for transmit-array applications in X-band," *IEEE Trans. Antennas Propag.*, vol. 60, no. 5, pp. 2260–2269, May 2012.

[114]. B. Schoenlinner, A. Abbaspour-Tamijani, L. C. Kempel, and G. M. Rebeiz, "Switchable low-loss RF MEMS Ka-band frequency-selective surface," *IEEE Trans. Microw. Theory Tech.*, vol. 52, no. 11, pp. 2474–2481, Nov. 2004.

[115]. A. Dey, R. Guldiken, and G. Mumcu, "Microfluidically reconfigured wideband frequency-tunable liquid-metal monopole antenna," *IEEE Trans. Antennas Propag.*, vol. 64, no. 6, pp. 2572–2576, Jun. 2016.

[116]. A.-P. Saghati, J.-S. Batra, J. Kameoka, and K. Entesari, "Miniature and reconfigurable CPW folded slot antennas employing liquid-metal capacitive loading," *IEEE Trans. Antennas Propag.*, vol. 63, no. 9, pp. 3798–3807, Sep. 2015.

[117]. W. Su, R. Bahr, S. A. Nauroze, and M. M. Tentzeris, "3D printed reconfigurable helical antenna based on microfluidics and liquid metal alloy," in *Proc. IEEE Int. Symp. Antennas Propag.*, Jun./Jul. 2016, pp. 469–470.

[118]. T. Li, H. Zhai, X. Wang, L. Li and C. Liang, "Frequency-Reconfigurable Bow-Tie Antenna for Bluetooth, WiMAX, and WLAN Applications," *IEEE Antennas Wireless Propag. Lett.*, vol. 14, pp. 171-174, 2015.

[119]. Y. Hu, Y. Wang, Q. Xu, et al. "Design of monofocal and bifocal lenses by new method and their application in high‐gain lens antenna based on chiral

metamaterial[J],” *IET Microwaves, Antennas & Propagation*, 2019, 13(13): 2272-2278.

[120]. H. Yi, S. -W. Qu, K. -B. Ng, C. K. Wong and C. H. Chan, “Terahertz Wavefront Control on Both Sides of the Cascaded Metasurfaces,” *IEEE Trans. Antennas Propag.*, vol. 66, no. 1, pp. 209-216, Jan. 2018.

[121]. D. L. Diedhiou, O. de Sagazan, R. Sauleau, and A. V. Boriskin, “Contactless Microstrip Transition for Flexible Microfluidic Circuits and Antennas,” *IEEE Antennas Wireless Propag. Lett.*, vol. 14, pp. 1502-1505, 2015.

[122]. N. J. Farcich, J. Salonen, and P. M. Asbeck, “Single-Length Method Used to Determine the Dielectric Constant of Polydimethylsiloxane,” *IEEE Trans. Microw. Theory Tech.*, vol. 56, no. 12, pp. 2963-2971, 2008.

[123]. O. Sydoruk, E. Tatartschuk, E. Shamonina, and L. Solymar, “Analytical formulation for the resonant frequency of split rings,” *Journal of Applied Physics*, vol. 105, p. 014903, Jan 2009.

[124]. M. Borhani, P. Rezaei and A. Valizade, “Design of a Reconfigurable Miniaturized Microstrip Antenna for Switchable Multiband Systems,” *IEEE Antennas Wireless Propag. Lett.*, vol. 15, pp. 822-825, 2016.

[125]. A. Bhattacharjee, S. Dwari, and M. K. Mandal, “Polarization reconfigurable compact monopole antenna with wide effective bandwidth,” *IEEE Antennas Wireless Propag. Lett.*, vol. 18, no. 5, pp. 1041–1045, May 2019.

[126]. N. Nguyen-Trong, L. Hall, and C. Fumeaux, “A frequency- and patterner configurable center-shorted microstrip antenna,” *IEEE Antennas Wireless Propag.*

Lett., vol. 15, pp. 1955–1958, 2016.

[127]. H. Aissat, L. Cirio, M. Grzeskowiak, J. M. Laheurte, and O. Picon, "Reconfigurable circularly polarized antenna for short-range communication systems," *IEEE Trans. Microw. Theory Techn.*, vol. 54, no. 6, pp. 2856–2863, Jun. 2006.

[128]. J. M. Kovitz, H. Rajagopalan, and Y. Rahmat-Samii, "Design and implementation of broadband MEMS RHCP/LHCP reconfigurable arrays using rotated E-shaped patch elements," *IEEE Trans. Antennas Propag.*, vol. 63, no. 6, pp. 2497–2507, Jun. 2015.

[129]. S. -L. Chen, P. -Y. Qin, C. Ding and Y. J. Guo, "Cavity-Backed Proximity-Coupled Reconfigurable Microstrip Antenna with Agile Polarizations and Steerable Beams," *IEEE Trans. Antennas Propag.*, vol. 65, no. 10, pp. 5553-5558, Oct. 2017.

[130]. D. Schaubert, "Frequency-agile, polarization diverse microstrip antennas and frequency scanned arrays," U.S. Patent 4 367 474, Jan. 1983.

[131]. W. Lin and H. Wong, "Polarization reconfigurable wheel-shaped antenna with conical-beam radiation pattern," *IEEE Trans. Antennas Propag.*, vol. 63, no. 2, pp. 491–499, Feb. 2015.

[132]. W. Lin and H. Wong, "Wideband circular polarization reconfigurable antenna," *IEEE Trans. Antennas Propag.*, vol. 63, no. 12, pp. 5938–5944, Dec. 2015.

[133]. J.-S. Row and C.-W. Tsai, "Pattern reconfigurable antenna array with circular polarization," *IEEE Trans. Antennas Propag.*, vol. 64, no. 4, pp. 1525–1530, Apr.

2016.

[134]. Chang won Jung, Ming-jer Lee, G. P. Li and F. De Flaviis, “Reconfigurable scan-beam single-arm spiral antenna integrated with RF-MEMS switches,” *IEEE Trans. Antennas Propag.*, vol. 54, no. 2, pp. 455-463, Feb. 2006.

[135]. Balanis C A. Antenna theory: analysis and design[M]. John wiley & sons, 2015.

[136]. X. Yang, Y. Liu, H. Lei, Y. Jia, P. Zhu and Z. Zhou, “A Radiation Pattern Reconfigurable Fabry–Pérot Antenna Based on Liquid Metal,” *IEEE Trans. Antennas Propag.*, vol. 68, no. 11, pp. 7658-7663, Nov. 2020.

[137]. X. Yi, L. Huitema and H. Wong, “Polarization and Pattern Reconfigurable Cuboid Quadrifilar Helical Antenna,” *IEEE Trans. Antennas Propag.*, vol. 66, no. 6, pp. 2707-2715, June 2018.

[138]. M. R. Khan, C. Trlica, M.D. Dickey, “Recapillarity: electrochemically controlled capillary withdrawal of a liquid metal alloy from microchannels[J],” *Advanced Functional Materials*, 2015, 25(5): 671-678.

[139]. J. Hu, Y. Li and Z. Zhang, “A Novel Reconfigurable Miniaturized Phase Shifter for 2-D Beam Steering 2-Bit Array Applications,” *IEEE Microw. Wireless Compon. Lett.*, vol. 31, no. 4, pp. 381-384, April 2021.

[140]. Z. Wang, F. Zhang, H. Gao, O. Franek, G. F. Pedersen and W. Fan, “Over-the-Air Array Calibration of mmWave Phased Array in Beam-Steering Mode Based on Measured Complex Signals,” *IEEE Trans. Antennas Propag.*, vol. 69, no. 11, pp. 7876-7888, Nov. 2021.

[141]. B. Schaer, K. Rambabu, J. Bornemann and R. Vahldieck, “Design of reactive parasitic elements in electronic beam steering arrays,” *IEEE Trans. Antennas Propag.*, vol. 53, no. 6, pp. 1998-2003, June 2005.

[142]. Y. Xiong, X. Zeng and J. Li, “A Tunable Concurrent Dual-Band Phase Shifter MMIC for Beam Steering Applications,” *IEEE Transactions on Circuits and Systems II: Express Briefs*, vol. 67, no. 11, pp. 2412-2416, Nov. 2020.

[143]. P. -Y. Qin, L. -z. Song and Y. J. Guo, “Beam Steering Conformal Transmitarray Employing Ultra-Thin Triple-Layer Slot Elements,” *IEEE Trans. Antennas Propag.*, vol. 67, no. 8, pp. 5390-5398, Aug. 2019.

[144]. B. Rana, I. -G. Lee and I. -P. Hong, “Digitally Reconfigurable Transmitarray with Beam-Steering and Polarization Switching Capabilities,” *IEEE Access*, vol. 9, pp. 144140-144148, 2021.

[145]. G. -B. Wu, S. -W. Qu, S. Yang and C. H. Chan, “Low-Cost 1-D Beam-Steering Reflectarray With ±70° Scan Coverage,” *IEEE Trans. Antennas Propag.*, vol. 68, no. 6, pp. 5009-5014, June 2020.

[146]. O. Kiris, K. Topalli and M. Unlu, “A Reflectarray Antenna Using Hexagonal Lattice with Enhanced Beam Steering Capability,” *IEEE Access*, vol. 7, pp. 45526-45532, 2019.

[147]. I. -J. Nam, S. Lee and D. Kim, “Miniaturized Beam Reconfigurable Reflectarray Antenna with Wide 3-D Beam Coverage,” *IEEE Trans. Antennas Propag.*, vol. 70, no. 4, pp. 2613-2622, April 2022.

[148]. M. I. Abbasi, M. H. Dahri, M. H. Jamaluddin, N. Seman, M. R. Kamarudin

and N. H. Sulaiman, “Millimeter Wave Beam Steering Reflectarray Antenna Based on Mechanical Rotation of Array,” *IEEE Access*, vol. 7, pp. 145685-145691, 2019.

[149]. W. Cao, Y. Xiang, B. Zhang, A. Liu, T. Yu and D. Guo, “A Low-Cost Compact Patch Antenna with Beam Steering Based on CSRR-Loaded Ground,” *IEEE Antennas Wireless Propag. Lett.*, vol. 10, pp. 1520-1523, 2011.

[150]. S. -J. Ha and C. W. Jung, “Reconfigurable Beam Steering Using a Microstrip Patch Antenna With a U-Slot for Wearable Fabric Applications,” *IEEE Antennas Wireless Propag. Lett.*, vol. 10, pp. 1228-1231, 2011.

[151]. B. Babakhani and S. K. Sharma, “Dual null steering and limited beam peak steering using a triple mode microstrip patch antenna,” *2016 IEEE International Symposium on Antennas and Propagation (APSURSI)*, 2016, pp. 2141-2142.

[152]. J. Zechmeister and J. Lacik, “Complex Relative Permittivity Measurement of Selected 3D-Printed Materials up to 10 GHz,” *2019 Conference on Microwave Techniques (COMITE)*, 2019, pp. 1-4.

[153]. J. Sorocki, I. Piekarz and M. Bozzi, “Broadband Permittivity and Permeability Extraction of 3-D-Printed Magneto-Dielectric Substrates,” *IEEE Microw. Wireless Compon. Lett.*, vol. 31, no. 10, pp. 1174-1177, Oct. 2021.

[154]. H. -N. Morales-Lovera, J. -L. Olvera-Cervantes, A. Corona-Chavez and T. K. Kataria, “Dielectric Characterization of Anisotropic 3D-Printed Biodegradable Substrates Based on Polylactic Acid [Application Notes],” *IEEE Microwave Magazine*, vol. 22, no. 9, pp. 18-100, Sept. 2021.

[155]. J. Persad and S. Rocke, “Comparison of Measured and Predicted Permittivity

Values for 3D Printed PLA Substrates," *2020 IEEE MTT-S Latin America Microwave Conference (LAMC 2020)*, 2021, pp. 1-4.

[156]. G. Boussatour, P. -. Cresson, B. Genestie, N. Joly and T. Lasri, "Dielectric Characterization of Polylactic Acid Substrate in the Frequency Band 0.5–67 GHz," *IEEE Microw. Wireless Compon. Lett.*, vol. 28, no. 5, pp. 374-376, May 2018.

[157]. J. M. Felício, C. A. Fernandes and J. R. Costa, "Complex permittivity and anisotropy measurement of 3D-printed PLA at microwaves and millimeter-waves," *2016 22nd International Conference on Applied Electromagnetics and Communications (ICECOM)*, 2016, pp. 1-6.

[158]. Z. Qu, S. -W. Qu, Z. Zhang, S. Yang and C. H. Chan, "Wide-Angle Scanning Lens Fed by Small-Scale Antenna Array for 5G in Millimeter-Wave Band," *IEEE Trans. Antennas Propag.*, vol. 68, no. 5, pp. 3635-3643, May 2020.

[159]. W. Chen, Y. Li, R. Li, A. V. -Y. Thean and Y. -X. Guo, "Bendable and Stretchable Microfluidic Liquid Metal-Based Filter," *IEEE Microw. Wireless Compon. Lett.*, vol. 28, no. 3, pp. 203-205, March 2018.

[160]. C. Koo, B. E. LeBlanc, M. Kelley, H. E. Fitzgerald, G. H. Huff and A. Han, "Manipulating Liquid Metal Droplets in Microfluidic Channels with Minimized Skin Residues Toward Tunable RF Applications," *Journal Microelectr. Sys.*, vol. 24, no. 4, pp. 1069-1076, Aug. 2015.

[161]. M. A. Rafi, B. D. Wiltshire and M. H. Zarifi, "Wideband Tunable Modified Split Ring Resonator Structure Using Liquid Metal and 3-D Printing," *IEEE Microw. Wireless Compon. Lett.*, vol. 30, no. 5, pp. 469-472, May 2020.

[162]. A. Ha and K. Kim, “Frequency tunable liquid metal planar inverted-F antenna,” *IET Elect. Lett.*, vol. 52, no. 2, pp. 100-102, Jan. 2016.

[163]. A. M. Watson *et al*., “Physically Reconfigurable RF Liquid Electronics via Laplace Barriers,” *IEEE Trans. Microw. Theory Techn.*, vol. 67, no. 12, pp. 4881-4889, Dec. 2019.

[164]. L. Song, W. Gao, C. O. Chui and Y. Rahmat-Samii, “Wideband Frequency Reconfigurable Patch Antenna with Switchable Slots Based on Liquid Metal and 3-D Printed Microfluidics,” *IEEE Trans. Antennas Propag.*, vol. 67, no. 5, pp. 2886-2895, May 2019.

[165]. T. Kim, K. Kim, S. Kim, J. Lee and W. Kim, “Micropatterning of Liquid Metal by Dewetting,” *Journal Microelectr. Sys.*, vol. 26, no. 6, pp. 1244-1247, Dec. 2017.

[166]. J. Low, P. Chee and E. Lim, “Deformable Liquid Metal Patch Antenna for Air Pressure Detection,” *IEEE Sensors Journal*, vol. 20, no. 8, pp. 3963-3970, Apr. 2020.

[167]. V. T. Bharambe, J. Ma, M. D. Dickey and J. J. Adams, “Planar, Multifunctional 3D Printed Antennas Using Liquid Metal Parasitics,” *IEEE Access*, vol. 7, pp. 134245-134255, Sept. 2019.

[168]. M. Wang, M. R. Khan, C. Trlica, M. D. Dickey, and J. J. Adams, “Pump free feedback control of a frequency reconfigurable liquid metal monopole,” *Proc. IEEE Int. Symp. Antennas Propag.*, 2015, pp. 2223– 2224.

[169]. A. Qaroot and G. Mumcu, “Microfluidically Reconfigurable Reflection Phase Shifter,” *IEEE Microw. Wireless Compon. Lett.*, vol. 28, no. 8, pp. 684-686, Aug.

2018.

[170]. M. N. Sarah, S. Shahrokh, S. H. Hjalti, “Band-Reconfigurable Filter with Liquid Metal Actuation,” *IEEE Trans. Microw. Theory Techn.*, vol. 66, no. 6., pp. 3073-3080. Jun. 2018.

[171]. A. Dey and G. Mumcu, “Microfluidically Controlled Frequency Tunable Monopole Antenna for High-Power Applications,” IEEE Antennas Wireless Propag. Lett., vol. 15, pp. 226-229, 2016.

[172]. S. Singh et al., “A Pattern and Polarization Reconfigurable Liquid Metal Helical Antenna,” *IEEE Int. Symp. Antennas and Propag*. & USNC/URSI National Radio Science Meeting, Boston, MA, 2018, pp. 857-858.

[173]. M. Wang, C. Trlica, M. R. Khan, M. D. Dickey, and J. J. Adams, “A reconfigurable liquid metal antenna driven by electrochemically controlled capillarity,” J. Appl. Phys., vol. 117, no. 19, May 2015.